UNIVERSITAT POLITÈCNICA DE VALÈNCIA
DEPARTAMENTO DE QUÍMICA
INSTITUTO UNIVERSITARIO MIXTO DE TECNOLOGÍA QUÍMICA
(UPV-CSIC)

DOCTORAL THESIS

Photoreactivity of DNA etheno adducts: a spectroscopic and mechanistic study

---

Paloma Lizondo Aranda

Supervisors:

Prof. Miguel Ángel Miranda Alonso
Dra. Virginie Lhiaubet-Vallet

Valencia, September 2022

CERTIFICATION

Miguel Ángel Miranda Alonso, full Professor of the Universitat Politècnica de València (UPV) and Virginie Lhiaubet-Vallet, tenured scientist of the Consejo Superior de Investigaciones Científicas (CSIC),

CERTIFY that the Doctoral Thesis entitled "Photoreactivity of DNA etheno adducts: spectroscopic and mechanistic study" has been developed by Paloma Lizondo Aranda under their supervision at the Instituto Universitario Mixto de Tecnología Química (UPV-CSIC).

Prof. Miguel Ángel Miranda Alonso Dra. Virginie Lhiaubet-Vallet

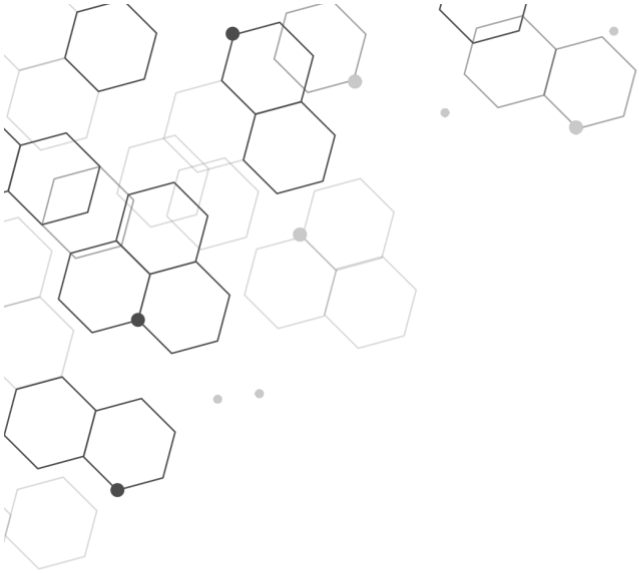

ABBREVIATIONS AND SYMBOLS

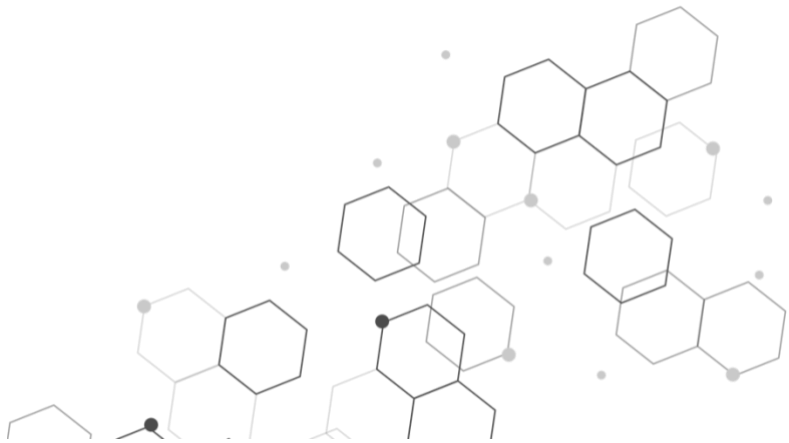

ABBREVIATIONS AND SYMBOLS

$^{\bullet}OH$	Hydroxyl radical
$^{1}O_2$	Singlet oxygen
^{13}C NMR	Carbon-13 nuclear magnetic resonance
^{1}H NMR	Proton nuclear magnetic resonance
3-meA	N3-methyladenine
$^{3}RB^{2-*}$	Triplet excited state of Rose Bengal
3-meA	N3-methyladenine
4-NHE	Trans-4-hydroxy-2-nonenal
6-4PPs	6-4 photoproducts
7-meG	N7-methylguanine
8-oxoA	8-oxo-7,8-dihydroadenine
8-oxodG	8-oxo-deoxyguanosine
8-oxoG	8-oxo-7,8-dihydroguanine
8-HDF	8-hydroxy-5-deazaflavin
A	Acceptor
AcEtO	Ethyl acetate
ACN	Acetonitrile
AP	Apurinic sites
APTES	(3-aminopropyl)triethoxysilane
Au	Gold
BER	Base excision repair
BP	Benzophenone
CASSCF	Complete active space self-consistent field
CASPT2	Complete active second-order perturbation theory

CBP	4-carboxybenzophenone
$CBP^{\bullet-}$	4-carboxybenzophenone radical anion
$CBPH^{\bullet}$	4-carboxybenzophenone ketyl radical
CH_2Cl_2	Dichloromethane
CI	Conical intersection
CPDs	Cyclobutane pyrimidine dimers
D	Donor
D_2O	Deuterated water
DABCO	1,4-diazabicyclo[2.2.2]octane
DewarPPs	Dewar valence isomers
DFT	Density functional theory
dG	2'-deoxyguanosine
DLS	Dynamic light scattering
DMF	N,N-dimethylformamide
DMSO-d6	Deuterated dimethyl sulfoxide
DNA	Deoxyribonucleic Acid
DSB	Double strand break
ε	Molar absorption coefficient
ε-adducts	Etheno adducts
εdA	1,N6-etheno-2'-deoxyadenosine
εdC	3,N4-etheno-2'-deoxycytidine
εdCH^{+}	Protonated form of εdC
EDC	N-(3-dimethylaminopropyl)-N-ethylcarbodiimide hydrochloride
εdG	1,N2-etheno-2'-deoxyguanosine

E_S	Singlet excited state energy
E_T	Triplet excited state energy
EF_Δ	Enhancement factor
ET	Energy transfer
Et_2O	Diethylether
ϕf	Fluorescence quantum yield
ϕ_{ISC}	ISC quantum yield
F	Fluorescence
FAD	Flavin adenine dinucleotide
FapyA	4,6-diamino-5-formamidopyrimidine
FapyG	2,6-diamino-4-hydroxy-5-formamidopyrimidine
FC	Frank-condon
ForU	5-formyluracil
FRET	Förster resonance energy transfer
$G^{\bullet+}$	Guanine radical cation
GGR	Global genomic repair
Gh	Guanidinohydantoin
H_2O	Water
H_2O_2	Hydrogen peroxide
HmU	5-Hydroxymethyluracil
HOMO	Highest occupied molecular orbital
HRMS-(ESI)	High resolution electrospray ionization mass spectrometry
$h\nu$	Light
IARC	International agency for research on cancer
IC	Internal conversion

ICP-OES	Inductively coupled plasma-optical emission spectroscopy
IR	Ionizing radiation
IRF	Instrument response function
ISC	Intersystem crossing
K_2CO_3	Potassium carbonate
k_d	Intrinsic decay rate constant
k_q	Quenching rate constant
λ_f	Fluorescence emission maximum
LFP	Laser flash photolysis
λ_{max}	Absorption maximum
λ_p	Phosphorescence emission maximum
LPO	Lipid peroxidation
LSPR	Localized surface plasmon resonance
LUMO	Lowest unoccupied molecular orbital
MeOH	Methanol
MGMT	O^6-methylguanine-DNA methyltransferase
MMR	DNA mismatch repair
MTHF	5,10-methenyltetrahydrofolate
N2,3-εdG	N2,3-etheno-2'-deoxyguanosine
Nd-YAG	Neodymium-doped yttrium aluminium garnet
NER	Nucleotide excision repair
NH_4OH	Ammonium hydroxide solution
NHEJ	Non-homologous DNA end joining
nm	Nanometer
NPs	Nanoparticles

NTO	Natural transition orbitals
O_2	Oxygen
$O_2^{\bullet-}$	Superoxide Anion
O6-meG	O6-methylguanine
Ox	2,2-diamino-oxazolone
P	Phosphorescence
PBS	Phosphate-buffered saline
PDI	Photodynamic inactivation
PDT	Photodynamic therapy
PES	Potential energy surface
PET	Photoinduced electron transfer
Phs	Photosensitizer
ps	picosecond
Pyo	5-methyl-2-pyrimidone
QDs	Quantum Dots
$RB^{\bullet-}$	Rose Bengal radical cataion
$RB^{\bullet 3-}$	Rose Bengal radical anaion
RB^{2-}	Rose Bengal
ROS	Reactive oxygen species
S_0	Ground state
SB	Strand break
SEF	Surface enhanced fluorescence
SERS	Surface enhanced raman scattering
S_n	Singlet excited state
Sp	Spiroiminodihydantoin
SSB	Single strand break

SSET	Singlet-singlet energy transfer
TBDMSCl	Tert-butyldimethylsilyl chloride
TCR	Transcription-coupled repair
TD-DFT	Time-dependent density functional theory
TEM	Transmission electron microscopy
TEOS	Tetraethyl orthosilicate
TFA	Trifluoroacetic acid
$<\tau>$	Average lifetime
τ_f	Fluorescence lifetime
T_n	Triplet excited state
t_R	Retention time
τ_T	Triplet lifetime
TTET	Triplet-triplet energy transfer
UDG	Uracil DNA glycosylase
UV	Ultraviolet (UVA, UVB and UVC)
Vis	Visible
VR	Vibrational relaxation
ζp	Zeta potential
αKG	2-oxoglutarate

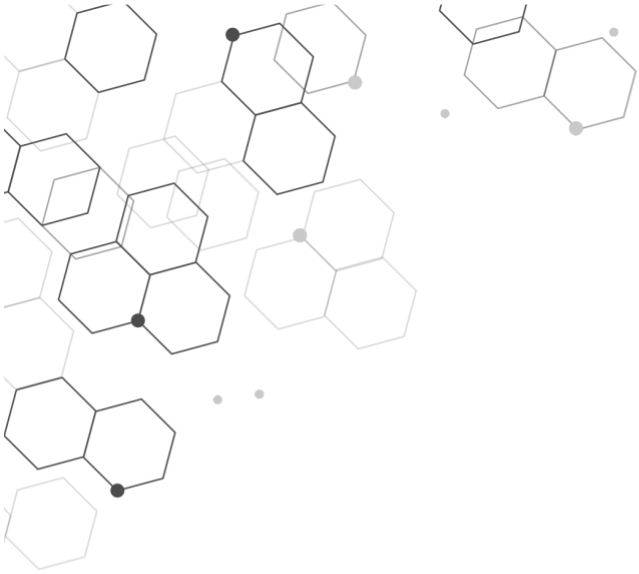

OUTLINE

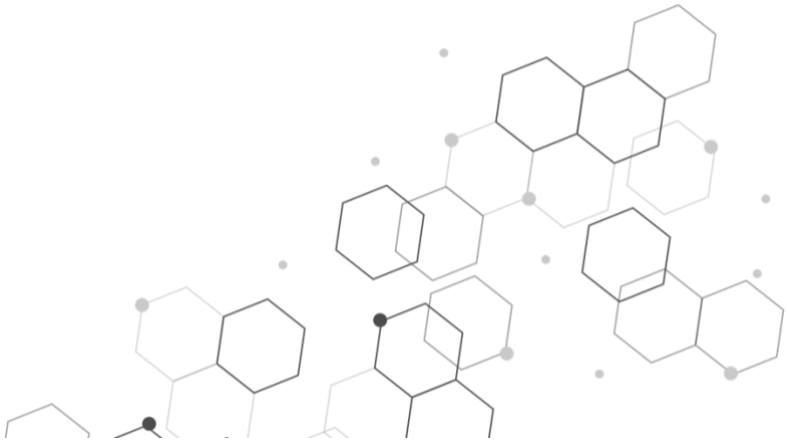

CHAPTER 1

INTRODUCTION

1.1. THE POWER OF SUN INVOLVED IN CHEMISTRY

Since the beginning of time, the Sun has been associated with energy, life and heat. It has been deified by many ancient cultures but also exploited by civilizations like Mayans as a time reference to build their calendar.

Undoubtedly, over the history the Sun has been the main player in many aspects of our lives. For chemists, the end of the 19th century marks a new era when a chemist called Giacomo Luigi Ciamician in the balcony of his institute began to glimpse the chemistry hidden behind the solar light absorption of matter. Together with is mate Paul Silber, he systematically studied the behavior of organic substances towards light. This way, they discovered photoreactions such as the conversion of quinone to hydroquinone, the [2+2] photocycloaddition through the formation of carvone camphor from carvone, etc. During his career, Giacomo dedicated all his efforts to develop a new area of chemistry called Photochemistry.

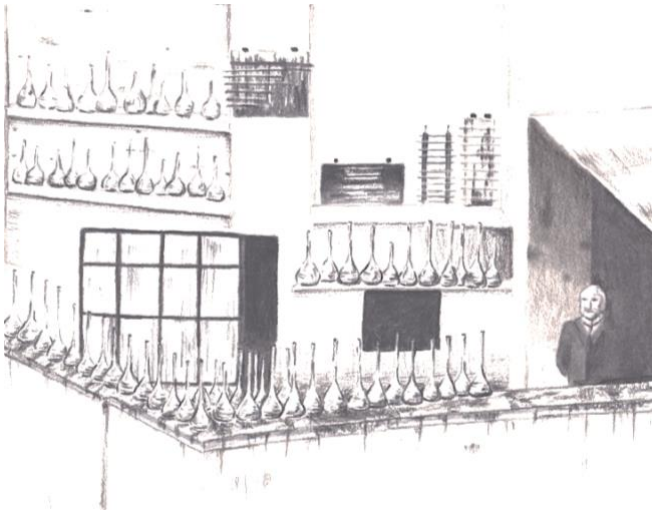

Figure 1. 1. Painting of Giacomo Ciamician and his flasks collection exposed to the sun on the balcony of his institute.

From then on, this field began to grow unveiling the importance of the Sun in our daily life. For instance, its involvement

in some physiological mechanisms of living species like the formation of vitamin D for humans, or the photosynthesis in plants.

It is well-known that the Sun is capable of emitting electromagnetic radiation extending from radio to gamma-rays, this is what is called solar spectrum. Among the different regions, the ultraviolet (UV) part has been recognized to be particularly harmful for living organisms. It is divided into 3 portions: UVC (up to 290 nm), UVB (290 – 320 nm) and UVA (320 -400 nm). But Earth has its own protection shield, the ozone layer, which absorbs the most energetic UV radiation from *ca.* 200 nm to 310 nm. Thus, UVC and part of UVB are filtered, whereas UVA penetrates and represents more than 95% of the UV radiation that reaches the Earth surface. These wavelengths, together with the visible (Vis) region (400-700 nm) are biologically active. They can be absorbed by some biomolecules or endogenous compounds and cause beneficial but also harmful effects such as mutations that can evolve into skin cancer.

Any part of a molecule able to absorb light is called chromophore. This is for example the case for organic molecules containing groups such as double bonds, carbonyl groups, aromatic rings, enones, etc. These compounds in the presence of light can undergo physical and chemical changes, which are studied in the fields of photophysics and photochemistry.

1.1.1. Mechanisms behind the photophysics and photochemistry of molecules

The light, formed by elemental particles called photons, has a dual wave-particle nature. Photochemical or photophysical processes can only take place when one photon (with an energy $h\nu$) is absorbed by a chromophore. This is the First Law of photochemistry attributed to Grotthuss and Drapper. [1]

1.1.1.1. Photophysical processes

As a general definition, photophysics describes photoexcitation and any subsequent process that does not involve any chemical change.

Everything starts with the absorption of a photon by a chromophore that gives rise to an electronic transition; one electron promotes from an occupied orbital to an unoccupied orbital of the same molecule.

The knowledge of the electronic transitions taking place in a molecule allows predicting its photoreactivity or its radiative or nonradiative deactivation mechanisms. Orbitals can be of different types: σ orbitals, π orbitals generally found in unsaturated systems, or the nonbonding n orbitals present for example in heteroatoms such as oxygen or nitrogen.[2] An asterisk is added to refer to antibonding orbitals (σ* or π*). The way to express a transition from an orbital to another one consists in citing the initial and final orbitals, for example transition of a non-bonding electron (n) to an antibonding orbital (π*) will be labeled as nπ* (Figure 1.2).

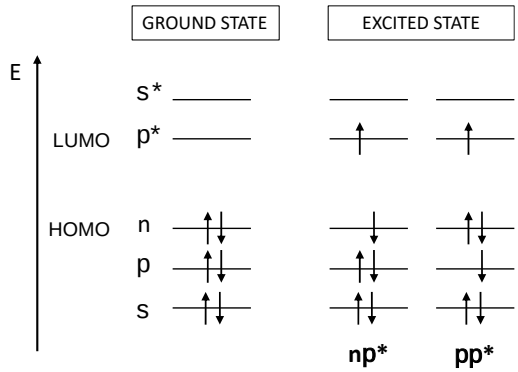

Figure 1. 2. Electronic transitions depending of carbonyl groups.

The electronic transition with the lowest energy corresponds to promotion of an electron from the Highest Occupied Molecular Orbital (HOMO) to the Lowest Unoccupied Molecular Orbital

(LUMO). Transitions between other occupied and unoccupied orbitals can also take place depending on the absorbed energy.

The photophysical processes occurring after light absorption are summarized in the Jablonski diagram (Figure 1. 3). After excitation, the molecule has reached a singlet excited state (S_n), which is a really unstable species that aims to deactivate by radiative or non-radiative processes to return to the ground state (S_0). Any of the vibrational levels of S_n can be populated, thus, the first process to occur is vibrational relaxation (VR) to reach the zero vibrational level, followed by internal conversion (IC) until reaching the lowest singlet excited state, S_1. All these deactivation ways are radiationless and are represented by curved arrows. At this stage, different pathways are open: the molecule can reach its ground state through IC, though a radiative process called fluorescence (F) or intersystem crossing (ISC) can occur populating a triplet excited state T_n. In this latter, by contrast with singlet manifold, the two spins are parallel, and the multiplicity, 2S+1, is 3. Once populated through ISC, T_n suffers the same deactivation path as S_n, ie. VR, IC, but after reaching the lowest triplet manifold T_1 deactivation to S_0 takes place through nonradiative ISC or phosphorescence emission (P).

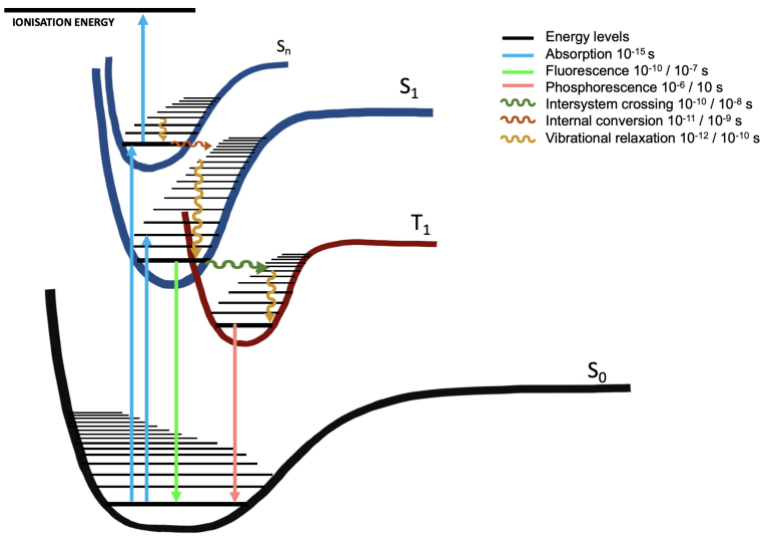

Figure 1. 3. Jablonski diagram.

Under particular conditions, excited states are capable to absorb a second photon promoting the electron to further upper excited states or even reach the ionization level.

Photochemical and photophysical processes are continuously competing. For this reason, it is crucial to known the photophysical properties of the molecules/chromophores absorbing the radiation, in order to envisage what type of photophysical or photochemical processes they can produce.

1.1.1.2. Photochemical processes

Photochemistry is defined in the gold book of IUPAC [3] as the branch of chemistry concerned with the chemical effects of light. It entails all the transformations that a molecule undergoes under irradiation related with its structure or electronic configuration, which differs from their initial ground state. [4]

Photochemistry plays an important role in natural and chemical processes since this discipline can access types of reactions that classical (thermal) chemistry cannot. Indeed, there are many "ground-state" reactions that have photochemical counterparts, one can cite for example photocycloadditions, photo-Fries rearrangement, photoisomerizations, etc. It is noteworthy that the photochemical routes offer the advantage over thermal methods of forming thermodynamically disfavored products, overcoming large activation barriers, and allowing reactivity otherwise forbidden in thermal reactions.

Light can be directly absorbed by the molecule of interest, triggering the purported reactivity, or it can be absorbed by another compound, called photosensitizer (Phs), which in turn will mediate the desired alteration. Photosensitized reactions are generally classified into different types of processes including energy transfer, Type I or Type II oxidations.

1.1.1.2.1. Energy Transfer

During energy transfer processes, the excited molecule, designated as the donor D* (Figure 1. 4), transfers its excess of energy to another molecule called acceptor (A) (Figure 1. 4) leading to the excited state of the acceptor (A*). This process permits an indirect excitation of A using an excitation wavelength that A does not absorb but D does. Singlet-singlet (SSET) or triplet-triplet energy transfer (TTET) can take place depending on the multiplicity of the donor excited state.

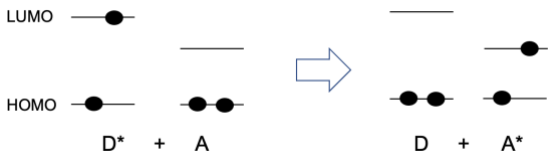

Figure 1. 4. Overall ET mechanism.

Energy transfer (ET) proceeds downhill, ie. the energy of D excited state is higher than that of A. Moreover, ET must compete with intrinsic deactivation of D*; thus, to be efficient the ET rate constant must be higher than that of D* intrinsic relaxation.

Two different types of ET mechanism exist. The Föster resonance energy transfer (FRET) occurs through a dipole-dipole coupling for which the orbital orientation between donor and acceptor has to be optimal. Interestingly, this mechanism is effective at distances of up to 100 Å.

For the electron exchange mechanism, also known as Dexter mechanism, the molecular orbitals of donor and acceptor have to overlap. For this reason, it occurs at short-range, typically within 10 Å. While SSET can take place through both types of processes, Dexter mechanism is the dominant one for TTET.

1.1.1.2.2. Photosensitized redox reaction

1.1.1.2.2.1. Type I reactions

Type I reactions are photoredox reactions that involve the generation of radicals or radical ions as reactive intermediates of electron transfer or H-abstraction mechanism. This is usually the initiation step in radical chain reactions that ultimately lead to oxygenated products.

The electron transfer, or photoinduced electron transfer (PET), is a charge-transfer type mechanism that involves two different molecules a donor (D) and an acceptor (A). This mechanism is governed by the reduction potential (E_{red}) of the photosensitizer in its excited state and that of the substrate in its ground state. The excited photosensitizer can play the role of the oxidant or reductant, ie. it can abstract or inject an electron to the substrate (Figure 1. 5). This leads to the formation of two ground-state species, the radical anion of the acceptor ($A^{\bullet-}$) and radical cation of the donor ($D^{\bullet+}$). [5]

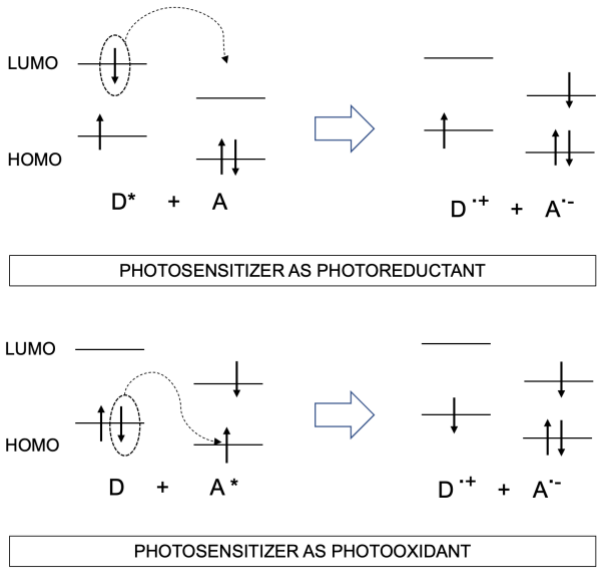

Figure 1. 5. Schematic representation of PET mechanism.

Finally, another Type I reaction is hydrogen atom abstraction. This process is generally, but not only, observed for compounds exhibiting $S_1(n\pi^*)$ or $T_1(n\pi^*)$ excited states, as it is common for ketone derivatives. The excited ketone moiety abstracts a hydrogen from a donor like alcohols, forming ketyl radicals (Figure 1. 6). Then, these radicals abstract a second hydrogen from their environment or recombine to form alcohols or diols, respectively.

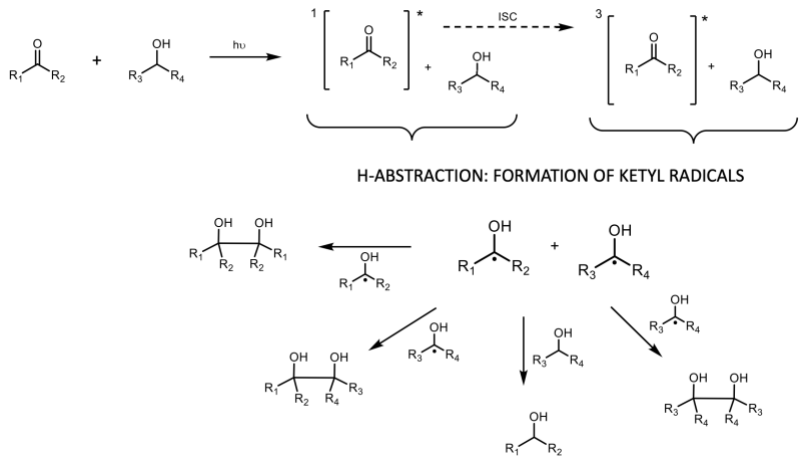

Figure 1. 6. H-abstraction mechanism and its possible products.

1.1.1.2.2.2. Type II reactions

Type II reactions involve the generation of singlet oxygen ($^1O_2$), this species is part of the reactive oxygen species (ROS) together with hydroxyl radical ($^{\bullet}OH$), hydrogen peroxide (H_2O_2) and superoxide anion ($O_2^{\bullet-}$).

The ground state of diatomic oxygen (O_2) is a triplet state ($^3\Sigma_g$, O_2) with two electrons of parallel spin in separated π^* orbitals. Singlet oxygen is an excited state of oxygen, which is formed through energy transfer from a photosensitizer, normally in its triplet excited state, to oxygen (O_2). Each photosensitizer molecule can typically produce 10^3–10^5 molecules of $^1O_2$ before being degraded through photobleaching by $^1O_2$ or by some other processes. [6]

Two $^1O_2$ states exist, $^1\Delta_g$ and $^3\Sigma_g$, but if not specified otherwise $^1O_2$ generally refers to $^1\Delta_g$ state, which has a lifetime of around 10^{-6} – 10^{-3}s in solution [7] and emits phosphorescence at 1270 nm. It may interact with other molecules through physical quenching, ie. after deactivation, neither consumption of oxygen nor product formation is observed; conversely, chemical quenching usually results in O_2 consumption and photoproduct formation.

Type II reactions are widely used in the photobiology fields for therapeutic purposes such as photodynamic therapy (PDT) or photodynamic inactivation (PDI) of bacteria.

1.2. BIOLOGICAL DAMAGES IN HUMANS

1.2.1. Dark lesions in DNA

Deoxyribonucleic acid (DNA) encodes genetic information which is crucial for the preservation of life. However, DNA is exposed to many endogenous and exogenous chemical agents that can violate its integrity. It is noteworthy that the DNA in a single cell can experience, at least, one million structural changes per day.[8] Fortunately, DNA has its own repair mechanisms to prevent aging and fatal errors. Nonetheless, the activation of this process holds the cell cycle and thus delays its division. This is what is known as aging process. However, the presence of DNA damages in cell increases the genotoxic stress, resulting in a higher accumulation of oxidative DNA damages together with high formation rates of ROS compared to that occurring during aging. [9] This excess of lesion could endanger the cell viability as it can accumulate in the same organs triggering in an accelerated aging, [10] generating a high risk spot with damaged cell that can end in cancer appearance.

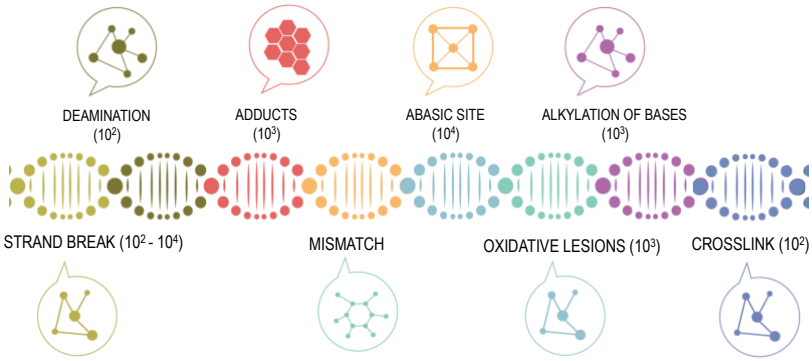

Figure 1. 7. Types of DNA lesions. In brackets, frequency rate per cell per day.

It is noteworthy that numerous errors (Figure 1.7) come from normal cellular processes such as depurination and depyrimidination. In these processes, the β-*N*-glycosidic bond between the deoxyribose and the purine or pyrimidine base is hydrolyzed generating a site lacking a base, known as an abasic site. Depyrimidination, with a frequency of *ca.* 10^2 damages per cell per day, has a very slow rate compared with that of depurination of *ca.* 10^4. [11] This damage not only can be generated spontaneously but also as an intermediate during the base excision repair process; therefore, any error occurring during the repair process would lead to an abasic site, which could provide a route to mutation upon replication.

Another spontaneous modification during DNA replication is the addition of an erroneous base in the new DNA strand that gives rise to a mismatched base pairing. Two types of base pair mismatch exist depending on the type of change produced. Transition refers to a mutation in which one base is replaced by another of the same class (purine by purine and pyrimidine by pyrimidine) and transversion involves a mutation in which a purine is replaced with a pyrimidine or vice versa.[12]

The integrity of the nucleotide structure can also be compromised in the case of adenine, cytosine and guanosine that

contain exocyclic amines, which can undergo deamination. Removal of the amino group leads firstly to the formation of ammonia, which ends up as urea after an enzyme-assisted addition of carbon dioxide. This process occurs frequently in the liver or kidney and, has a high frequency rate of 10^2 per cell per day. [11]

The vast majority of DNA lesions disturbs the DNA helix structure by modifying the bases. However, some processes can also lead to strand break formation. In this case, the phosphodiester backbone is broken on one strand, ie. single strand break (SSB), or on both strands, ie. double strand break (DSB). This type of lesion comes both from exogenous agents like ionizing radiation (IR), and endogenous processes like oxidative stress and reactive oxygen species (ROS) generation or from errors produced during the replication process.[13]

It has been established that above all the DNA damages present within the cell, strand break (SB) is one of the most dangerous one with a rate frequency of 10^2-10^4 per cell per day.[11] Sometimes, these SBs are the consequence of the action of drugs that cause crosslinks within the DNA creating a covalent link between two bases. This interaction can occur between nucleotides of the same strand (intrastrand crosslink) or between nucleotides of opposite strands (interstrand crosslink). Crosslinks appear approximately 10^3 times per cell per day [11], and have important cytotoxic effects as they can block the processes of transcription or replication.[14] UV radiation is one of the most common exogenous agents producing crosslinks. It is especially responsible for crosslinks formation between two pyrimidine bases that are located consecutively within the same strand. These lesions are commonly known as a cyclobutane pyrimidine dimers (CPDs) or 6–4 photoproducts (6-4PPs). [15] Other exogenous agents are chemotherapeutic compounds for treating cancer like nitrogen mustards or cisplatin. These drugs are classified as bifunctional alkylating agents as they are able to covalently bind to the two DNA strands, resulting in an interstrand crosslink formation.[16] Their bifunctional reactivity differentiates them from other drugs causing one site alkylating damages.

Alkylation of DNA occurs with a frequency up to 10^3 per cell per day.[11] Nucleotides have several reaction sites (Figure 1. 8) that

can be attacked by endogenous or exogenous agents. In this context, recurrent damages result from guanine methylation at N7 or O6 giving rise to N7-methylguanine (7-meG) and O6-methylguanine (O6-meG), respectively, or from adenine leading to N3-methyladenine (3-meA). Some of these damages are cytotoxic and can block replication, interrupt transcription or activate apoptosis, but they can also be mutagenic by inducing miscoding and causing mutations in newly synthesized DNA.[17] However, not all the alkylating processes end up in mutation, they can also be cytotoxic or innocuous to the cell. Interestingly, alkylation is used by the cell in some mechanisms. This is the case for formation of the epigenetic base 5-methylcytosine, which regulates gene transcription. [18,19] Therefore, this process has not just a negative connotation for our health as it can also be beneficial.

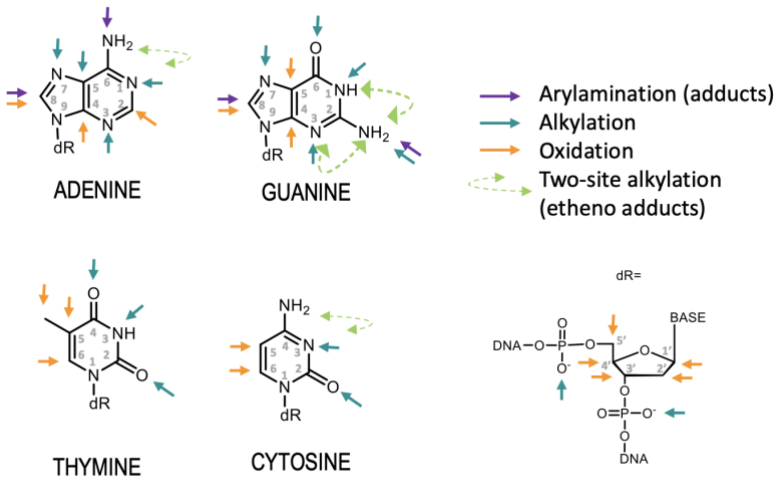

Figure 1. 8. Nucleotide reactive sites predisposed to alkylation.

Orange arrows in Figure 1. 8 show vulnerable sites for base oxidation. This type of damage comes as a result of a metabolic process or is due to exposure to environmental toxins, which produces reactive oxygen species (ROS), being this latter the main pathway for nucleobase oxidation. For example, singlet oxygen can oxidize guanine yielding to 8-oxo-7,8-dihydroguanine (8-oxoG),

which is the most common oxidatively formed lesion. Figure 1. 9 encloses other important oxidative lesions such as 2,6-diamino-4-hydroxy-5-formamidopyrimidine (FapyG), spiroiminodihydantoin (Sp), thymine glycol, 5-hydroxycytosine and 5-hydroxyuracil.

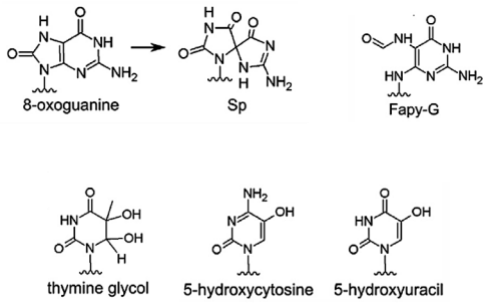

Figure 1. 9. Most common DNA oxidative lesions.

Other types of damage are the DNA adducts obtained from reaction with oxidative agents or other reactive molecules. These adducts are the result of a covalent link between the nucleobase and some endogenous molecules, for example subproducts arising from lipid peroxidation. But, they can also arise from reaction with exogenous species like benzo(a)pyrene found in cigarette smoke. The modification takes place at the nucleophilic sites of bases (see Figure 1. 8), as well as at C8 of purines and also at the endocyclic or exocyclic nitrogen and oxygen atoms of nucleotides.[20]

The type of DNA adducts varies depending not only on the structure of the reactive species or the nature of the electrophile, but also on the interaction of the reactive agent with DNA. In this context, intercalation can provide a particular orientation between the electrophile and the nucleobases, favoring the reaction at concrete nucleophilic sites. Therefore, molecules that exhibit a high sequence specificity result in a high yield of a determined adduct formation. The adducts can correspond to the covalent union of the electrophile and the base, namely bulky adducts, or in a simple addition of a group like in the case of methylation.[21]

This thesis is centered on one of the most common family of DNA adduct, the etheno adducts.

1.2.1.1. Etheno adducts

Among exocyclic DNA adducts, etheno adduct (ε-adduct) family has attracted a lot of attention because of its mutagenic properties.[22] Their origin was firstly attributed to the reactivity of metabolically formed aldehydes from human carcinogens such as vinyl chloride. [23] However, their presence as background DNA lesions in rodent or human tissues [24,25] suggests that these adducts are also the result of an endogenous reaction. On this basis, the role of lipid peroxidation (LPO) active products has also been demonstrated. This biochemical process is constantly occurring in our body, and it is related with inflammation oxidative stress mechanism. The ROS generated during this process can degrade the membrane polyunsaturated fatty acids by LPO causing reactive aldehydes species ie. malondialdehyde or trans-4-hydroxy-2-nonenal (4-NHE). These can directly, or after metabolization to 4-hydroperoxy-2-nonal, react with the nucleobase yielding an extra imidazole ring. This etheno bridge is formed between the exocyclic amine of cytosine, guanine or adenine and the amine at N3 or N1 of the base skeleton. [26,27]

There are four possible ε-adducts: 1,N6-etheno-2'-deoxyadenosine (εdA), 3,N4-etheno-2'-deoxycytidine (εdC), N2,3-etheno-2'-deoxyguanosine (N2,3-εdG) and 1,N2-etheno-2'-deoxyguanosine (εdG) (Figure 1. 10).

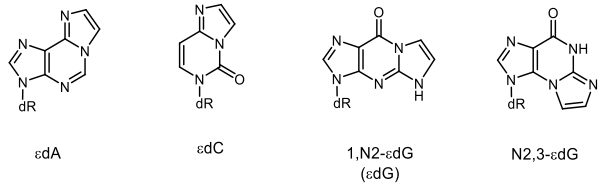

Figure 1. 10. Etheno DNA adducts structures.

The four etheno adducts have been reported in both rodents and humans, especially in chronically inflamed human tissues, making their quantification useful as potential biomarkers for cancer of colon, prostate, lung, etc. [28–31] The high carcinogenic

potential of etheno adducts has been underlined. In particular for εdA, that incorporated into plasmid DNA, was found to be more mutagenic than the 8-oxo-deoxyguanosine (8-oxodG) lesion in HeLa cells. [32] Several studies also revealed ε-adducts mutagenetic potential in mammals cells. [33,34] εdA may cause AT-TA and AT-CG transversions and AT-GC transition, whereas εdC leads to CG-AT transversions and CG-TA transition, and the etheno adducts derived from guanine (N2,3-εdG and εdG) can induce GC-AT transition. [27,28,35] These modifications have been associated with the interference of the etheno ring in the formation of Watson−Crick hydrogen bonding. [36–38] It is noteworthy that their mutagenicity has been established by *in vitro* experiments. For example, 4-HNE was shown to induce to a high frequency of G to T transversions at the third base of codon 249 (-AGG*-) in the p53 gene, which represents a mutational hotspot in human cancers.[22]

1.2.2. DNA lesions induced by light

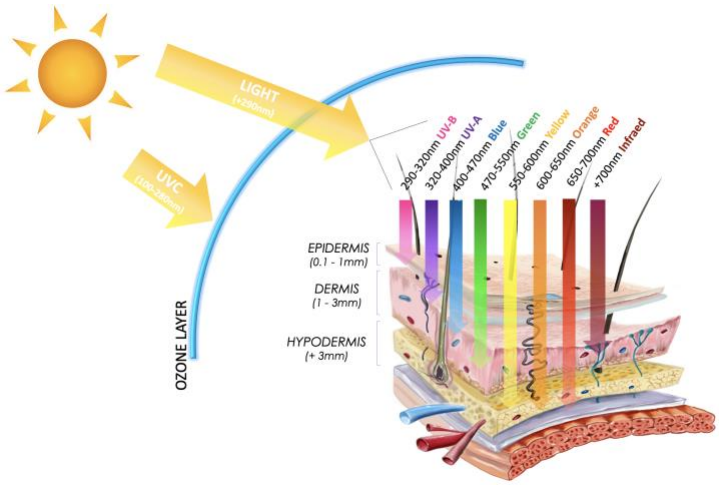

Figure 1. 11. Representation of different regions of the solar spectrum and their ability to penetrate the skin.

The World Health Organization (WHO) considered ultraviolet light like a carcinogenic and mutagenic component of sun. [39] This is due not only to the direct absorption of UVB by the nucleic acids

but also to UVA absorption by endogenous or exogenous compounds that can act indirectly by photosensitizing DNA damages. Both direct or indirect processes can modify the nucleic acid structure and give rise to mutations that can ultimately derive in cancer appearance. [40]

Therefore, it is of great interest to identify the different mutagenic DNA photoproducts and establish the molecular processes responsible for their formation in order to develop new strategies to prevent cancer. In this scenario, two types of DNA damages must be distinguished: direct and photosensitized damages (Figure 1. 12).

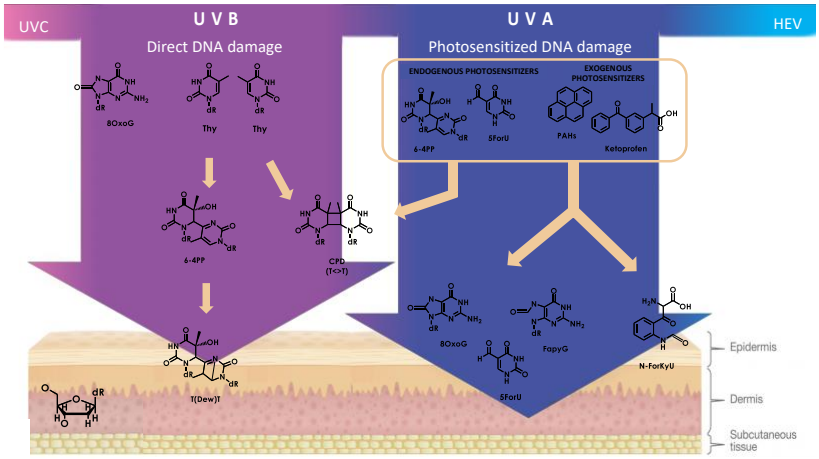

Figure 1. 12. DNA lesions classified as a result of direct UVB absorption (left) and/or photosensitization (right).

1.2.2.1. Direct DNA light absorption

DNA nucleotides have an absorption band with a maximum in the UVC at *ca.* 260-270 nm that reaches the UVB region. In DNA oligomers, a weak absorption tail has been reported in the UVA. Therefore, and since the UVC radiation does not reach the Earth surface, this section reports the DNA damages caused by UVB and UVA radiation.

The study of DNA photolability has been a matter of interest over the years. In the early 60s radioactivity-based assays demonstrated the presence of bipyrimidine photoproducts formed between neighboring bases of the same DNA strand: the so-called cyclobutane pyrimidine dimers (CPDs). A decade later, advances in technology allowed, through mass spectrometry and electrophoresis-based assays, the discovery that CPDs were not the only dipyrimidine lesions formed by UV radiation and identified the (6-4) photoproducts (6-4PPs) and their Dewar valence isomers (DewarPPs) (Figure 1.13). [41,42]

The CPDs are formed through a [2+2] photocycloaddition between the C5-C6 double bond of two neighboring pyrimidine bases. Their formation is favored in the UVB range since it is the most energetic UV range reaching the skin and the closest to the DNA absorption maximum. In addition, direct CPD formation has also been observed in human keratinocytes[43],[42] and melanocytes [44] under UVA radiation with a quantum yield 10^3 - 10^4 times lower than under UVB. In this photoreaction different types of diastereoisomers can be formed depending on: *cis or trans* location of the pyrimidine moieties by respect to the cyclobutane ring and *syn or anti* depending on their respective orientation. Nonetheless, in DNA only the *cis*,*syn* isomer can be found due to steric constrains. [45,46] A secondary reaction takes place in CPDs, it corresponds to deamination of the reduced cytosine moiety, which leads to the formation of uracil. [47]

The 6-4PPs are formed through a Paternò-Büchi photoreaction. This reaction starts with a [2+2] cycloaddition between the C5-C6 double bond of the 5'-pyrimidine and the C4 carbonyl group or imine group of a 3'-thymine or cytosine, which leads to an unstable oxetane or azetidine intermediate, respectively. Then, the opening of the heterocycle ends in a covalent bond formation between C6 of the 5'-base and C4 of the 3'-base. Once formed, 6-4PPs can absorb a second photon and undergo an intramolecular electrocyclization of their pyrimidone ring turning into their Dewar valence isomer. [48,49] This reaction has been well documented in model systems but has been observed in very low yields in cells exposed only to UVB. Interestingly, these lesions

exhibit absorption maximum at 325 nm for TT and CT 6-4PPs and at 315 nm for TC and CC 6-4PPs and a residual absorption in the UVA. Indeed, UVB is filtered within the cell due to absorption of biomolecules and endogenous compounds, and which explains the higher yields of photoisomerization when both UVB and UVA photons are used. [50]

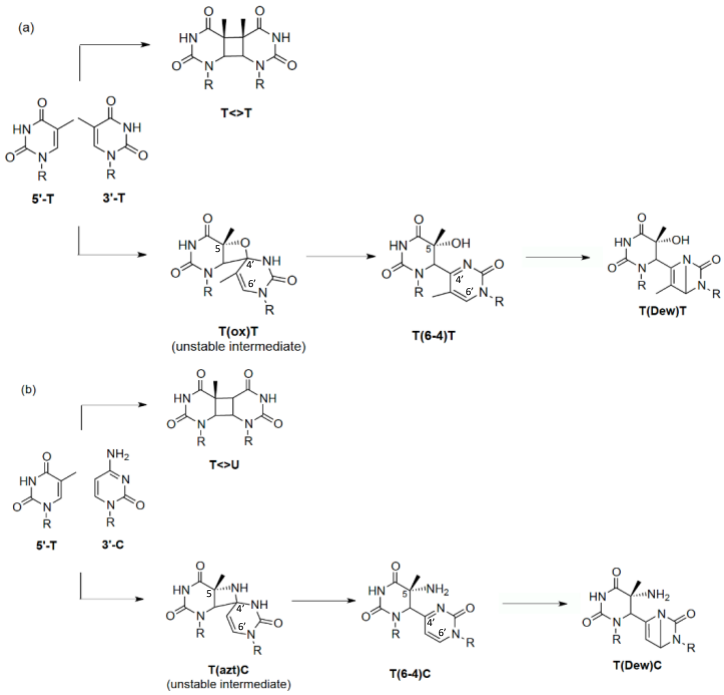

Figure 1. 13. Mechanism of CPDs and 6-4PPs formation for (a) TT and (b) TC sequences.

CPDs are the lesions produced by direct light absorption with the highest frequency rate, whereas 6-4PPs have a formation rate constant three to five times lower. [51,43]. Their formation is sequence-dependent, being TT > TC > CT > CC with a ratio of 10:5:3:1, respectively, as determined in human skin upon UVB irradiation . [51,52,53]

Formation of the dipyrimidine damages can lead to mutation. In this context, CPDs (TT) are less mutagenic than 6-4PPs (TT), even though their formation frequency is higher. This latter is more

mutagenic than its equivalent (TC). [54] The high mutagenicity of CPDs (TC) is due to the deamination process forming CPDs (TU), which during the replication process leads to C →T transitions. [55]

Besides bipyrimidine photoproducts, formation of 8-oxoguanine (8-oxoG) has also been reported for cellular DNA exposed to UVA or UVB light. [56,57] In this case, the proposed mechanism suggests the involvement of the guanine radical cation originated through photoionization, since the ionization potential of this nucleobase is the lowest among the DNA bases. However, 8-oxoG represents a minor photoproduct as its yield is two orders of magnitude lower than that of CPDs. [45] 8-oxoG lesions also exhibit mutagenic properties and are at the origin of G → T transversions.[58]

Interestingly, light not only causes DNA lesions as abovementioned, but it also affects repair processes. Exposure of human keratinocytes and melanocytes to UVB and UVA radiation reduces the rate of elimination of CPDs by polymerase. [42,59]

1.2.2.2. Indirect DNA light absorption

UVA is the most extended region of the ultraviolet reaching the Earth surface. Fortunately, DNA barely absorbs in this region, but it is not innocuous as lesions can be formed by another pathway called photosensitization. In this case, an endogenous or exogenous photosensitizer absorbs light and induces energy transfer (ET), usually TTET, or photoredox processes.

Table 1. 1. Triplet excited state energy of monophosphate nucleobases determined by laser flash photolysis. [40]

	E_T (kJ mol^{-1})
TMP	310
AMP	314
GMP	317
UMP	320
CMP	321

To photosensitize the DNA bases through an ET mechanism the Phs has to fulfill some requirements: (i) it has to absorb light in the UVA or Vis region, at a wavelength higher than 300 nm, to be selectively excited, (ii) its triplet excited state (^{3}Phs) must have an energy (E_T) higher than that of the nucleobase triplet (generally that of thymine, see below), and it must be efficiently populated (ie. a high ISC quantum yield, $\emptyset_{ISC}$), (iii) it should have a long triplet lifetime (τ_T) which enables it to interact with other species, (iv) and finally, the Phs has to be chemically inert under the reaction conditions to avoid its consumption and formation of undesired products. However, this last requirement is not exclusive.

It is well established that triplet-triplet energy transfer takes place through a Dexter-type mechanism, in which the distance between the Phs and the energy acceptor is of maximum 10Å. However, a recent work, where the Phs was covalently inserted within an oligonucleotide, has reported that the energy can be transferred at longer distances of *ca.* 37 Å, [60] suggesting a triplet energy migration along the DNA structure. [61] In this context, it has been proposed since the 60s that energy transfer in DNA takes place from higher to lower lying nucleobase triplet states, and that, excitation tends finally to be localized on thymine residues, which is the nucleotide with the lowest E_T (Table 1. 1). [40]

The damage caused by TTET corresponds exclusively to CPDs. [62] Their formation yield depends on the photophysical properties of the photosensitizer and the nucleobase involved. In this case, CPDs (TT) represent the most abundant combination whereas CPDs (CC), (TC), and (CT) are more unlikely. [63,64]

A large number of endogenous and exogenous photosensitizers have been reported. Exogenous Phs gathered nonsteroidal anti-inflammatory drugs such as the benzophenone derivative ketoprofen,[65,66] solar filters or some antibiotics from the fluoroquinolones family.[63] As endogenous photosensitizers pterins,[67] porphyrins, flavins or melanin have been reported in the literature. [48,68]

In this context, our group has discovered a new class of endogenous Phs.[69] Indeed, UVA/UVB absorbing DNA photolesions can act as intrinsic photosensitizers and induce formation of CPDs, ROS or oxidatively generated damages, which finally ends in the generation of multiple lesions, known as cluster lesions. The 6-4PPs through the 5-methyl-2-pyrimidone chromophore, and some oxidatively generated lesions like 5-formyluracil and 5-formylcytosine can act as Trojan horses and generate CPDs under exposure to light. [69–72]

Not all the Phs mentioned above act through a TTET, they can also be part of Type I or Type II processes and oxidize the DNA. A common DNA photosensitization pathway involves one-electron oxidation which is considered as a Type I mechanism as described before in this chapter (section 1.1.1.2.2). In addition to the abovementioned requirements for a photosensitizer, in this case, one of the main properties which drives the efficiency of the process is the reduction potential of the photosensitizer in its excited state. The main target of Type I oxidation is guanine because it exhibits the lowest ionization potential among all the DNA bases.[73] However, other oxidation photoproducts from the rest of the nucleobases have been reported in lower yields. [74]

Thus, the most frequent oxidatively generated DNA damage comes from guanine and is formed by several processes. One of them is the electron transfer mechanism, which leads to the loss of one electron by guanine and the consequent formation of its radical cation ($G^{\bullet+}$) that evolves into several products. Normally, it undergoes a hydration leading to the 8-hydroxy-7,8-dihydroguanyl radical, which in turn yields 8-oxoG or 2,6-diamino-4-hydroxy-5-formamidopyrimidine (FapyG) by a competitive one-electron oxidation or reduction process, respectively.[74] Additionally, $G^{\bullet+}$ can suffer a hydrogen abstraction at C1 of the sugar giving rise to formation of an abasic site. [75]

Type I photoreaction also involves the formation of hydroxyl radicals ($^{\bullet}OH$), which are highly reactive and do not display any specific DNA target. Their reaction with purine bases gives rise to 8-oxoG, FapyG, 8-oxo-7,8-dihydroadenine (8-oxoA) and 4,6-diamino-5-formamidopyrimidine (FapyA), the last two are generally obtained in lower yields. It has also been reported that $^{\bullet}OH$

mediates the formation of products derived from oxidation of thymine methyl group like 5-hydroxymethyluracil (HmU) and 5-formyluracil (ForU).[76] Besides, $^{\bullet}OH$ interacts with the 2-deoxyribose moieties through a hydrogen abstraction provoking DNA strand break. [77]

It is important to highlight that $^{\bullet}OH$ is not directly formed after light irradiation, and generally results from $O_2^{\bullet-}$ production. The photosensitizer radical anion ($Phs^{\bullet-}$), produced from a Type I process, interacts with molecular oxygen (O_2) releasing superoxide anion ($O_2^{\bullet-}$). This radical anion can also arise from mitochondria as the consequence of UVA irradiation. Next, superoxide dismutase (SOD) catalyzes its dismutation into O_2 and hydrogen peroxide (H_2O_2). This latter is reduced in the presence of Cu^+ or Fe^{2+} (ie. Fenton reaction) to form $^{\bullet}OH$. [73]

A second DNA photooxidation mechanism is the Type II, which involves the formation of singlet oxygen ($^1O_2$). This species shows a strong reaction affinity with molecules rich in double bonds and can easily oxidize biomolecules such as fatty acids, proteins and DNA leading to endoperoxides and dioxetanes as products of this oxidation. [78] In DNA, guanine is the only target of $^1O_2$. The reaction involves a Diels Alder [4+2] photocycloaddition that forms a 4,8-endoperoxide, which is reduced to 8-oxoG. [79]

1.3. DNA REPAIR PROCESSES

As described before, DNA damages are occurring in humans with non-negligible yields, being their frequency rates around 10^4 - 10^6 per cell per day per type of damage. As a consequence, they represent a threat to genome integrity. However, to maintain the genome, humans have their own repair mechanisms based on DNA repair enzymes that efficiently repair around 10^{16} - 10^{18} per cell per day. [40]

When a cell is damaged, its cycle slows down, which can be beneficious in terms of repair, since it provides more time to the DNA repair machinery before replication and cell division. However, if a large number of lesions are present or some specific errors occur during repair process, the cell can undergo apoptosis

(ie. programmed cell death). [80] If any of these protection measures fails, the lesion remains in the DNA sequence and may cause mutations during the replication process, which may finally result in the appearance of cancer.

1.3.1. DARK DNA REPAIR MECHANISMS

1.3.1.1. Common DNA repair mechanisms

The most common repair mechanism in mammals is excision repair. It includes three different types of systems: Base Excision Repair (BER), Nucleotide Excision Repair (NER) and Base Mismatch Repair (MMR).

BER acts on small DNA modifications that arise from alkylation, deamination or oxidation. [81] This mechanism involves a set of enzymes. First, a DNA glycosylase cleaves the glycosidic bond of the modified base to generate an abasic site. This enzyme is base-specific and has several types depending on the lesion it recognizes. For example, Uracil DNA glycosylase (UDG) is involved in the replacement of uracil by thymine, 3-methyladenine-DNA glycosylase recognizes alkylated lesions like 3-methyladenine or guanosine, whereas OGG1 DNA glycosylase cleaves specifically one of the major mutagenic lesions, 8-oxoG.

Secondly, an incision of the phosphate backbone is produced by an AP endonuclease removing specific modified nucleobases and leaving a gap with a 3'-end -OH and a 5'-end ribosyl-phosphate. Then, the resulting abasic site is filled by a polymerase with a short-patch (just one nucleotide is replaced) or a long-patch (where 2-10 nucleotides are newly synthesized by the DNA polymerase) and finally, ligase seals this new patch. The repair process takes place in a short period of time, for example, BER repairs 8-oxoG lesions within few hours after its formation. [82]

Concerning NER mechanism, it mainly repairs bulky lesions including adducts, intrastrand crosslinks and those formed by direct UV light absorption such as CPDs and 6-4PPs. The procedure for NER is similar to BER, it works through a cut-and-patch mechanism but the main difference is that NER removes chains

between 24 and 32 nucleotides long. Moreover, NER has two signaling pathways: one the Global Genomic Repair (GGR) and the Transcription-Coupled Repair (TCR). Both ways employ several signaling proteins that detect the lesions; [83] however, TCR is restrained to lesions in the transcribed strand of active genes whereas GGR acts on the whole gene.

As for BER, in NER after the first excision step performed by TCR or GGR, the resulting gap is filled by DNA polymerases and fixed by the DNA ligase.

The last excision repair mechanism is the DNA Mismatch Repair (MMR), this mechanism is mainly centered on the repair of mismatch lesions arising from erroneous polymerase activity after the replication process. Its main targets in mammalians cells are G→T, A→C, G→G, and C→C and also some mismatches originating from oxidatively generated lesions like O^6-methylguanine with thymine or cytosine. [84] In the first step of the repair process, recognition and cleavage are performed by heterodimeric complexes called MutSα or MutSβ, which are formed by the proteins MSH2 and MSH6 for MutSα and MSH2 and MSH3 for MutSβ. [85] After, ATP hydrolysis forms a loop in the structure followed by its degradation and elongation due to the 5'-3' exonuclease and helicase enzymes. Finally, the gap is filled by DNA polymerase δ and sealed by the DNA ligase. MMR is associated with gastrointestinal and endometrial cancer. [40]

Although, most DNA damages are repaired by excision mechanisms followed by insertion of the right base, some lesions can be restored *in situ* by specific proteins through the so-called direct repair (Figure 1.14). In this context, dealkylation of nucleobases takes place through methyltransferase enzymes, such as the O^6-methylguanine-DNA methyltransferase (MGMT) that acts by transferring the methyl group anchored in O^6-alkyl guanines to its cysteine residue. [86] Double-stranded DNA breaks (DSB), are mainly repaired through the non-homologous DNA end joining (NHEJ) pathway. In this mechanism, a circular protein with a heterodimeric complex called Ku70/Ku80 recognizes the DSB and binds the broken ends using the DNA-Protein Kinase catalytic subunit PKcs, which acts as a bridge to bring the two ends of the phosphate backbone together. Finally, a DNA ligase joins them. [87]

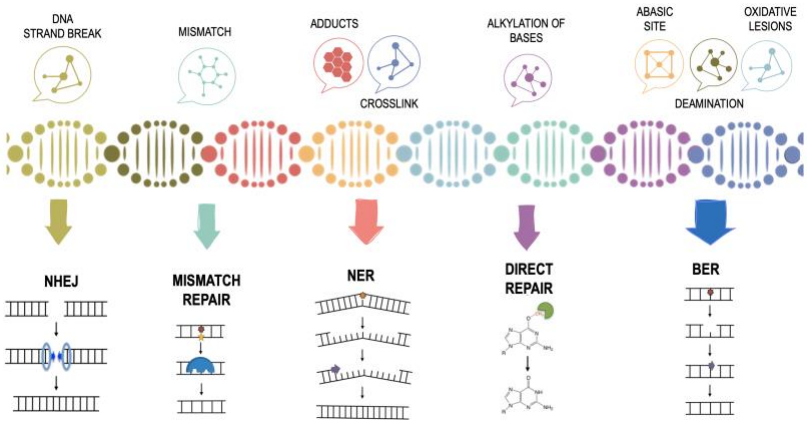

Figure 1. 14. Dark repair processes.

1.3.1.2. Direct repair mechanism: AlkB protein

DNA-glycosylase was firstly proposed as the principal enzyme for the repair since *in vitro* studies in human cells reported its activity towards εdA and εdG. [88–90] However, over time it has been demonstrated that repair of ε-adducts is not governed only by BER process, but that they are also vulnerable to direct repair. [91] Indeed, direct repair is the main mechanism in bacteria through the action of the AlkB protein. This protein is a α-ketoglutarate dioxygenase belonging to the family of the non-heme iron-dependent oxygenases, it catalyzes the incorporation of molecular oxygen into biological substrates.

In crystallographic studies of AlkB-double stranded DNA complexes under aerobic conditions and in presence of a εA containing sequences have captured the formation of an εA-glycol intermediate (Figure 1. 15) [92,93] This observation points towards an epoxidation step followed by ring opening after water attack and subsequent protonation finally leading to the original adenine nucleobase. The repair process involves the coordination of 2-oxoglutarate (αKG) and molecular oxygen with Fe^{2+} bound to the enzyme. One oxygen would be subsequently added to the target and the second oxygen atom is transferred to 2-oxoglutarate producing carbon dioxide and succinate.

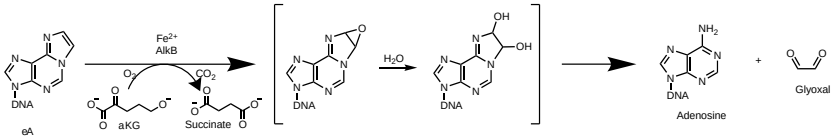

Figure 1. 15. Repair process of εdA through AlkB protein.

Despite AlkB presents an interaction for all the etheno adducts, this enzyme is found only in bacteria and its role in εG repair is still under discussion. Interestingly, in mammals, its counterpart enzymes, which are part of the AlkBH family, present a poor etheno adducts repair effectiveness. Only AlkBH2 has been reported to repair εA and εG in dsDNA, whereas AlkBH3 is the only active enzyme for εC [94,95]

In this thesis, the photolability of etheno adducts is addressed. Their ability to suffer photooxidation will be assessed in order to mimic the repair process of AlkB protein and investigate a new strategy based on a light-triggered recovering of the original base.

1.3.2. LIGHT-DEPENDENT DNA REPAIR MECHANISMS

Photoreactivation was discovered by Kelner in the mid-20th century. He observed how the lethal effect of UV radiation on *Streptomyces griseus* was reversed when, following the harmful UV radiation, the irradiated bacterial culture was exposed to visible light. [96] Resurrection of these UV light-killed cells by light is due to the action of enzymes named photolyases. These peculiar enzymes are flavoproteins, which are able to repair *in situ* the two main UV-derived lesions, ie. the bipyrimidine dimers, using blue light as a co-substrate. Mechanistically, there are two main types of photolyases depending on the type of lesion they repair: enzymes that repair CPDs are referred to as CPD photolyase, while enzymes that repair (6-4) photoproducts are called (6-4) photolyase. [97,98]

These proteins are present in several organisms. For instance, CPD photolyase has been found in bacteria, viruses, fungi and some invertebrates and even in certain placental mammals. For (6-4) photolyase, it has been detected in some insects and animals like silkworm, frogs (*Xenopus Laevis*) and rattlesnakes. However, photolyase is lacking in humans although some flavoprotein homologs called cryptochromes are involved in light-regulated functions, but they do not repair DNA lesions. [99]

The CPD and (6-4) photolyases are 55 kDa enzymes that share the same cofactors at their active site. A first cofactor is a flavin adenine dinucleotide (FAD) which is responsible for the repair process, whereas the second cofactor is 8-hydroxy-5-deazaflavin (8-HDF, Figure 1. 16) or 5,10-methenyltetrahydrofolate (MTHF, Figure 1. 16) those chromophores act as a light-harvesting antenna and trigger the photorepair process.

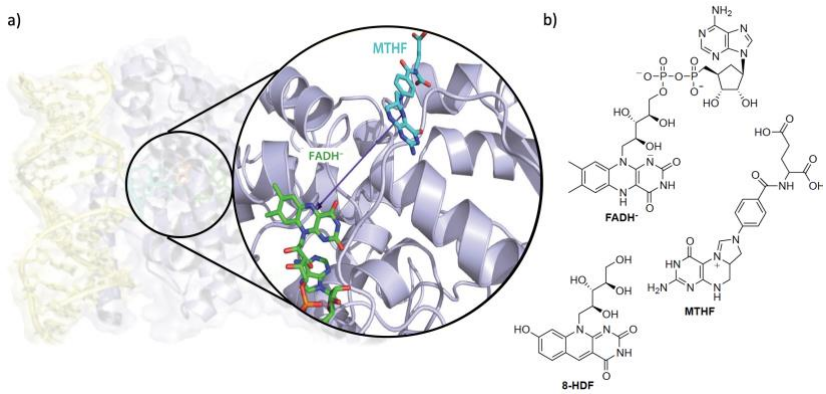

Figure 1. 16. a) Crystal structure of the CPD photolyase. b) Structure of the different cofactors.

FAD can be present in three different redox states corresponding to fully oxidized (FAD_{ox}), semi-reduced ($FADH^{\bullet}$) and fully reduced ($FADH^{-}$, Figure 1. 16). But only the $FADH^{-}$ is the catalytically active form responsible for the bipyrimidine repair. [100,101] The other two cofactors (FADox and $FADH^{\bullet}$) can be converted to the active $FADH^{-}$ by means of a photoinduced process called photoactivation that typically involves an intraprotein electron transfer through a chain of three tryptophans. [101,102]

1.3.2.1. CPD Photolyase mechanism

Repair mechanism by CPD photolyase (Figure 1. 17a) is well established. [102] The enzyme recognizes the CPD lesion and flips it out of the double helix towards its active center. Photoexcitation of $FADH^-$ is achieved after photon absorption by 8-HDF or MTHF, that has a wider absorption in the visible range than $FADH^-$; it is followed by energy transfer to the $FADH^-$ cofactor. Then, an electron transfer occurs from the excited $^1FADH^{-*}$ to the CPD inducing the formation of the semi-reduced $FADH^\bullet$ and of the CPD radical anion, which rapidly suffers the splitting of C5-C6 bond leading to one intact base and the radical anion of the other one. The latter transfers back its extra electron to the flavin closing the catalytic cycle restoring $FADH^-$ and giving rise to the repaired lesion. The process takes around 50 μs [103] and the enzyme is regenerated and ready to bind another CPD. This repair process has a high quantum yield of *ca.* 0.7-0.9 [97] in contrast with (6-4) photolyase which is much lower *ca.* 0.1. [104]

1.3.2.2. (6-4) Photolyase mechanism

The mechanism behind (6-4) photolyase repair is still under study. Indeed, the molecular process responsible for restoring the original nucleobases is not as direct as in the case of CPD, because it requires an NH_2 or OH group transfer from 5' to the 3' nucleobase. Several mechanisms have been proposed along the years. The first theory suggested thermal formation of an oxetane intermediate. [97] However, in 2008 a crystal structure of a *Drosophila Melanogaster* (6-4) photolyase bound to a 6-4PP (T-T) lesion was solved. [105] Unexpectedly, the formation of the oxetane in a dark step was not observed, and, irradiation of the crystal showed repair of the (6-4) lesion without large changes of the structure pointing toward a direct electron transfer to one of the 6-4PP moieties as possible repair mechanism. In 2010, ultrafast fluorescence and transient absorption spectroscopy studies on a (6-4) photolyase from an *Arabidopsis Thaliana* support this proposal. [106] The photorepair cycle (Figure 1. 17b) begins with an electron transfer

from the $^{1}FADH^{-}$, which has been excited by the antenna cofactor 8-HDF or MTHF, to the 6-4PP in 225 ps. This first stage is identical to the one described for the CPD photolyase. Then, a proton transfer from a protonated histidine moiety (His365) occurs in 425 ps and leads, after oxygen-atom at C4 attacks the 3' base, to the transient zwitterion (III, in Figure 1. 17b), which has an oxetane-like structure. This finally rearranges to the repaired pyrimidine bases returning an electron to the $FADH^{\bullet}$, which closes the catalytic cycle and allows starting the process with a new 6-4PP lesion. [102]

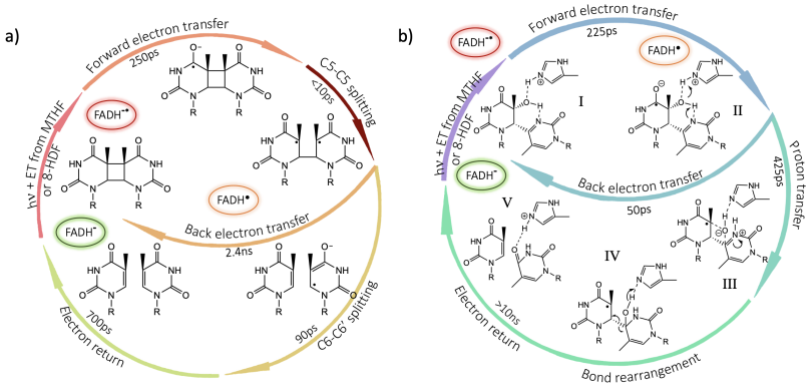

Figure 1. 17. Proposed photolyase mechanism a) CPD photolyase and b) 6-4 photolyase.

The low quantum yield of the process (*ca.* 0.1) has been interpreted as the result of competition between the fast back electron transfer (50 ps) of radical anion (II, in Figure 1. 17b), leading to the original 6-4PP, and protonation of II in 425 ps, as a step of the productive repair process. Indeed, in CPD photolyases back electron transfer is much slower (2.4 ns, Figure 1. 17a), which could explain the higher quantum yield of repair of these enzymes compared to (6-4) photolyases.

Computational studies foreshadow several possible mechanisms, one of them involves a two photon absorption. [107] Experimental results have supported this proposal. An approach, using non-saturating 100-ps laser flashes, has been designed to distinguish between a one- and a two photon repair process. It has

been observed that the first flash depleted the 6-4PP without leading to substantial repair, but, subsequent flashes resulted in the base recovery. It has been proposed that the first flash leads to the formation of an unstable intermediate with a lifetime of 100 s at 10ºC, which might correspond to an oxetane as it thermally reverts to the lesion or under another photon absorption yields to the restored bases. [102,108]

1.4. REFERENCES

(1) Albini, A. Some Remarks on the First Law of Photochemistry. *Photochem. Photobiol. Sci. 2016 153* **2016**, *15* (3), 319–324.

(2) Valeur, B.; Molecular Fluorescence: Principles and Applications; *Wiley-VCH Verlag*, **2001**.

(3) McNaught, A. D.; Wilkinson, A. Golden book of IUPAC-Compendium of Chemical Terminology.

(4) Turro, N. J.; Modern Molecular Photochemistry; *Columbia University*, **1991**.

(5) Verma, M.; Chaudhry, A. F.; Fahrni, C. J. Predicting the Photoinduced Electron Transfer Thermodynamics in Polyfluorinated 1,3,5-Triarylpyrazolines Based on Multiple Linear Free Energy Relationships. *Org. Biomol. Chem.* **2009**, *7* (8), 1536–1546.

(6) DeRosa, M. C.; Crutchley, R. J. Photosensitized Singlet Oxygen and Its Applications. *Coord. Chem. Rev.* **2002**, *233–234*, 351–371.

(7) Merkel, P. B.; Kearns, D. R. Remarkable Solvent Effects on the Lifetime of $^1\Delta_g$ Oxygen. *J. Am. Chem. Soc.* **2002**, *94* (3), 1029–1030.

(8) Tubbs, A.; Nussenzweig, A. Endogenous DNA Damage as a Source of Genomic Instability in Cancer. *Cell* **2017**, *168* (4), 644–656.

(9) Robinson, A. R.; Yousefzadeh, M. J.; Rozgaja, T. A.; Wang, J.; Li, X.; Tilstra, J. S.; Feldman, C. H.; Gregg, S. Q.; Johnson, C. H.; Skoda, E. M.; Frantz, M. C.; Bell-Temin, H.; Pope-Varsalona, H.; Gurkar, A. U.; Nasto, L. A.; Robinson, R. A. S.; Fuhrmann-Stroissnigg, H.; Czerwinska, J.; McGowan, S. J.; Cantu-Medellin, N.; Harris, J. B.; Maniar, S.; Ross, M. A.; Trussoni, C. E.; LaRusso, N. F.; Cifuentes-Pagano, E.;

Pagano, P. J.; Tudek, B.; Vo, N. V.; Rigatti, L. H.; Opresko, P. L.; Stolz, D. B.; Watkins, S. C.; Burd, C. E.; Croix, C. M. S.; Siuzdak, G.; Yates, N. A.; Robbins, P. D.; Wang, Y.; Wipf, P.; Kelley, E. E.; Niedernhofer, L. J. Spontaneous DNA Damage to the Nuclear Genome Promotes Senescence, Redox Imbalance and Aging. *Redox Biol.* **2018**, *17*, 259–273.

(10) Yousefzadeh, M. J.; Zhao, J.; Bukata, C.; Wade, E. A.; McGowan, S. J.; Angelini, L. A.; Bank, M. P.; Gurkar, A. U.; McGuckian, C. A.; Calubag, M. F.; Kato, J. I.; Burd, C. E.; Robbins, P. D.; Niedernhofer, L. J. Tissue Specificity of Senescent Cell Accumulation during Physiologic and Accelerated Aging of Mice. *Aging Cell* **2020**, *19* (3), 13094-13117.

(11) Yousefzadeh, M.; Henpita, C.; Vyas, R.; Soto-Palma, C.; Robbins, P.; Niedernhofer, L. DNA Damage—How and Why We Age? *Elife* **2021**, *10*, 1–17.

(12) Ganai, R. A.; Johansson, E. DNA Replication—A Matter of Fidelity. *Mol. Cell* **2016**, *62* (5), 745–755.

(13) Khanna, K. K.; Jackson, S. P. DNA Double-Strand Breaks: Signaling, Repair and the Cancer Connection. *Nat. Genet.* **2001**, *27* (3), 247–254.

(14) Noll, D. M.; McGregor Mason, T.; Miller, P. S. Formation and Repair of Interstrand Cross-Links in DNA. *Chem. Rev.* **2005**, *106* (2), 277–301.

(15) Kuzminov, A. Pyrimidine Dimers. *Brenner's Encycl. Genet. Second Ed.* **2013**, 538–539.

(16) Pujol, J. L.; Carestia; Daurès, J. P. Is There a Case for Cisplatin in the Treatment of Small-Cell Lung Cancer? A Meta-Analysis of Randomized Trials of a Cisplatin-Containing Regimen versus a Regimen without This Alkylating Agent. *Br. J. Cancer* **2000**, *83* (1), 8–15.

(17) Flatt, P. Biochemistry: Defining Life at the Molecular Level,

Western Oregon University, **2019**.

(18) Wu, X.; Zhang, Y. TET-Mediated Active DNA Demethylation: Mechanism, Function and Beyond. *Nat. Rev. Genet.* **2017**, *18* (9), 517–534.

(19) Herzog, V. A.; Reichholf, B.; Neumann, T.; Rescheneder, P.; Bhat, P.; Burkard, T. R.; Wlotzka, W.; Von Haeseler, A.; Zuber, J.; Ameres, S. L. Thiol-Linked Alkylation of RNA to Assess Expression Dynamics. *Nat. Methods* **2017**, *14* (12), 1198–1204.

(20) Liu, S.; Wang, Y. Mass Spectrometry for the Assessment of the Occurrence and Biological Consequences of DNA Adducts. *Chem. Soc. Rev.* **2015**, *44* (21), 7829–7854.

(21) Guo, J.; Turesky, R. J. Emerging Technologies in Mass Spectrometry-Based DNA Adductomics. *High-Throughput 2019, Vol. 8, Page 13* **2019**, *8* (2), 13.

(22) Hu, W.; Feng, Z.; Eveleigh, J.; Iyer, G.; Pan, J.; Amin, S.; Chung, F.-L.; Tang, M.-S. The Major Lipid Peroxidation Product, Trans-4-Hydroxy-2-Nonenal, Preferentially Forms DNA Adducts at Codon 249 of Human P53 Gene, a Unique Mutational Hotspot in Hepatocellular Carcinoma. *Carcinogenesis* **2002**, 23(11), 1781–1789.

(23) Basu, A. K.; Wood, M. L.; Niedernhofer, L. J.; Ramos, L. A.; Essigmann, J. M. Mutagenic and Genotoxic Effects of Three Vinyl Chloride-Induced DNA Lesions: 1,N6-Ethenoadenine, 3,N4-Ethenocytosine, and 4-Amino-5-(Imidazol-2-Yl)Imidazole, *Biochemistry* **1993**, 32, 12793-12801.

(24) Chung, F. L.; Chen, H. J. C.; Nath, R. G. Lipid Peroxidation as a Potential Endogenous Source for the Formation of Exocyclic DNA Adducts. *Carcinogenesis* **1996**, *17* (10), 2105–2111..

(25) Fernando, R. C.; Nair, J.; Barbin, A.; Miller, J. A.; Bartsch, H.

Detection of 1, N6 -Ethenodeoxyadenosine and 3, N4 -Ethenodeoxycytidine by Immunoaffinity/ 32 P-Post-Labelling in Liver and Lung DNA of Mice Treated with Ethylcarbamate (Urethane) or Its Metabolites. *Carcinogenesis* **1996**, *17* (8), 1711–1718.

(26) Ghissassi, F. El; Barbin, A.; Nair, J.; Bartsch, H.; El Ghissassi, F.; Barbin, A.; Nair, J.; Bartsch, H. Formation of 1,N6-Ethenoadenine and 3,N4-Ethenocytosine by Lipid Peroxidation Products and Nucleic Acid Bases., *American Chemical Society*, **2002**, 8, 278-283.

(27) Tudek, B.; Zdżalik-Bielecka, D.; Tudek, A.; Kosicki, K.; Fabisiewicz, A.; Speina, E. Lipid Peroxidation in Face of DNA Damage, DNA Repair and Other Cellular Processes. *Free Radic. Biol. Med.* **2017**, *107*, 77–89.

(28) Rioux, K. L.; Delaney, S. 1,N6-Ethenoadenine: From Molecular to Biological Consequences. *Chem. Res. Toxicol.* **2020**, *33* (11), 2688–2698.

(29) Chen, H.; Krishnamachari, S.; Guo, J.; Yao, L.; Murugan, P.; Weight, C. J.; Turesky, R. J. Quantitation of Lipid Peroxidation Product DNA Adducts in Human Prostate by Tandem Mass Spectrometry: A Method That Mitigates Artifacts. *Chem. Res. Toxicol.* **2019**, *32* (9), 1850–1862.

(30) Bartsch, H.; Nair, J.; Owen, R. W. Exocyclic DNA Adducts as Oxidative Stress Markers in Colon Carcinogenesis: Potential Role of Lipid Peroxidation, Dietary Fat and Antioxidants. *Biol. Chem.* **2002**, *383* (6), 915–921.

(31) Hecht, S. S. Oral Cell DNA Adducts as Potential Biomarkers for Lung Cancer Susceptibility in Cigarette Smokers. *Chem. Res. Toxicol.* **2016**, *30* (1), 367–375.

(32) Levine, R. L.; Yang, I.-Y.; Hossain, M.; Pandya, G. A.; Grollman, A. P.; Moriya, M. Mutagenesis Induced by a Single 1,N6-Ethenodeoxyadenosine Adduct in Human Cells. *Cancer Res.* **2000**, *60* (15), 4098 – 4104.

(33) Nair, U.; Bartsch, H.; Nair, J. Lipid Peroxidation-Induced DNA Damage in Cancer-Prone Inflammatory Diseases: A Review of Published Adduct Types and Levels in Humans. *Free Radic. Biol. Med.* **2007**, *43* (8), 1109–1120.

(34) Nair, J.; Srivatanakul, P.; Haas, C.; Jedpiyawongse, A.; Khuhaprema, T.; Seitz, H. K.; Bartsch, H. High Urinary Excretion of Lipid Peroxidation-Derived DNA Damage in Patients with Cancer-Prone Liver Diseases. *Mutat. Res. Mol. Mech. Mutagen.* **2010**, *683* (1–2), 23–28.

(35) Yu, Y.; Cui, Y.; Niedernhofer, L. J.; Wang, Y. Occurrence, Biological Consequences, and Human Health Relevance of Oxidative Stress-Induced DNA Damage. *Chemical Research in Toxicology* **2016**, 29 (12), 2008–2039.

(36) Barbin, A.; Bartsch, H.; Leconte, P.; Radman, M. Studies on the Miscoding Properties of 1,N 6 -Ethenoadenine and 3,N 4 -Ethenocytosine, DNA Reaction Products of Vinyl Chloride Metabolites, during in Vitro DNA Synthesis. *Nucleic Acids Res.* **1981**, *9* (2), 375–387.

(37) Freisinger, E.; Fernandes, A.; Grollman, A. P.; Kisker, C. Crystallographic Characterization of an Exocyclic DNA Adduct: 3,N4-Etheno-2'-Deoxycytidine in the Dodecamer 5'-CGCGAATTεCGCG-3'. *J. Mol. Biol.* **2003**, *329* (4), 685–697.

(38) Kouchakdjian, M.; Patel, D. J.; Eisenberg, M.; Yarema, K.; Basu, A.; Essigmann, J. NMR Studies of the Exocyclic 1,N6-Ethenodeoxyadenosine Adduct (EdA) Opposite Thymidine in a DNA Duplex. Nonplanar Alignment of EdA(Anti) and DT(Anti) at the Lesion Site. *Biochemistry* **1991**, *30* (7), 1820–1828.

(39) World Health Organization. Ultraviolet radiation (UV) https://www.who.int/data/gho/data/themes/topics/topic-details/GHO/ultraviolet-(uv)-radiation.

(40) DNA Photodamage. From Light Absorption to Cellular

Response and Skin Cancer., Improta, R.; Douki, T.; Eds.*; Royal Society of Chemistry*, **2021**.

(41) Cadet, J.; Berger, M.; Douki, T.; Morin, B.; Raoul, S.; Ravanat, J. L.; Spinelli, S. Effects of UV and Visible Radiation on DNA-Final Base Damage. *Biol. Chem.* **1997**, *378* (11), 1275–1286.

(42) Courdavault, S.; Baudouin, C.; Charveron, M.; Canguilhem, B.; Favier, A.; Cadet, J.; Douki, T. Repair of the Three Main Types of Bipyrimidine DNA Photoproducts in Human Keratinocytes Exposed to UVB and UVA Radiations. *DNA Repair (Amst).* **2005**, *4* (7), 836–844.

(43) Perdiz, D.; Grof, P.; Mezzina, M.; Nikaido, O.; Moustacchi, E.; Sage, E. Distribution and Repair of Bipyrimidine Photoproducts in Solar UV-Irradiated Mammalian Cells: Possible Role of Dewar Photoproducts in Solar Mutagenesis. *J. Biol. Chem.* **2000**, *275* (35), 26732–26742.

(44) Mouret, S.; Forestier, A.; Douki, T. The Specificity of UVA-Induced DNA Damage in Human Melanocytes. *Photochem. Photobiol. Sci. 2012 111* **2012**, *1* (11), 155–162.

(45) Ravanat, J. L.; Douki, T.; Cadet, J. Direct and Indirect Effects of UV Radiation on DNA and Its Components. *J. Photochem. Photobiol. B.* **2001**, *63* (1–3), 88–102.

(46) Douki, T. The Variety of UV-Induced Pyrimidine Dimeric Photoproducts in DNA as Shown by Chromatographic Quantification Methods. *Photochem. Photobiol. Sci.* **2013**, *12* (8), 1286–1302.

(47) Jin, S. G.; Pettinga, D.; Johnson, J.; Li, P.; Pfeifer, G. P. The Major Mechanism of Melanoma Mutations Is Based on Deamination of Cytosine in Pyrimidine Dimers as Determined by Circle Damage Sequencing. *Sci. Adv.* **2021**, *7* (31), 1-13.

(48) Douki, T. Pyrimidine (6-4) Pyrimidone Photoproducts in

UVA-irradiated DNA: Photosensitization or Photoisomerization? *ChemPhotoChem* **2020**, *4* (4), 294–299.

(49) Haiser, K.; Fingerhut, B. P.; Heil, K.; Glas, A.; Herzog, T. T.; Pilles, B. M.; Schreier, W. J.; Zinth, W.; De Vivie-Riedle, R.; Carell, T.; Heil,] K; Glas, + A; Carell, T.; Fingerhut, B. P.; De Vivie-Riedle, R.; Haiser, K.; Herzog, T. T.; Pilles, B. M.; Schreier, W. J.; Zinth, W. Mechanism of UV-Induced Formation of Dewar Lesions in DNA. *Angew. Chemie Int. Ed.* **2012**, *51* (2), 408–411.

(50) Taylor, J. S.; Cohrs, M. P. DNA, Light, and Dewar Pyrimidinones: The Structure and Biological Significance to TpT3. *J. Am. Chem. Soc.* **1987**, *109* (9), 2834–2835.

(51) Courdavault, S.; Baudouin, C.; Sauvaigo, S.; Mouret, S.; Candeias, S.; Charveron, M.; Favier, A.; Cadet, J.; Douki, T. Unrepaired Cyclobutane Pyrimidine Dimers Do Not Prevent Proliferation of UV-B-Irradiated Cultured Human Fibroblasts. *Photochem. Photobiol.* **2004**, *79* (2), 145–151.

(52) Douki, T.; Cadet, J. Individual Determination of the Yield of the Main UV-Induced Dimeric Pyrimidine Photoproducts in DNA Suggests a High Mutagenicity of CC Photolesions. *Biochemistry* **2001**, *40* (8), 2495–2501.

(53) Bastien, N.; Therrien, J. P.; Drouin, R. Cytosine Containing Dipyrimidine Sites Can Be Hotspots of Cyclobutane Pyrimidine Dimer Formation after UVB Exposure. *Photochem. Photobiol. Sci.* **2013**, *12* (8), 1544–1554.

(54) LeClerc, J. E.; Borden, A.; Lawrence, C. W. The Thymine-Thymine Pyrimidine-Pyrimidone(6-4) Ultraviolet Light Photoproduct Is Highly Mutagenic and Specifically Induces 3' Thymine-to-Cytosine Transitions in Escherichia Coli. *Proc. Natl. Acad. Sci.* **1991**, *88* (21), 9685–9689.

(55) Shen, Y.; Ha, W.; Zeng, W.; Queen, D.; Liu, L. Exome Sequencing Identifies Novel Mutation Signatures of UV Radiation and Trichostatin A in Primary Human

Keratinocytes. *Sci. Reports,* **2020**, *10* (1), 1–12.

(56) Pouget, J. P.; Douki, T.; Richard, M. J.; Cadet, J. DNA Damage Induced in Cells by γ and UVA Radiation As Measured by HPLC/GC−MS and HPLC−EC and Comet Assay. *Chem. Res. Toxicol.* **2000**, *13* (7), 541–549.

(57) Gomez-Mendoza, M.; Banyasz, A.; Douki, T.; Markovitsi, D.; Ravanat, J. L. Direct Oxidative Damage of Naked DNA Generated upon Absorption of UV Radiation by Nucleobases. *J. Phys. Chem. Lett.* **2016**, *7* (19), 3945–3948.

(58) Tan, X.; Grollman, A. P.; Shibutani, S. Comparison of the Mutagenic Properties of 8-Oxo-7,8-Dihydro-2'-Deoxyadenosine and 8-Oxo-7,8-Dihydro-2'-Deoxyguanosine DNA Lesions in Mammalian Cells. *Carcinogenesis* **1999**, *20* (12), 2287–2292.

(59) Kimeswenger, S.; Dingelmaier-Hovorka, R.; Foedinger, D.; Jantschitsch, C. UVA1 Impairs the Repair of UVB-Induced DNA Damage in Normal Human Melanocytes. *Exp. Dermatol.* **2018**, *27* (3), 276–279.

(60) Miro, P.; Gomez-Mendoza, M.; Sastre, G.; Cuquerella, M. C.; Miranda, M. A.; Marin, M. L. Generation of the Thymine Triplet State by Through-Bond Energy Transfer. *Chem. – A Eur. J.* **2019**, *25* (28), 7004–7011.

(61) Antusch, L.; Gaß, N.; Wagenknecht, H. A. Elucidation of the Dexter-Type Energy Transfer in DNA by Thymine–Thymine Dimer Formation Using Photosensitizers as Artificial Nucleosides. *Angew. Chemie Int. Ed.* **2017**, *56* (5), 1385–1389.

(62) Consuelo Cuquerella, M.; Lhiaubet-Vallet, V.; Bosca, F.; Miranda, M. A. Photosensitised Pyrimidine Dimerisation in DNA. *Chem. Sci.* **2011**, *2* (7), 1219–1232.

(63) Lhiaubet-Vallet, V.; Bosca, F.; Miranda, M. A. Photosensitized DNA Damage: The Case of

Fluoroquinolones. *Photochem. Photobiol.* **2009**, *85* (4), 861–868.

(64) Douki, T.; Bérard, I.; Wack, A.; Andrä, S. Contribution of Cytosine-Containing Cyclobutane Dimers to DNA Damage Produced by Photosensitized Triplet–Triplet Energy Transfer. *Chem. – A Eur. J.* **2014**, *20* (19), 5787–5794.

(65) Boscá, F.; Marín, M. L.; Miranda, M. A. Photoreactivity of the Nonsteroidal Anti-Inflammatory 2-Arylpropionic Acids with Photosensitizing Side Effects. *Photochem. Photobiol.* **2001**, *74* (5), 637–655.

(66) Monteiro, A. F.; Rato, M.; Martins, C. Drug-Induced Photosensitivity: Photoallergic and Phototoxic Reactions. *Clin. Dermatol.* **2016**, *34* (5), 571–581.

(67) Dantola, M. L.; Vignoni M.; Serrano M. P.; Lorente, C.; Thomas, A. H. Oxidation of biomolecules photosensitized by pterin derivatives. *An. Asoc. Quim. Argent.* **2020**, 107(2), 164-187.

(68) Noonan, F. P.; Zaidi, M. R.; Wolnicka-Glubisz, A.; Anver, M. R.; Bahn, J.; Wielgus, A.; Cadet, J.; Douki, T.; Mouret, S.; Tucker, M. A.; Popratiloff, A.; Merlino, G.; De Fabo, E. C. Melanoma Induction by Ultraviolet A but Not Ultraviolet B Radiation Requires Melanin Pigment. *Nat. Commun.* **2012**, *3* (1), 1–10.

(69) Vendrell-Criado, V.; Rodríguez-Muñiz, G. M.; Cuquerella, M. C.; Lhiaubet-Vallet, V.; Miranda, M. A. Photosensitization of DNA by 5-Methyl-2-Pyrimidone Deoxyribonucleoside: (6-4) Photoproduct as a Possible Trojan Horse. *Angew. Chemie Int. Ed.* **2013**, *52* (25), 6476–6479.

(70) Aparici-Espert, I.; Garcia-Lainez, G.; Andreu, I.; Miranda, M. A.; Lhiaubet-Vallet, V. Oxidatively Generated Lesions as Internal Photosensitizers for Pyrimidine Dimerization in DNA. *ACS Chem. Biol.* **2018**, *13* (3), 542–547.

(71) Lineros-Rosa, M.; Francés-Monerris, A.; Monari, A.; Miranda, M. A.; Lhiaubet-Vallet, V. Experimental and Theoretical Studies on Thymine Photodimerization Mediated by Oxidatively Generated DNA Lesions and Epigenetic Intermediates. *Phys. Chem. Chem. Phys.* **2020**, *22* (44), 25661–25668.

(72) Francés-Monerris, A.; Lineros-Rosa, M.; Miranda, M. A.; Lhiaubet-Vallet, V.; Monari, A. Photoinduced Intersystem Crossing in DNA Oxidative Lesions and Epigenetic Intermediates. *Chem. Commun.* **2020**, *56* (32), 4404–4407.

(73) Cadet, J.; Mouret, S.; Ravanat, J. L.; Douki, T. Photoinduced Damage to Cellular DNA: Direct and Photosensitized Reactions. *Photochem. Photobiol.* **2012**, *88* (5), 1048–1065.

(74) Cadet, J.; Douki, T.; Ravanat, J. L.; Di Mascio, P. Sensitized Formation of Oxidatively Generated Damage to Cellular DNA by UVA Radiation. *Photochem. Photobiol. Sci.* **2009**, *8* (7), 903–911.

(75) Paris, C.; Encinas, S.; Belmadoui, N.; Climent, M. J.; Miranda, M. A. Photogeneration of 2-Deoxyribonolactone in Benzophenone-Purine Dyads. Formation of Ketyl-C1' Biradicals. *Org. Lett.* **2008**, *10* (20), 4409–4412.

(76) Pogozelski, W. K.; Tullius, T. D. Oxidative Strand Scission of Nucleic Acids: Routes Initiated by Hydrogen Abstraction from the Sugar Moiety. *Chem. Rev.* **1998**, *98* (3), 1089–1107.

(77) Balasubramanian, B.; Pogozelski, W. K.; Tullius, T. D. DNA Strand Breaking by the Hydroxyl Radical Is Governed by the Accessible Surface Areas of the Hydrogen Atoms of the DNA Backbone. *Proc. Natl. Acad. Sci.* **1998**, *95* (17), 9738–9743.

(78) Singlet Oxygen: Applications in Biosciences and Nanosciences. Vol. 1.; Nonell, S., Flors, C., Eds.; *Royal Society of Chemistry*, **2016**;

(79) Cadet, J.; Ravanat, J.-L.; Martinez, G. R.; Medeiros, M. H. G.; Mascio, P. D. Singlet Oxygen Oxidation of Isolated and Cellular DNA: Product Formation and Mechanistic Insights. *Photochem. Photobiol.* **2006**, *82* (5), 1219–1225.

(80) Kaina, B. DNA Damage-Triggered Apoptosis: Critical Role of DNA Repair, Double-Strand Breaks, Cell Proliferation and Signaling. *Biochem. Pharmacol.* **2003**, *66* (8), 1547–1554.

(81) Hegde, M. L.; Hazra, T. K.; Mitra, S. Early Steps in the DNA Base Excision/Single-Strand Interruption Repair Pathway in Mammalian Cells. *Cell Res. 2008 181* **2008**, *18* (1), 27–47.

(82) Surjana, D.; Halliday, G. M.; Damian, D. L. Nicotinamide Enhances Repair of Ultraviolet Radiation-Induced DNA Damage in Human Keratinocytes and Ex Vivo Skin. *Carcinogenesis* **2013**, *34* (5), 1144–1149.

(83) Kusakabe, M.; Onishi, Y.; Tada, H.; Kurihara, F.; Kusao, K.; Furukawa, M.; Iwai, S.; Yokoi, M.; Sakai, W.; Sugasawa, K. Mechanism and Regulation of DNA Damage Recognition in Nucleotide Excision Repair. *Genes Environ.* **2019**, *41* (1), 1–6.

(84) Jiricny, J. The Multifaceted Mismatch-Repair System. *Nat. Rev. Mol. Cell Biol.* **2006**, *7* (5), 335–346.

(85) Sachadyn, P. Conservation and Diversity of MutS Proteins. *Mutat. Res. Mol. Mech. Mutagen.* **2010**, *694* (1–2), 20–30.

(86) Christmann, M.; Verbeek, B.; Roos, W. P.; Kaina, B. O6-Methylguanine-DNA Methyltransferase (MGMT) in Normal Tissues and Tumors: Enzyme Activity, Promoter Methylation and Immunohistochemistry. *Biochim. Biophys. Acta - Rev. Cancer* **2011**, *1816* (2), 179–190.

(87) Panier, S.; Boulton, S. J. Double-Strand Break Repair: 53BP1 Comes into Focus. *Nat. Rev. Mol. Cell Biol.* **2013**, *15* (1), 7–18.

(88) Rydberg, B.; Dosanjh, M. K.; Singer, B. Human Cells Contain Protein Specifically Binding to a Single 1,N6-

Ethenoadenine in a DNA Fragment. *Proc. Natl. Acad. Sci.* **1991**, *88* (15), 6839–6842.

(89) Singer, B.; Antoccia, A.; Basu, A. K.; Dosanjh, M. K.; Fraenkel-Conrat, H.; Gallagher, P. E.; Kusmierek, J. T.; Qiu, Z. H.; Rydberg, B. Both Purified Human 1,N6-Ethenoadenine-Binding Protein and Purified Human 3-Methyladenine-DNA Glycosylase Act on 1,N6-Ethenoadenine and 3-Methyladenine. *Proc. Natl. Acad. Sci.* **1992**, *89* (20), 9386–9390.

(90) Saparbaev, M.; Langouët, S.; Privezentzev, C. V.; Peter Guengerich, F.; Cai, H.; Elder, R. H.; Laval, J. 1,N 2-Ethenoguanine, a Mutagenic DNA Adduct, Is a Primary Substrate of Escherichia ColiMismatch-Specific Uracil-DNA Glycosylase and Human Alkylpurine-DNA-N-Glycosylase. *J. Biol. Chem.* **2002**, *277* (30), 26987–26993.

(91) Chaim, I. A.; Gardner, A.; Wu, J.; Iyama, T.; Wilson, D. M.; Samson, L. D. A Novel Role for Transcription-Coupled Nucleotide Excision Repair for the in Vivo Repair of 3,N4-Ethenocytosine. *Nucleic Acids Res.* **2017**, *45* (6), 3242–3252.

(92) Yi, C.; Jia, G.; Hou, G.; Dai, Q.; Zhang, W.; Zheng, G.; Jian, X.; Yang, C. G.; Cui, Q.; He, C. Iron-Catalysed Oxidation Intermediates Captured in a DNA Repair Dioxygenase. *Nature.* **2010**, *468* (7321), 330–333.

(93) Feng, C.; Liu, Y.; Wang, G.; Deng, Z.; Zhang, Q.; Wu, W.; Tong, Y.; Cheng, C.; Chen, Z. Crystal Structures of the Human RNA Demethylase Alkbh5 Reveal Basis for Substrate Recognition. *J. Biol. Chem.* **2014**, *289* (17), 11571–11583.

(94) Fedeles, B. I.; Singh, V.; Delaney, J. C.; Li, D.; Essigmann, J. M. The AlkB Family of Fe(II)/α-Ketoglutarate-Dependent Dioxygenases: Repairing Nucleic Acid Alkylation Damage and Beyond . *J. Biol. Chem.* **2015**, *290* (34), 20734–20742.

(95) Ringvoll, J.; Moen, M. N.; Nordstrand, L. M.; Meira, L. B.;

Pang, B.; Bekkelund, A.; Dedon, P. C.; Bjelland, S.; Samson, L. D.; Falnes, P.; Klungland, A. AlkB Homologue 2–Mediated Repair of Ethenoadenine Lesions in Mammalian DNA. *Cancer Res.* **2008**, *68* (11), 4142–4149.

(96) Kelner, A. Effect of Visible Light on the Recovery of Streptomyces Griseus Conidia from Ultra-Violet Irradiation Injury. *Proc. Natl. Acad. Sci. U. S. A.* **1949**, *35* (2), 73–79.

(97) Sancar, A. Structure and Function of DNA Photolyase and Cryptochrome Blue-Light Photoreceptors. *Chem. Rev.* **2003**, *103* (6), 2203–2237.

(98) Sancar, A. Structure and Function of Photolyase and in Vivo Enzymology: 50th Anniversary. *J. Biol. Chem.* **2008**, *283* (47), 32153–32157.

(99) Byrdin, M.; Hoang, N.; Ritz, T.; Chaves, I.; Pokorny, R.; Brettel, K.; Essen, L.-O.; Van Der Horst, G. T. J.; Batschauer, A.; Ahmad, M. The Cryptochromes: Blue Light Photoreceptors in Plants and Animals. *Artic. Annu. Rev. Plant Biol.* **2011**.

(100) Kim, S. T.; Sancar, A.; Essenmacher, C.; Babcock, G. T. Time-Resolved EPR Studies with DNA Photolyase: Excited-State FADH0 Abstracts an Electron from Trp-306 to Generate FADH-, the Catalytically Active Form of the Cofactor. *Proc. Natl. Acad. Sci.* **1993**, *90* (17), 8023–8027.

(101) Aubert, C.; Vos, M. H.; Mathis, P.; Eker, A. P. M.; Brettel, K. Intraprotein Radical Transfer during Photoactivation of DNA Photolyase. *Nature* **2000**, *405* (6786), 586–590.

(102) Yamamoto, J.; Plaza, P.; Brettel, K. Repair of (6-4) Lesions in DNA by (6-4) Photolyase: 20 Years of Quest for the Photoreaction Mechanism. *Photochem. Photobiol.* **2017**, *93* (1), 51–66.

(103) Espagne, A.; Burdin, M.; Eker, A. P. M.; Brettel, K. Very Fast Product Release and Catalytic Turnover of DNA Photolyase.

ChemBioChem **2009**, *10* (11), 1777–1780.

(104) Kim, S. T.; Malhotra, K.; Smith, C. A.; Taylor, J. S.; Sancar, A. Characterization of (6-4) Photoproduct DNA Photolyase. *J. Biol. Chem.* **1994**, *269* (11), 8535–8540.

(105) Maul, M. J.; Barends, T. R. M.; Glas, A. F.; Cryle, M. J.; Domratcheva, T.; Schneider, S.; Schlichting, I.; Carell, T. Crystal Structure and Mechanism of a DNA (6-4) Photolyase. *Angew. Chemie Int. Ed.* **2008**, *47* (52), 10076–10080.

(106) Li, J.; Liu, Z.; Tan, C.; Guo, X.; Wang, L.; Sancar, A.; Zhong, D. Dynamics and Mechanism of Repair of Ultraviolet-Induced (6–4) Photoproduct by Photolyase. *Nature.* **2010**, *466* (7308), 887–890.

(107) Sadeghian, K.; Bocola, M.; Merz, T.; Schütz, M. Theoretical Study on the Repair Mechanism of the (6-4) Photolesion by the (6-4) Photolyase. *J. Am. Chem. Soc.* **2010**, *132* (45), 16285–16295.

(108) Yamamoto, J.; Martin, R.; Iwai, S.; Plaza, P.; Brettel, K. Repair of the (6–4) Photoproduct by DNA Photolyase Requires Two Photons. *Angew. Chemie Int. Ed.* **2013**, *52* (29), 7432–7436.

CHAPTER 2

GENERAL OBJECTIVES

This Doctoral thesis is framed within the fields of photochemistry and photobiology. It focuses on the photobehavior and photorepair of etheno adducts. As mentioned in the introduction, these oxidatively generated DNA damages, are ubiquitous in our organism as a consequence of the interaction of DNA with subproducts of lipid peroxidation. On the one hand, these lesions exhibit an extended conjugation in respect with their canonical bases, which should modify their photochemical behavior and represent a threat for genome integrity. On the other hand, they display significant mutagenic properties, generating base transitions or transversions in mammal cells. Consequently, the development of new strategies for their repair is of great interest. In this context, the two main objectives of this Thesis are (i) to determine the photophysical properties of the etheno adducts and their role as potential intrinsic photosensitizers, and (ii) to design new strategies for their repair.

To achieve these goals, specific objectives have to be addressed during this Doctoral Thesis. They have been tackled over the three chapters:

1) To get a better understanding on the etheno adducts optical properties through the detailed study of εdC excited state relaxation processes using spectroscopic studies at femtosecond timescale combined with quantum chemistry calculations.

2) To establish the reactivity of etheno adducts toward singlet oxygen and one-electron photooxidants and investigate the role of these processes as photorepair pathways for the etheno lesions.

3) To synthesize a system based on plasmon-enhanced triplet excited state production using new hybrid metal nanoparticles decorated with Rose Bengal and investigate their application for the photorepair of etheno adducts.

CHAPTER 3

AN EXPERIMENTAL AND COMPUTATIONAL STUDY OF THE MUTAGENIC ETHENO ADDUCT 3,N4-ETHENO-2'-DEOXYCYTIDINE PHOTOPHYSICS.

3.1. INTRODUCTION

Over the years, stability of DNA upon UV irradiation and its connection with genetic preservation have been widely studied leading to the conclusion that the natural selection of the nucleobases is related to their high resistance to photochemical damage. [1–3] Indeed, both experimental and theoretical studies have demonstrated how the nucleobases efficiently dissipate the absorbed UV-radiation through ultrafast internal conversion channels, in this way reducing the photoreactions at the origin of lesion formation. [1–5]

However, small changes in the base structure can drastically modify its photochemical properties through the lengthening of its excited state lifetime and/or the increase of intersystem crossing efficiency, opening the door to a higher photoreactivity. In this respect, 5-methylcytosine, (6-4) photoproducts, 5-formylpyrimidine and thiobases are some of the DNA modifications that illustrate how minor changes interfere in the photophysical properties of the nucleobase and induce an increase of DNA photodamages becoming intrinsic DNA photosensitizers. [6–14]

In this context, etheno adducts are interesting candidates to evaluate the relationship between a modification of the structure and changes of the photochemical properties. A remarkable feature of some etheno derivatives is their inherent fluorescence emission. This way, the etheno-derived 2'-deoxyadenosine (εdA) has been used as a tool for monitoring enzymatic processes, or investigating changes in nucleic acid structure, such as nucleotide flipping, DNA binding, etc. [15–18]

Since the first time εdA was isolated by Leonard et al [19] its spectroscopic properties revealed that εdA presented a more extended π-conjugation, resulting in a red shift of its absorption spectrum and in a broad emission band in the UV-Vis compared with adenosine.

Therefore, etheno adducts attracted the attention of the scientific community and their properties began to be studied. In this context another etheno adduct started to show a particular interest due to its high mutation frequency, 81% in a single-stranded

vector replicated in mammals kidney cells, [20] namely the 3,N4-etheno-2'-deoxycytidine (εdC, Figure 3.1.).

In the case of εdC, fluorescence has only been observed in its protonated form with a very low quantum yield ($\phi_F < 0.01$) and a short lifetime of ca 30 ps, evaluated by means of an indirect method.[21] From the computational side, a few, scattered studies are available in the literature, focused mainly on the absorption and emission energies of εC and εCH^+.[22,23] So up to now the photophysical and theoretical studies reported for εdC are fragmentary leaving a lack in the understanding of its photolability since its presence in the DNA sequence can modify its inherent photorelaxation pathway. Thus, a complete picture of the ultrafast processes responsible for its deactivation is essential to evaluate its potential to delay the efficient DNA photodeactivation. This chapter is a full photochemical study of εdC not only from an experimental point of view but also on the theoretical calculations that help us to understand its photo-activated dynamics.

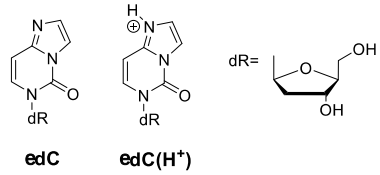

Figure 3.1. Structure of the studied etheno adduct in its neutral (εdC) and acid form ($\varepsilon dC(H^+)$).

3.2. RESULTS AND DISCUSSION

3.2.1. Experimental studies

3.2.1.1. Steady-state absorption and emission spectra

As a first step, absorption and fluorescence emission spectra were carried out in different aqueous buffer solutions, at neutral and acidic pH. In phosphate buffer saline solution (PBS, at pH 7.4), εdC exhibits an absorption band with a maximum at 273 nm that reaches the UVB region (Figure 3.2. and Table 3.1) with a shoulder at ca. 291 nm. Interestingly, the presence of the extra-ring does not induce

an important change as εdC absorption is only slightly red-shifted compared to the canonical 2´-deoxycytidine.[7]

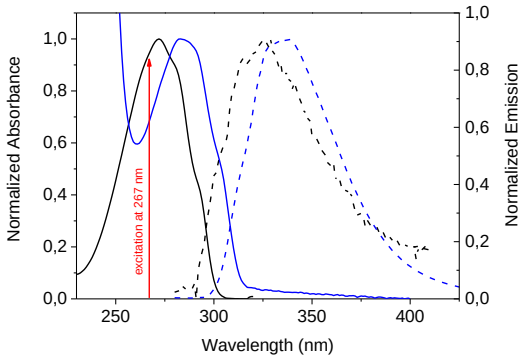

Figure 3.2. Absorption (solid line) and fluorescence emission (dash line) spectra of εdC in PBS 0.1M pH 7.4 (black color) and citric acid buffer at pH 3 (blue color), fluorescence steady-state spectra were obtained upon excitation at 267 nm.

Steady-state fluorescence was measured at room temperature under excitation at λ_{exc}= 267 nm. The emission spectrum exhibits a very broad signal that extends over from 290 to 400 nm with a maximum peaking in the UVA at λ_{em} of ca. 325 nm (Figure 3.2.). No dependence on the excitation wavelength was found between 266 to 290 nm (Figure 3.3). A fluorescence quantum yield (ϕ_F, Table 3.1.) of ca. 1.8×10^{-4} was determined using thymidine monophosphate as reference (ϕ_F=$1.5 \cdot 10^{-4}$) and an λ_{exc}= 255 nm.[24]

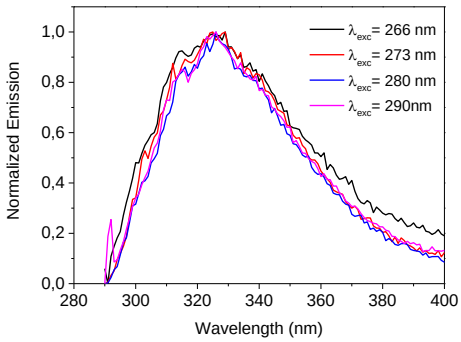

Figure 3.3. Steady-state fluorescence spectra of εdC in PBS 0.1M pH 7.4 obtained at different excitation wavelengths.

Table 3.1. Optical properties of εdC and dC in aqueous solution at pH 7.4 and 3, absorption maximum (λ_{max}) and its corresponding extinction coefficient (ε_{max}), steady-state emission fluorescence maximum (λ_{em}) and fluorescence quantum yield (ϕ_F) determined at λ_{exc}= 267 nm.

	λ_{max}	λ_{em}	ϕ_F	ε ($M^{-1}cm^{-1}$)
εdC (pH 7.4)	273 nm (4.54 eV)	325 nm (3.81 eV)	$1.84 \cdot 10^{-4}$	13200
εdCH$^+$ (pH 3)	284 nm (4.36 eV)	332 nm (3.7 eV)	$2.76 \cdot 10^{-3}$	7200
dC[a]	271 nm	323 nm	$0.6 \cdot 10^{-4}$	9300

[a] in water, data from ref [7]

The effect of protonation on the singlet excited state properties was considered by performing the experiments at pH 3, using citric acid buffer. Under these conditions the nitrogen N4 of the cytidine etheno derivative is protonated (εdCH$^+$, Figure 3.1). When decreasing the pH, a bathochromic shift from λ_{max} = 273 nm to 284 nm was observed for the absorption band. This change was accompanied by a decrease of the molar absorption coefficient ε_{max} (Figure 3.2 and Table 3.1). A shoulder in the UVB region is also present at ca. 303 nm. Likewise, steady-state fluorescence spectrum suffers a red-shift with an emission band centred at 332 nm (Figure 3.2). And the fluorescence quantum yield increased by one order of magnitude, being ϕ_F of ca. 2.7×10^{-3} (Table 3.1), when compared to εdC's quantum yield.

By contrast, only small changes have been detected in the emission spectra recorded in solvents of different polarity, with only a few nanometers blue shift observed when moving from PBS to diethyl ether (Table 3.2., Figure 3.4). The fluorescence quantum yields remain in the order of 10^{-4} varying from 1.8×10^{-4} in PBS to 2.9×10^{-4} in acetonitrile (Table 3.2).

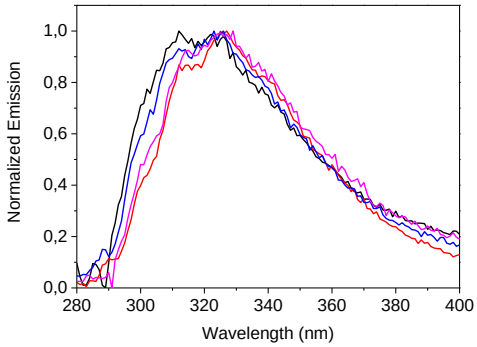

Figure 3.4. Fluorescence emission spectra obtained upon excitation of εdC at 266 nm in different solvents: acetonitrile (black), methanol (red), diethyl ether (blue) and PBS (fuchsia).

Table 3.2. εdC spectroscopic properties depending on the polarity of solvents, determined upon excitation at 266 nm. The reference compound, TMP, was excited at 255 nm.

	polarity	λ_{max} ***(nm)***	λ_{em} ***(nm)***	ϕ_F
PBS	10.2	273	325	$1.8 \cdot 10^{-4}$
MeCN	5.8	273	322	$2.9 \cdot 10^{-4}$
MeOH	5.1	273	320	$2.0 \cdot 10^{-4}$
Et_2O	2.8	273	318	$2.1 \cdot 10^{-4}$

3.2.1.2. Time resolved upconversion fluorescence experiments

In view of the very low fluorescence quantum yields, the excited state lifetimes are expected to be very short. Therefore, femtosecond fluorescence upconversion experiments were performed in order to resolve the time-dependence of the emission.

The excitation wavelength used ie. 267 nm leads to a population of both S_1 (**ππ*1**) and S_2 (**ππ*2**), with consequences discussed below.

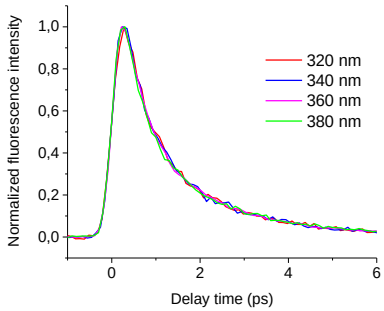

Figure 3.5. Total fluorescence decays obtained from a solution of εdC in PBS pH 7.4 at different emission wavelengths after excitation at λ_{exc}= 267 nm.

For the εdC solution at neutral pH, the decays were recorded from 310 to 420 nm. As shown in Figure 3.5. only small variations were observed for different emission wavelengths. These decays cannot be described in a satisfactory way by a monoexponential function; by contrast biexponential function reproduces the data more adequately (Table 3.3 and 3.4). Thus, decays were analyzed following a nonlinear fitting/deconvolution procedure using the biexponential function: $f(t) = a_1 \exp(-t/\tau_1) + a_2 \exp(-t/\tau_2)$ with $a_2 = 1-a_1$.

Table 3.3. Fitted parameters for the decays of εdC in PBS.

	310 nm	***320 nm***	***340 nm***	***360 nm***
$\mathbf{a_1}$	0.585 ± 0.017	0.592 ± 0.010	0.568 ± 0.031	0.658 ± 0.017
$\boldsymbol{\tau_1}$ (ps)	0.260 ± 0.032	0.395 ±0.0198	0.479 ± 0.044	0.547 ± 0.021
$\mathbf{p_1}^a$	0.178 ± 0.021	0.237 ± 0.012	0.260 ± 0.032	0.341 ± 0.020
$\mathbf{a_2}$	0.415 ± 0.017	0.408 ± 0.010	0.431 ± 0.031	0.342 ± 0.017
$\boldsymbol{\tau_2}$ (ps)	1.686 ± 0.051	1.849 ± 0.037	1.796 ± 0.084	2.029 ± 0.062
$\mathbf{p_2}^a$	0.822 ± 0.021	0.763 ± 0.012	0.740 ± 0.032	0.659 ± 0.020
$\boldsymbol{<\tau>}$ (ps)^b	0.852 ± 0.037	0.988 ± 0.024	1.048 ± 0.060	1.054 ± 0.036
$\mathbf{r_0}$	0.296 ± 0.005	0.285 ± 0.002	0.273 ± 0.004	0.261 ± 0.002
$\boldsymbol{\tau_R}$ (ps)^c	55	55	55	55

[a] relative contributions p_1 and p_2 have been calculated as follows: $p_1 = a_1\tau_1/(a_1\tau_1+a_2\tau_2)$ and $p_2 = a_2\tau_2/(a_1\tau_1+a_2\tau_2)$, [b] The average lifetime was calculated as $<\tau> = a_1\tau_1 + a_2\tau_2$, [c] fixed value.

The lifetime of the fast component increases monotonously by a factor two with wavelength, from 0.26 ps at 310 nm to 0.54 ps at 420 nm. The amplitude (a_1) of this component increases very slightly with wavelength, from 0.59 at 310 nm to 0.62 at 420 nm. The lifetime of the longer component also increases monotonously with wavelength, from 1.68 ps at 310 nm to 2.38 ps at 420 nm, whereas its amplitude (a_2) decreases within the same range from 0.42 to 0.38 (Table 3.3.). The average lifetime $<\tau>$ is practically constant, about 1 ps, between 320 and 380 nm.

The zero-time fluorescence anisotropy (r_0) is of ca. 0.28-0.29 (Table 3.3.) and does not show any significant dependence on the registered emission. This value is, however, significantly lower than the expected value of 0.4 for parallel absorption and emission transition dipoles and may indicate an ultrafast change of the nature of the excited state.

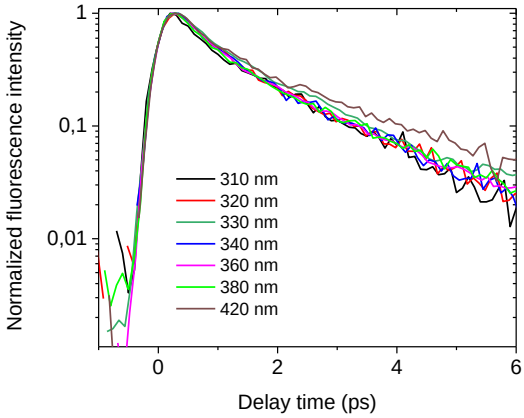

Figure 3.6. Fluorescence decays obtained from a solution of εdC in PBS pH 7.4 at different emission wavelengths after excitation at λ_{exc}= 267 nm.

Focusing on longer wavelengths the two traces at λ=380 and 420 nm (Figure 3.6.) were fitted with a bi-exponential function, keeping the longer time fixed to 55 ps (Table 3.4.). These anisotropies decay rapidly during the first picosecond (Table 3.4., $\tau_{R,1}$ of ca. 0.4 ps), which can indicate a further "slower" electronic relaxation at longer wavelengths. Interestingly, the fluorescence

decays of εdC in aqueous solution are longer than those of the "canonical" nucleoside dC, for which a τ_1 of ca. 0.22 and a τ_2 of ca. 0.96 ps (average lifetime $<\tau> \approx 0.4$ ps) were reported in the literature.[7]

Table 3.4. Fitted parameters for the decays of εdC in PBS. The average lifetime was calculated as $<\tau> = a_1\tau_1 + a_2\tau_2$. The anisotropy decay time $\tau_{R,2}$ was fixed to 55 ps.

	380 nm	***420 nm***
$\mathbf{a_1}$	0.642 ± 0.017	0.618 ± 0.028
$\boldsymbol{\tau_1}$ (ps)	0.512 ± 0.023	0.537 ± 0.046
$\mathbf{p_1}^a$	0.313 ± 0.020	0.268 ± 0.031
$\mathbf{a_2}$	0.358 ± 0.017	0.382 ± 0.028
$\boldsymbol{\tau_2}$ (ps)	2.011 ± 0.061	2.378 ± 0.130
$\mathbf{p_2}^a$	0.687 ± 0.020	0.732 ±0.031
$\boldsymbol{<\tau>}$(ps)	1.049 ± 0.036	1.240 ± 0.077
$\mathbf{r_0}$	0.270 ± 0.007	0.275 ± 0.014
$\mathbf{a_r}$	0.178 ± 0.025	0.626 ± 0.031
$\boldsymbol{\tau_{R,1}}$ (ps)	0.437 ± 0.198	0.348 ± 0.076
$\boldsymbol{\tau_{R,2}}$ (ps)	55	55

[a] relative contributions p_1 and p_2 have been calculated as follows: $p_1 = a_1\tau_1/(a_1\tau_1+a_2\tau_2)$ and $p_2 = a_2\tau_2/(a_1\tau_1+a_2\tau_2)$

Although the increase of the lifetime between the "canonical" base and its etheno analogue is not so large, it might represent a significant obstacle to the efficient DNA excited state decay pathway. To some extent this could be connected to the "Trojan horse" concept proposing that certain damages can act as intrinsic DNA photoactive species.[9–14,25]

Nonetheless, for damages such as (6-4) photoproducts or formylpyrimidine derivatives, both experimental and theoretical studies have highlighted the involvement of a triplet manifold with a lifetime in the μs timescale. [9–14,25] In the εdC case, no triplet excited state has been detected, which leaves the singlet excited state as the only potential reactive state.

In addition, time-resolved fluorescence spectra were recorded with the upconversion set-up (Figure 3.7.). It shows how the intense band centered at 330 nm decays rapidly on a time scale of few ps. Furthermore, the obtained spectra fit well with the steady-state spectrum described above, which means that the fluorescence emission does not contain any important long-lived component having different maximum and/or shape than that detected with the upconversion setup.

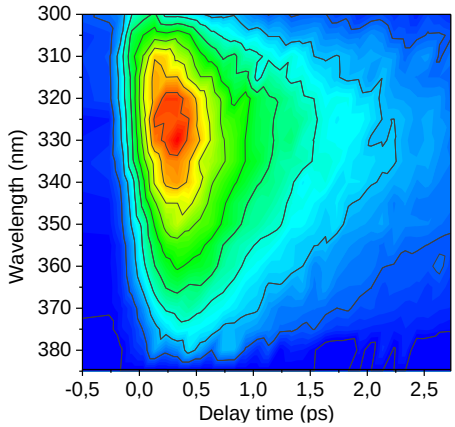

Figure 3.7. Corrected time-resolved fluorescence spectra of εdC in PBS at pH 7.4 after laser excitation at λ_{exc}= 267 nm.

The time-resolved fluorescence spectra showed that the total intensity decays rapidly with a time constant of about 1 ps (Figure 3.8. (A)), in accordance with the individual decays (average lifetime $<\tau>$, Table 3.3.) reported above.

The fluorescence spectrum undergoes an ultrafast red shift followed by a small amplitude and much slower blue shift stabilizing at 30400 cm^{-1} (Figure 3.8. (B)). The former might correspond to water solvation dynamics occurring at sub-ps to ps timescale,[26,27] whereas the latter might be interpreted in terms of rearrangement of the sugar conformation as previously proposed for guanosine derivatives. [27]

A ~ 10% decrease of the spectral width (Figure 3.8. (C)) occurring within 3 ps, may correspond to the common signature of a vibrational cooling.[28] It is proposed that the strong hydrogen

bonding of the nucleoside to water molecules allows an efficient intermolecular vibrational energy transfer to the solvent.[28]

This conclusion was based on previous works suggesting a solute and solvent-dependent of intermolecular energy transfer (dissipation) from the electronically excited organic molecules to their surroundings.[29–31] Later, the role of hydrogen bonding in accelerating the cooling was definitively evidenced by studies comparing the kinetics of azulene in different nonaqueous media and in aqueous methanol.[32,33]

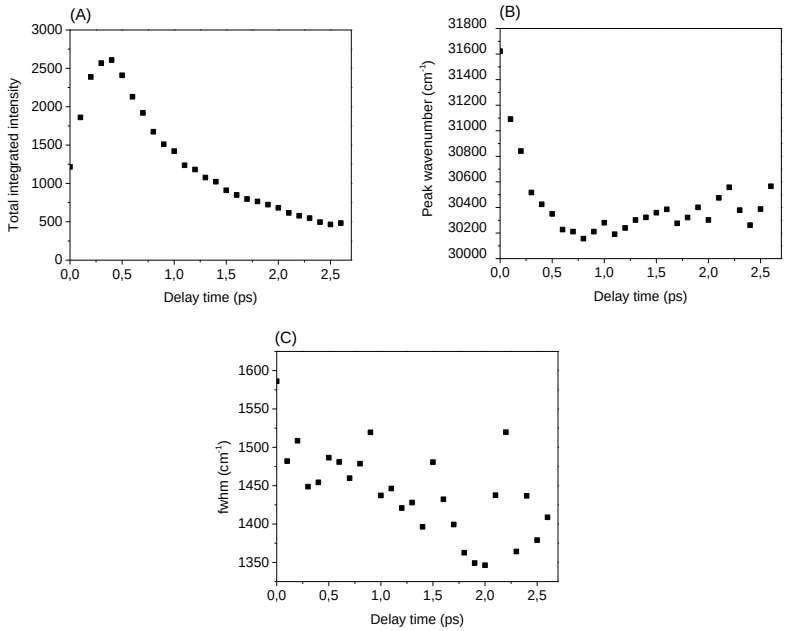

Figure 3.8. Time evolution of (A) total intensity, (B) peak frequency and (C) spectral width using log-normal functions.

Similar experiments were run using citric acid buffer at pH 3 to get more information on the singlet excited state dynamics of the protonated εdCH$^+$.

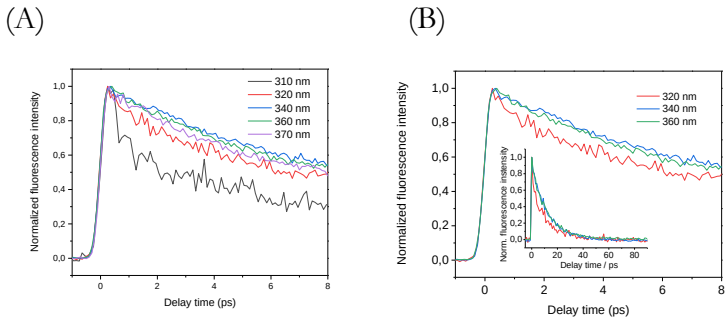

Figure 3.9. Total fluorescence decays obtained for a solution of εdCH$^+$ in citric acid: (A) emission wavelengths from 310 to 370 nm and (B) emission wavelengths close to its emission maximum after excitation at λ_{exc}= 267 nm.

The decays were registered upon excitation at 267 nm, as in the case of pH 7.4 for emission wavelengths from 310 to 370 nm (Figures 3.9A).

Overall, the decays are much slower at pH 3 than at pH 7.4. The decays at the blue and red edges, ie. 310, 320 and 370 nm, are faster than those registered next to the maximum of emission 340 and 360 nm, which are similar. However, in all cases, a biexponential function is needed for an optimized fitting of the data and lifetimes (Table 3.5.). Actually at 340 nm which is close to εdCH$^+$ emission maximum, the fast component (τ_1 of ca. 0.123 +/- 0.074 ps) has a very weak contribution (relative weight: p_1= 0.00143 +/- 0.00141) compared to the longer lived one (τ_2 of ca. 12.72 +/- 0.11 ps and p_2=0.99857 +/- 0.00141). Therefore, the decay can be considered as nearly mono-exponential with a mean lifetime $<\tau>$ of ca. 11.1 +/- 1.1 ps, which is in the same order of magnitude than that extrapolated from earlier fluorescence data (τ of ca. 30 ps). [21]

The anisotropy decay is mono-exponential, with a zero-time anisotropy (r_0) of ca. 0.32 +/- 0.002 and a lifetime of τ_R = 55 +/- 5 ps. To understand the origin of the faster time-constant τ_1 it will be needed theoretical calculation support.

Table 3.5. Fitted parameters for the decays of εdCH$^+$ at pH 3.

	320 nm	*340 nm*	*360 nm*
a_1	0.212 ± 0.012	0.128 ± 0.088	0.137 ± 0.011
τ_1 (ps)	0.672 ± 0.083	0.123 ± 0.074	1.68 ± 0.23
p_1	0.014 ± 0.002	0.0014 ± 0.0014	0.018 ± 0.003
a_2	0.788 ± 0.012	0.872 ± 0.088	0.863 ± 0.011
τ_2 (ps)	12.59 ± 0.26	12.72 ± 0.11	14.25 ±- 0.35
p_2	0.986 ± 0.002	0.999 ± 0.001	0.982 ± 0003
$\langle\tau\rangle$ (ps)	10.06 ± 0.25	11.1 ± 1.1	12.54 ± 0.33
r_0	0.327 ± 0.004	0.320 ± 0.002	0.317 ± 0.003
τ_R (ps)	49 ± 7	55 ± 5	46 ± 4

Finally, the time-resolved fluorescence spectra were recorded after excitation at 267 nm (Figure 3.10.). The observed emission at long times (> 20 ps) with a maximum λ_{em} of ca. 330 nm is in concordance with the steady-state spectrum shown in Figure 3.3. However, contrary to the case of pH 7, the intense band centered at 330 nm decays more slowly on a time scale of >10 ps. For this reason, the time-resolved spectra were recorded in two time-windows, 3 and 30 ps, with adequately chosen time-steps.

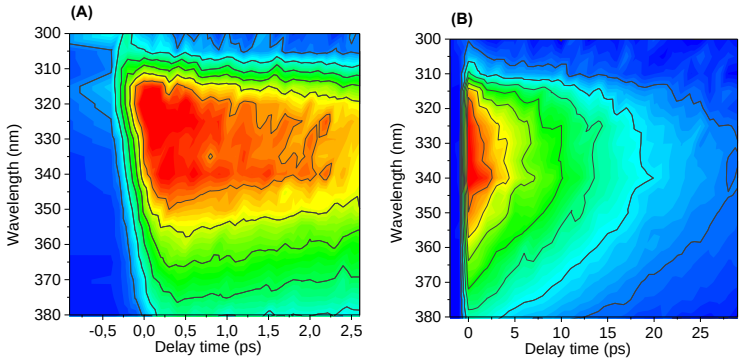

Figure 3.10. Time-resolved fluorescence spectra of εdCH$^+$ in citrate buffer at pH 3 over a time window of (A) 3 ps and (B) 30 ps. The excitation wavelength was λ_{exc}= 267 nm and the average power was 50 mW. The intensity scaling of the two figures are not the same, explaining the apparent differences.

A deeper analysis of the time-resolved spectra at pH 3 using log-normal functions was performed for the two time-windows of 3 and 30 ps (Figure 3.11. left and right, respectively).

As in the case of pH 7.4, an ultrafast red shift, more or less limited by the 400 fs irf, can be observed (Figures 3.11.B); then, beyond 1 ps, this shift proceeds more slowly all the spectra up to 30 ps.

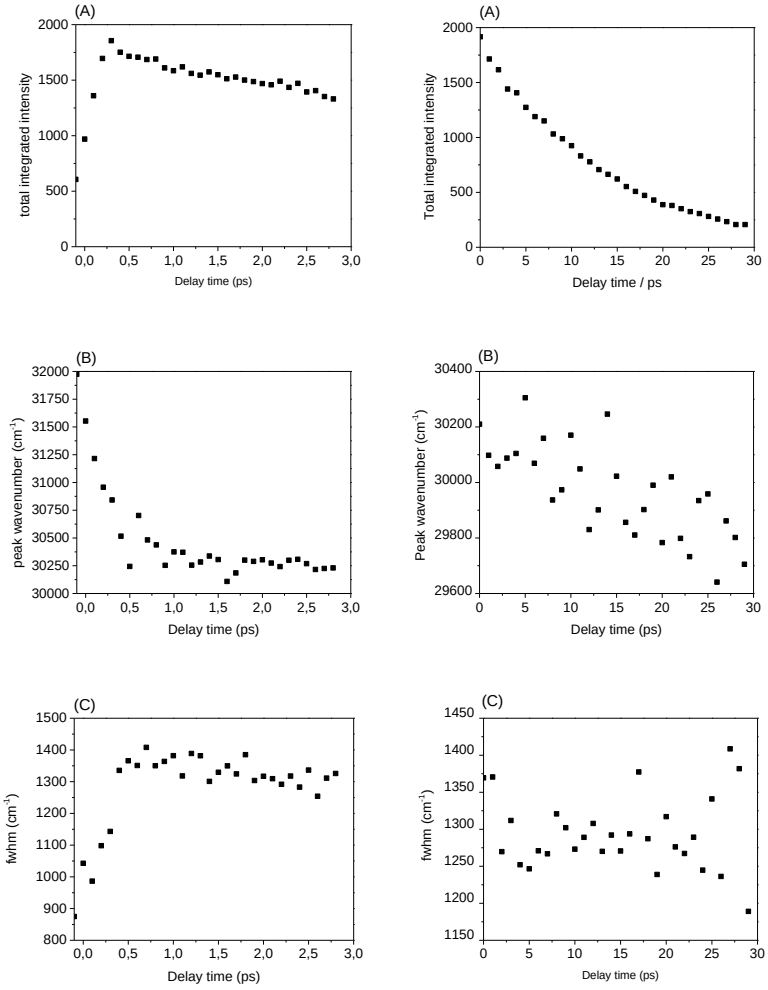

Figure 3.11. Time evolution of (A) total intensity, (B) peak frequency and (C) spectral width using log-normal functions at a time window of 3 ps (left) and 30 ps (right).

Regarding the spectral width, an ultrafast broadening appears, once again limited by the 400 fs irf (Figure 3.11.(C) left), followed by a ps narrowing from ≈1350 cm^{-1} to ≈1300 cm^{-1}, which could be due to cooling. At longer times, there is no visible change in the spectral width (Figure 3.11.(C) right).

3.2.2. Theoretical calculations

3.2.2.1. Computed absorption and emission energies

The natural transition orbitals (NTO)[34] associated to the $S_0 \rightarrow S_1$ and $S_0 \rightarrow S_2$ electronic transitions for $\varepsilon C \cdot 2H_2O$ and $\varepsilon CH^+ \cdot 2H_2O$ (Figure 3.12.) are reported in Figure 3.13.

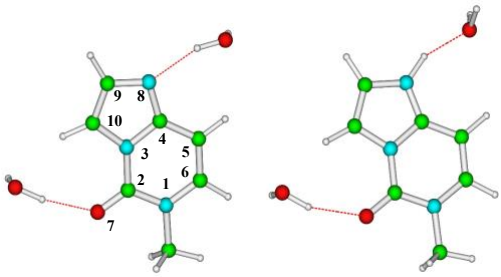

Figure 3.12. Computational model adopted to study εC in water solution at neutral $\varepsilon C \cdot 2H_2O$ on the left and its acidic form $\varepsilon CH^+ \cdot 2H_2O$ on the right.

NTOs is a useful tool to describe the electronic transitions in terms of one-particle excitations. In the case of εC the lowest energy excited state in the Franck Condon region (FC) (S_1) can be described as bright ππ* excitation (with a prevalent HOMO→LUMO contribution), called ππ*1, from an orbital with strong C5-C6 bonding character to an orbital which is antibonding with respect to this bond.

Besides, there is a strong contribution of the 5-member ring atoms to this excitation. The second lowest energy state S_2 is also a bright ππ* state (hereafter denoted as ππ*2), with the strongest contribution coming from HOMO→LUMO+1 excitation. This

picture is rather similar to that obtained for 1-methylcytosine (hereafter simply C) in water.

On the other hand, as shown in Table 3.6, significant differences are found with respect to the canonical nucleobase. In addition to a weak red-shift of the lowest energy absorption band, we observe that ππ*2 gets closer to ππ*1, while its intensity decreases.

On these grounds, the shift of the absorption maxima from 271 (in case of C) to 273 nm (in εC) is due to a very small red-shift of the lowest absorption band maximum with an increase in intensity of ππ*2 band. Overall, these changes lead to a blue-shift of the 'total' absorption band and the disappearance of the large shoulder at 250 nm present in the experimental spectrum of C.

Table 3.6. Vertical absorption and emission energies computed for εC•2H_2O and εC in water. PCM/M052X/6-31G(d) geometry optimization. Oscillator strength is given in parentheses. The results have been obtained at the solvent non equilibrium level.

	εC ·2H_2O		***εC***		***C***	
	6-31G (d)	***6-311+G (2d,2p)***	***6-31G (d)***	***6-311+G (2d,2p)***	***6-31G (d)***	***6-311+G (2d,2p)***
S_1 (ππ*1)	5.16 (0.29)	4.99 (0.31)	5.15 (0.30)	4.98 (0.32)	5.29 (0.17)	5.13 (0.25)
S_1 (ππ*1-min)$_{em}$	4.34 (0.35)		4.34 (0.35)			
S_1 (ππ*1-min)$_{em}$ [a]	4.17 (0.49)[a]	-	4.16 (0.49)[a]	-	-	-
S_2 (ππ*2)	5.52 (0.11)	5.30 (0.13)	5.56 (0.10)	5.34 (0.12)	6.27 (0.22)[b]	6.06 (0.17)
S_3 (nπ*)	6.42 (0.00)	6.26 (0.04)	6.26 (0.00)	6.17 (0.04)	5.84 (0.00)	5.87 (0.00)

[a] emission energies computed at the solvent equilibrium level, [b]S_4

The increase of the molar absorption coefficient with respect to C is also reproduced by our calculations. The dark excited states are affected, since the lowest energy nπ* state of C, involving the lone pair (LP) of N3, disappears. The lowest energy dark state (S_3), hereafter labelled as nπ*, therefore mainly corresponds to an

excitation from the carbonyl lone pair towards a π* orbital (similar to the LUMO+1) and, as for C in water, is less stable than ππ*2.

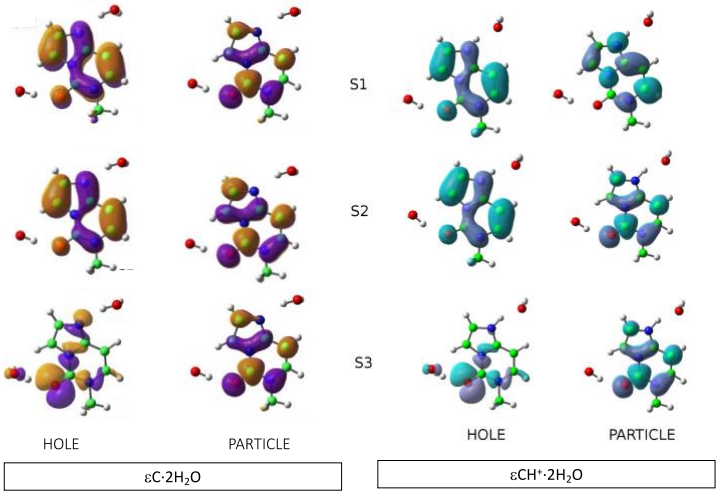

Figure 3.13. Natural Transition Orbital (NTO) associated to the three lowest energy excited states in εC·2H_2O (left) and $\varepsilon CH^+ \cdot 2H_2O$ (right) in water, according to PCM/M052X/6-31G(d) calculations. Upper row: particles. Lower row: hole.

Our calculations also capture the effect of protonation occurring in acidic pH (Table 3.7.). A red-shift of the lowest energy band by 0.2 eV is predicted, in good agreement with the experimental indications (λ_{max} 284 vs. 273 nm, Table 3.1 and Figure 3.2). The shape of the three lowest energy excited states is similar to that just described for the neutral compound (Figure 3.13. right), except for the loss of the contribution of the N8 lone pair to nπ*, which, though always 0.5 eV less stable than ππ*2, gets closer in energy to the bright excited states. It is worth noting that the explicit inclusion of H_2O molecules has a limited impact on the absorption spectra.

Finally, the extension of the basis set leads to a moderate red-shift of the spectra of both εC and εCH^+, but does not change the qualitative picture obtained with the smaller 6-31G(d) basis set. From a quantitative point of view, the computed vertical absorption energies are blue-shifted with respect to the experimental bands, confirming the trends evidenced for C. In addition to the possible limitations of the computational methods adopted, a significant part

of this discrepancy is due to the absence of vibrational and thermal effects in our calculations, which are expected to red-shift the computed band maxima by an additional 0.2 eV.[35]

S_1 geometry optimization leads to a stable minimum of the Potential Energy Surface (PES), denoted ππ*1-min, both for εC·2H_2O and $\varepsilon CH^+ \cdot 2H_2O$. The vertical emission energies obtained from these minima are given in Tables 3.6 y 3.7. Calculations duly reproduced the spectral red-shifts associated with protonation, being more important for absorption than for fluorescence. This is also well reflected, both experimentally and theoretically, by a higher Stokes (ν) shift under neutral (ν_{exp}=0.73 eV vs ν_{theo}=1 eV) conditions than at acidic pH (ν_{exp}=0.63 eV vs ν_{theo}=0.8 eV). The small overestimation of ν_{theo} can be interpreted in terms of vibronic effects which affect absorption and emission maxima in opposite directions.

Table 3.7. Vertical absorption and emission energies computed for $\varepsilon CH^+ \bullet 2H_2O$ and εCH^+ in water. PCM/M052X/6-31G(d) calculations. Oscillator strength is given in parentheses. The results have been obtained at the solvent non equilibrium level.

	εCH⁺ ·2H₂O		***εCH⁺***	
	6-31G (d)	***6-311+G (2d,2p)***	***6-31G (d)***	***6-311+G (2d,2p)***
S_1 (ππ*1)	4.95 (0.33)	4.84 (0.34)	4.88 (0.34)	4.78 (0.35)
S_1 $(\pi\pi^*1\text{-min})_{em}$	4.27 (0.36)	-	4.24 (0.36)	-
S_1 $(\pi\pi^*1\text{-min})_{em}$[a]	4.11 (0.49)[a]		4.07 (0.48)[a]	
S_2 **(ππ*2)**	5.82 (0.15)	5.59 (0.17)	5.93 (0.14)	5.68 (0.17)
S_3 **(nπ*)**	6.33 (0.00)	6.39 (0.00)	6.19 (0.00)	6.25 (0.00)

[a]emission energies computed at the solvent equilibrium level

Moreover, a more careful treatment of dynamical solvation effects could provide refined, and more reliable, values. The main

structural changes with respect to the Franck Condon point involve the lengthening of the C5-C6 and C9-C10 (Figure 3.12) double bonds. Interestingly the S_1 minimum keeps the planarity typical of the S_0 minimum, at difference with what happens for C, where a shallow minimum, with the ring adopting a strongly bent structure, is predicted.[4,7]

Geometry optimization of S_2 ($\pi\pi^*2$) for $\varepsilon C \cdot 2H_2O$ predicts a very effective decay to the underlying $\pi\pi^*1$ state, eventually reaching $\pi\pi^*1$-min. Optimizing $\pi\pi^*2$ for $\varepsilon CH^+ \cdot 2H_2O$, we obtain the same final outcome. However, analysis of the PES shows that a low-energy gradient region is present, we can consider as a pseudo-minimum for $\pi\pi^*2$.

Gas phase CASPT2 calculations (Figure 3.14 and Table 3.8) are consistent with the picture provided by TD-M052X, predicting that protonation red-shifts the lowest energy excited state by ~0.3 eV. Moreover, a planar minimum is predicted for S_1, a bright $\pi\pi^*$ HOMO→LUMO transition, with a predicted Stokes shift of ~1 eV.

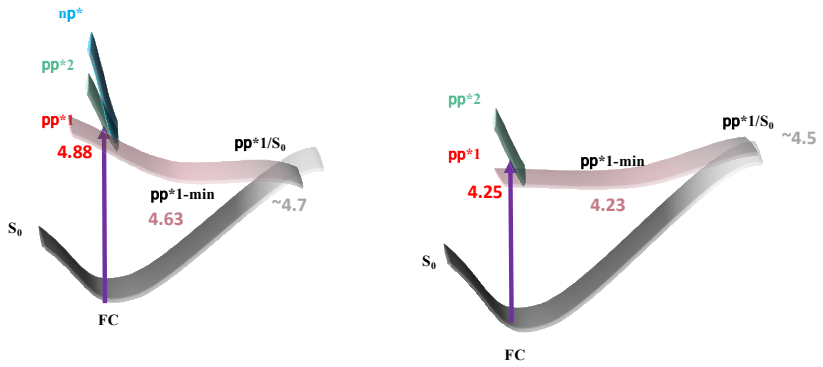

Figure 3.14. Schematic description of the proposed decay mechanism for εdC (left) and εdCH^+ (right) in gas phase according to CASPT2/CASSCF calculations.

Table 3.8. Vertical absorption and emission energies (in eV) computed for εC and εCH^+ in the gas phase. SS (italics) and MS-CASPT2 calculations. Oscillator strength is given in parentheses.

	εCH	***εCH⁺***
S_1 (ππ*1)	4.56(0.16) *4.88*	4.25(0.30) *4.25*
S_1 (ππ*1-min)	3.52(0.43) *4.17*	3.23(0.18) *3.49*
S_2 (ππ*2)	5.42(0.01)	5.73(0.02)
S_3 (nπ*1)	5.92(0.01)	6.13(0.00)
S_4 (nπ*1)	6.28(0.00)	6.24(0.00)

3.2.2.2. Deactivation pathways

In order to help the interpretation of the time-resolved experiments the main non-radiative decay paths for εC and εCH^+ have been mapped at PCM/TD-M052X/6-31G(d) level (Figure 3.15). As a first start calculations to obtain the S_1/S_0 crossing regions were done. This crossing regions can modulate the ground state recovery. The analysis was performed for ππ*1, since the geometry optimizations strongly suggest that ππ*2 decays effectively to ππ*1.

It has been mentioned that excitation at 267 nm leads to partial population of ππ*2. Therefore, the low value of the anisotropy at time zero show in the time resolved fluorescence experiment is affected by the population excited on ππ*2 and emitting from ππ*1. This process should be more relevant for εC than for its protonated counterpart, for which a larger ππ*2/ππ*1 energy gap is found in the FC point, in line with the experimental trends (r_0 = 0.27 for εC compared to 0.32 for εCH^+, Tables 3.3 and 3.5). No clear wavelength dependence is observed, in line with the emission coming only from ππ*1.

An extensive exploration of the PES allows locating a crossing region between $\pi\pi^*1$ and S_0 for both εC and εCH^+ at the PCM/TD-M052X/6-31G(d) level (Figure 3.15). The main geometrical features of this region are very similar to that exhibited by the Conical Intersection (CI) located at the CASPT2 level and discussed below. It is the C5-C6 ethylenic CI (Figure 3.16), a common feature of the decay path of pyrimidines nucleobases, with the C5 and the C6 atom out of the molecular plane and the H5 atom undergoing a significant out-of-plane motion. This crossing region is more stable than the S_1 minimum, but a sizeable energy barrier is present on the path. According to calculations this barrier is ~0.5 eV for εCH^+ and ~0.3 eV for εC.

In addition, a possible explanation to the faster time-constant τ_1 determined for εCH^+, which varies randomly as a function of the emission wavelength, is that during the motion away from the FC region toward, emission taking place at different energies are more sensitive to the different regions of the PES. Indeed, previous data obtained for 2'-deoxycytidine and its derivatives,[7,36] reported that this ultrafast lifetime in the blue side of the spectrum could be attributed to an emission from an area close to the FC region, or to the interplay with additional bright states.

In order to put this analysis on a firmer ground, CASPT2 was used to obtain a consistent picture describing the crossing regions with S_0 in the gas phase. A CI between $\pi\pi^*1$ and S_0, which is confirmed a C5-C6 ethylenic CI. This stationary point is higher in energy compared to $\pi\pi^*1$-min and the energy gap is ~0.1 for εC and 0.3 eV for εCH^+, respectively.

Moreover, any additional barrier along the $\pi\pi^*1$-min$\rightarrow S_1/S_0$ CI pathway was found after connecting $\pi\pi^*1$-min and the CI by minimum energy path calculations.

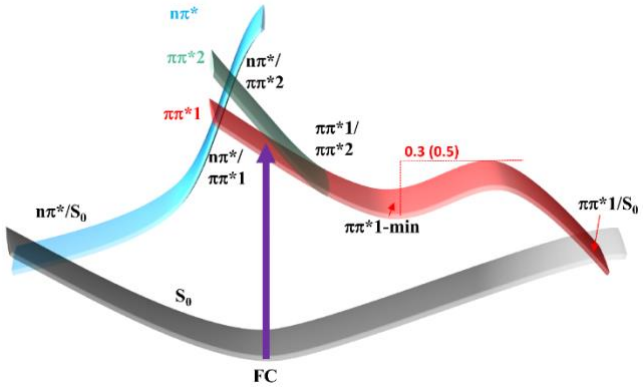

Figure 3.15. Schematic description of the proposed decay mechanism for εC and εCH^+ in water. The value in parentheses is relative to εCH^+.

Finally, geometry optimization of S_3 (nπ*) indicates that, after crossing of S_2 and S_3, a crossing region with S_0 is directly reached, without overcoming any energy barrier, both for εC and εCH^+. In the crossing region, the C2-O7 group undergoes a strong out-of-plane motion (Figure 3.16).

For both εC and for εCH^+ there is a viable path connecting the photoexcited population to a CI with S_0, which is more stable than ππ*1 at the FC point. However, this decay channel is expected to be less effective than that mapped for C. A sizeable energy barrier is indeed predicted by PCM/TD-M052X in water, whereas in the gas phase the CI is less stable than ππ*1-min, giving account of the longer lifetime found for εC with respect to C. In the case of protonation, it makes this non-radiative decay path more difficult (both according TD-M052X and CASPT2), in line with the experimental indications. These results are fully consistent with the longer lifetime (ca. 3 times) observed for the εC by respect with that of cytidine, and also with the increase of the lifetime under acidic conditions. It is noteworthy that another deactivation route was previously computed for C. This decay, which corresponds to a conical intersection with a new conformational deformation involving C4–NH_2 out of plane "sofa" type configuration, is somewhat more energetic than the ethylene-like CI.[37]

The barriers in the presence of the solvent were found to be 0.23 eV and 0.31 eV for the two different pathways compared to 0.15 eV and 0.14 eV in the gas phase, indicating that the aqueous

environment does not make one of the two directions much more preferable.

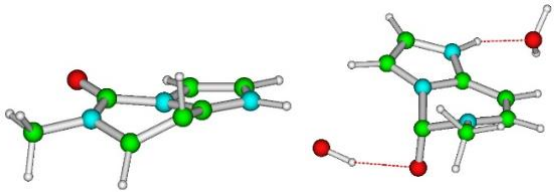

Figure 3.16. Schematic drawing of a representative structure of the (left) S_1/S_0 crossing region εCH^+ (right) S_3/S_0 crossing region for $\varepsilon CH^+ \bullet 2H_2O$. PCM/M052X/6-31G(d) calculations.

This "sofa" type pathway would be effectively blocked in εC, indicating that it does not represent any major relaxation channel since the excited state lifetime is still picosecond. Other studies addressed the importance of the ethylene-like CI by means of combined experimental/theoretical investigation of 5,6-trimethylenecytosine (TMC), where the C5 and C6 atoms are linked by an aliphatic (non-aromatic) chain.[38–40] This conformation constraint causes a strong energy barrier for the out-of-plane deformation at the C5 position.

Interestingly, this compound does not exhibit the subpicosecond excited-state lifetime characteristic for the naturally occurring pyrimidine bases. Instead, the fluorescence lifetime increases 4 to 10-times by respect with that of the unclamped nucleobase, showing the enormous involvement of the ethylene-like torsion in the non-radiative deactivation of the cytosine excited state. The picosecond range lifetime obtained for εdC together with the computational data disclose that the C5-C6 twist involved in the ethylene-like CI is not blocked by the presence of the etheno ring and still acts as the main radiationless pathway.

Another effective non-radiative decay path involves the dark state $S_3(n\pi^*)$. This excited state is less stable than the bright spectroscopic states in the FC region. On the contrary, despite being significantly less stable than the lowest energy bright states in water, it has been proposed to be involved in the excited state dynamics of C in aqueous solution,[6,7] and recent quantum dynamical simulations

in the gas phase have confirmed its strong coupling with the spectroscopic states.[41]

Actually, εCH^+ is rather close in energy to $\pi\pi^*2$ and, therefore, its involvement cannot be discarded. Interestingly, at difference with what happens for C, no minimum is provided for this dark state, whereas a barrierless path is predicted to lead directly to a crossing region with S_0. This path could provide an additional decay route for the photoexcited population, further decreasing the excited state lifetime, also in the presence of an energy barrier in the path involving the $\pi\pi^*1/S_0$ CI. This state has been shown to play an opposite role in the deactivation paths of C for which it acts as a central player for its long decay lifetime (of tens of ps).[7,36]

In the canonical base, the $n\pi^*$ state relaxes towards its minimum which is significantly lower in energy (≈0.6 eV) than the crossing-point (CI) with the ground state[7], and therefore, this state persists for tens of picoseconds, as shown by time-resolved IR experiments.[42] The etheno substituent makes this excited state more localized on the carbonyl moiety (Figure 3.13), reducing the participation of the ring with respect to C, making its out-of-plane motion an effective mechanism for non-radiative decay.

3.3. CONCLUSIONS

Both experimental and computational approaches have been followed to investigate the photophysics of 3,N4-etheno-2'-deoxycytidine under its neutral or protonated form (εdC and εdCH^+, respectively).

Steady-state and time-resolved experiments show that the etheno ring significantly affects εdC excited state properties with respect to those of the parent cytidine. Indeed, a 3-fold increase of the fluorescence quantum yield (ϕ_F) and average lifetime $<\tau>$ were observed for εdC in neutral solution. These values are dramatically amplified upon protonation at pH 3 with $<\tau>$ increasing from 1 to 11 ps and a 15-fold higher ϕ_F.

The experimental results have been rationalized with the help of quantum mechanical calculations. The pH dependence observed for the steady state measurements are well reproduced by theoretical calculations run at PCM/M052X/6-31G(d) level, which reveal for both εC and εCH^+ the presence of three different excited states, two bright ππ* states and a higher located dark nπ* state, involving the carbonyl lone pair.

As already reported for the canonical base 2'-deoxycytidine (dC), the emissive state is the lowest bright state ππ*1, with excitation mainly centered on orbitals of the C5-C6 bond; nonetheless, for the etheno derivative this state has a non-negligible contribution of the 5-membered ring atoms. Irrespectively of the pH, a major difference compared to dC is the absence of a dark nπ* singlet due to N3 lone pair, as the lowest energy dark state is a nπ* state involving the carbonyl lone pair.

Mapping of the main non-radiative decay pathway shows that the extra ring does not affect the typical pyrimidine main deactivation path, which corresponds to the ethene-like conical intersection with an out of plane deviation of the C5 and C6 substituents. Concerning the emission decays, the sub-ps lifetime (τ_1) is associated with deactivation in an area close to FC region or with the interplay with other bright states, whereas the longer-lived τ_2 is the result of deactivation from the ππ*1-min.

The slower kinetics of εdC (τ_2 of ca. 2 ps) and εdCH^+ (τ_2 of ca. 12 ps) compared to that of dC (τ_2 of ca. 1 ps) is the consequence of the need to overcome a sizeable energy barrier in the ππ*1 PES to reach the CI. The higher height of this barrier in the case of the protonated counterpart (~0.5 eV vs ~ 0.3 eV) is also in concordance with its longer lifetime τ_2.

Altogether, these results show that the addition of an extra etheno ring on the canonical dC alters its photobehavior. On the one hand, εdC exhibits a red-shifted absorption compared to dC, which increases the UVB fraction of sunlight that can be directly absorbed by εdC–containing DNA, and that can trigger undesired photolesions. However on the other hand, this structural change decreases the efficiency of the non-radiative deactivation by

lengthening the excited state lifetime. Similar changes have already been reported for 5-methyl-2'-deoxycytidine and associated with an increased intrinsic photoreactivity, especially in terms of cyclobutane pyrimidine formation.

Other lesions, such as the formylpyrimidine derivatives or (6-4) photoproducts, have also been proposed as internal DNA photosensitizer. Thus, the presence of a εdC adduct in a nucleic acid sequence could endanger the genome integrity not only because of its reported "dark" mutagenicity but also because, under irradiation, it might act as a doorway for undesired DNA photolability.

3.4. EXPERIMENTAL SECTION

3.4.1. Reagents and Solvents

3,N4-etheno-2'-deoxycytidine (εdC), sodium phosphate monobasic (Na_2HPO_4), sodium phosphate dibasic (Na_2HPO_4), sodium citrate dihydrate, citric acid, methanol, diethyl ether and acetonitrile were purchased from Carbosynth and Sigma-Aldrich and used as received. All the solvents were spectroscopic grade and buffers were made following the AAT Bioquest buffer protocol.

3.4.2. UV-Vis measurements

Absorption spectra were recorded in a Perkin Lambda 850 spectrophotometer, using quartz cuvette with optical path of 1 cm.

3.4.3. Steady state fluorescence

Spectra were measured upon 267 nm excitation with a Fluorolog-3 (Horiba, Jobin-Yvon) fluorimeter. Quantum yield was determined using thymidine monophosphate as reference ($\phi_F = 1.54 \times 10^{-4}$). [24]

3.4.4. Upconversion technique

A detailed description of the femtosecond fluorescence upconversion equipment has been given earlier. [43] Briefly, the 267 nm excitation was generated as a third harmonic of a femtosecond mode-locked Ti-sapphire laser (Coherent MIRA 900). The average

excitation power was set at 50 mW. The εdC solution (30 mL, 0.5 OD at 267 nm) was circulated in a flow system with a moving 1 mm flow-cell in order to avoid degradation.
The fluorescence from the cell was collected and focused into a 1 mm BBO type I crystal using two off-axes parabolic mirrors. It was further passed through a cutoff filter (WG305 or WG320) in order to eliminate the weak remaining UV excitation light.
After the mixing of the fluorescence and the IR gating pulse in the NL crystal, the generated sum-frequency light was focused on the entrance slit of a double monochromator equipped with a photomultiplier (Hamamatsu 1527P) connected to a photon counter (Stanford SR400). Fluorescence decays were recorded at selected wavelengths with parallel ($I_{par}(t)$) and perpendicular ($I_{perp}(t)$) excitation/detection configurations. These were performed by controlling the polarization of the exciting beam with a zero-order half wave plate. The temporal scans were repeated several times and then averaged in order to improve the statistics. For visualization, total fluorescence decay kinetics ($F(t)$) were constructed from the parallel and perpendicular signals according to the equation: $F(t) = I_{par}(t) + 2\, I_{perp}(t)$. [44]
Likewise, the fluorescence anisotropy r(t) was constructed according to the equation: $F(t) = (I_{par}(t) - I_{perp}(t))/F(t)$.
For the data treatment, parallel and perpendicular scans were treated together, allowing both the intensity and the anisotropy decays to be model-fitted simultaneously.
To this end, we performed a merged nonlinear fitting/deconvolution process using the impulse response model functions
$i_{par}(t) = (1 + 2r(t))f(t)$
$i_{perp}(t) = (1 - r(t))f(t)$
convoluted by the Gaussian instrument response function (irf) $G(t)$: $i(t) \otimes G(t)$. The fwhm value of the Gaussian irf was about 400 fs.
The model functions thus obtained were fitted to the experimental parallel (I_{par}) and perpendicular (I_{perp}) signals. Mono- or biexponential functions were used for $f(t)$, while $r(t)$ was taken as monoexponential. The average lifetime $<\tau>$ was determined from fitted parameters using the equation: $<\tau> = a_1\tau_1 + a_2\tau_2$,
Time resolved fluorescence spectra were recorded at magic angle between 300 and 385 nm by scanning the monochromator with a

step of 5 nm. The detection system is blind around 400 nm due to scattered excitation light and the red-wing of the spectrum was too weak to record separately. About 30 time-resolved spectra equally spaced in time were recorded over a time window of 3 or 30 ps. The full wavelength – time sampling was repeated several times and then averaged in order to improve the statistics.
Resulting spectra were corrected with regards to the spectral sensitivity of the system using a phenomenological correction curve obtained by comparing a reference FU spectrum to the corresponding steady-state spectrum. For the pH 7.4 recordings, the long-time spectra (> 200 ps) of the dye DMQ were used (external calibration), while for the pH 3 recordings, the long-time spectra (< 20 ps) of εdC itself were used (internal calibration).

3.4.5. Computational details

Water solution. In order to study the behavior of εdC and $\varepsilon dC(H)^+$ in water we have adopted the computational models depicted in Figure 3.12, where the sugar is mimicked by a methyl group, bulk solvent effects are included with the polarizable continuum (PCM) model,[45] and the effect of solute-solvent hydrogen bond interactions considered by explicitly including two H_2O molecules, with the arrangement shown in Figure 3.12. Our previous study on Cyt shows indeed that substitution of the sugar with methyl group does not have a significant impact on the excited state behaviour.[7] Calculations have been also performed without including explicit water molecules. DFT and TD-DFT, using the M052X functional,[46,47] have been used as reference computational model, since they have been already profitably adopted to study the photoactivated behavior of Cyt derivatives in solution.[4,7]

Gas Phase. In parallel we have mapped the PES of εCH and εCH^+ in the gas phase by Complete Active Space Self Consistent Field (CASSCF)[48,49] optimization of minima and state crossings and minimum energy path calculations. Energies have been corrected using second-order perturbation theory (CASPT2) in its single and multistate (MS)[50] formulation with an IPEA shift[51] of 0.0 a.u. and an imaginary level shift[52] of 0.3 a.u. The selected active space, 16 electrons in 12 orbitals, contains all the π and π* orbitals together

with the Lone Pairs of the O and N8 atoms for εCH. Since the latter is not present in εCH^+ the active space is reduced to 14 electrons in 11 orbitals. An equal weight state-average over 5 states was used throughout. To be consistent with the DFT calculations these calculations were also done using the 6-31G(d) basis set.

3.5. REFERENCES

(1) Serrano-Andrés, L.; Merchán, M. Are the Five Natural DNA/RNA Base Monomers a Good Choice from Natural Selection?: A Photochemical Perspective. *J. Photochem. Photobiol. C Photochem. Rev.* **2009**, *10* (1), 21–32.

(2) Crespo-Hernández, C. E.; Cohen, B.; Hare, P. M.; Kohler, B. Ultrafast Excited-State Dynamics in Nucleic Acids. *Chem. Rev.* **2004**, *104* (4), 1977–2019.

(3) Beckstead, A. A.; Zhang, Y.; De Vries, M. S.; Kohler, B. Life in the Light: Nucleic Acid Photoproperties as a Legacy of Chemical Evolution. *Phys. Chem. Chem. Phys.* **2016**, *18* (35), 24228–24238.

(4) Improta, R.; Santoro, F.; Blancafort, L. Quantum Mechanical Studies on the Photophysics and the Photochemistry of Nucleic Acids and Nucleobases. *Chem. Rev.* **2016**, *116* (6), 3540–3593.

(5) Photoinduced Phenomena in Nucleic Acids I; Barbatti, M., Borin, A. C., Ullrich, S., Eds.; *Springer*, **2015**.

(6) Banyasz, A.; Esposito, L.; Douki, T.; Perron, M.; Lepori, C.; Improta, R.; Markovitsi, D. Effect of C5-Methylation of Cytosine on the UV-Induced Reactivity of Duplex DNA: Conformational and Electronic Factors. *J. Phys. Chem. B* **2016**, *120* (18), 4232–4242.

(7) Martínez-Fernández, L.; Pepino, A. J.; Segarra-Martí, J.; Jovaišaitei, J.; Vaya, I.; Nenov, A.; Markovitsi, D.; Gustavsson, T.; Banyasz, A.; Garavelli, M.; Improta, R. Photophysics of Deoxycytidine and 5-Methyldeoxycytidine in Solution: A Comprehensive Picture by Quantum Mechanical Calculations and Femtosecond Fluorescence Spectroscopy. *J. Am. Chem. Soc.* **2017**, *139* (23), 7780–7791.

(8) Luis, S.; Ortiz-Rodríguez, A.; Crespo-Hernández, C. E.; Ortiz-Rodríguezrodríguez, L. A.; Hernández, H. Thionated

Organic Compounds as Emerging Heavy-Atom-Free Photodynamic Therapy Agents. *Chem. Sci.* **2020**, *11* (41), 11113–11123.

(9) Vendrell-Criado, V.; Rodriguez-Muniz, G. M.; Cuquerella, M. C.; Lhiaubet-Vallet, V.; Miranda, M. A. Photosensitization of DNA by 5-Methyl-2-Pyrimidone Deoxyribonucleoside: (6-4) Photoproduct as a Possible Trojan Horse. *Angew. Chem. Int. Ed.* **2013**, *52* (25), 6476–6479.

(10) Aparici-Espert, I.; Garcia-Lainez, G.; Andreu, I.; Miranda, M. A.; Lhiaubet-Vallet, V. Oxidatively Generated Lesions as Internal Photosensitizers for Pyrimidine Dimerization in DNA. *ACS Chem. Biol.* **2018**, *13* (3), 542–547.

(11) Vendrell-Criado, V.; Rodríguez-Muñiz, G. M.; Lhiaubet-Vallet, V.; Cuquerella, M. C.; Miranda, M. A. The (6-4) Dimeric Lesion as a DNA Photosensitizer. *ChemPhysChem* **2016**, *17* (13), 1979–1982.

(12) Francés-Monerris, A.; Hognon, C.; Miranda, M. A.; Lhiaubet-Vallet, V.; Monari, A. Triplet Photosensitization Mechanism of Thymine by an Oxidized Nucleobase: From a Dimeric Model to DNA Environment. *Phys. Chem. Chem. Phys.* **2018**, *20* (40), 25666–25675.

(13) Francés-Monerris, A.; Lineros-Rosa, M.; Miranda, M. A.; Lhiaubet-Vallet, V.; Monari, A. Photoinduced Intersystem Crossing in DNA Oxidative Lesions and Epigenetic Intermediates. *Chem. Commun.* **2020**, *56* (32), 4404–4407.

(14) Lineros-Rosa, M.; Frances-Monerris, A.; Monari, A.; Miranda, M. A.; Lhiaubet-Vallet, V. Experimental and Theoretical Studies on Thymine Photodimerization Mediated by Oxidatively Generated DNA Lesions and Epigenetic Intermediates. *Phys. Chem. Chem. Phys.* **2020**, *22*, 25661–25668.

(15) Barbin, A.; Bartsch, H.; Leconte, P.; Radman, M. Studies on

the Miscoding Properties of 1,N 6 -Ethenoadenine and 3,N 4 -Ethenocytosine, DNA Reaction Products of Vinyl Chloride Metabolites, during in Vitro DNA Synthesis. *Nucleic Acids Res.* **1981**, *9* (2), 375–387.

(16) Secrist, J. A.; Barrio, J. R.; Leonard, N. J.; Weber, G. Fluorescent Modification of Adenosine-Containing Coenzymes. Biological Activities and Spectroscopic Propertiest, *Biochem.* **1972**, 11(19), 3499–3506.

(17) Sattsangi, P. D.; Barrio, J. R.; Leonard, N. J. 1,N6-Etheno-Bridged Adenines and Adenosines. Alkyl Substitution, Fluorescence Properties, and Synthetic Applications. *J. Am. Chem. Soc.* **2002**, *102* (2), 770–774.

(18) Wolfe, A. E.; O'Brien, P. J. Kinetic Mechanism for the Flipping and Excision of 1,N6- Ethenoadenine by Human Alkyladenine DNA Glycosylase. *Biochemistry* **2009**, *48* (48), 11357–11369.

(19) Secrist, J. A.; Barrio, J. R.; Leonard, N. J. A Fluorescent Modification of Adenosine Triphosphate with Activity in Enzyme Systems: 1,N6-Ethenoadenosine Triphosphate. *Science* **1972**, *175* (4022), 646–647.

(20) Paula, A.; Loureiro, M. DNA Lesions Induced by Lipid Peroxidation Products in Cancer Progression. *Handbook Oxidative Stress Cancer Mech. Asp.* **2021**, 1–22.

(21) Barrio, J.; Sattsangi, P.; Gruber, B.; Dammann, L.; Leonard, N. Species Responsible for the Fluorescence of 3,N4-Ethenocytidine. *J. Am. Chem. Soc.* **1976**, 98(23), 7408–7413.

(22) Kistler, K. A.; Matsika, S. Cytosine in Context: A Theoretical Study of Substituent Effects on the Excitation Energies of 2-Pyrimidinone Derivatives. *J. Phys. Chem. A* **2007**, *111* (35), 8708–8716.

(23) Major, D. T.; Fischer, B. Theoretical Study of the PH-Dependent Photophysics of N1,N6-Ethenoadenine and

N3,N4-Ethenocytosine. *J. Phys. Chem. A* **2003**, *107* (42), 8923–8931.

(24) Onidas, D.; Markovitsi, D.; Marguet, S.; Sharonov, A.; Gustavsson, T. Fluorescence Properties of DNA Nucleosides and Nucleotides: A Refined Steady-State and Femtosecond Investigation. *J. Phys. Chem. B* **2002**, *106* (43), 11367–11374.

(25) Wang, X.; Martínez-Fernández, L.; Zhang, Y.; Zhang, K.; Improta, R.; Kohler, B.; Xu, J.; Chen, J. Solvent-Dependent Stabilization of a Charge Transfer State Is the Key to Ultrafast Triplet State Formation in an Epigenetic DNA Nucleoside. *Chem. Eur. J.* **2021**, 27(42), 10932–10940.

(26) Jimenez, R.; Fleming, G. R.; Kumar, P. V; Maroncelli, M. Femtosecond Solvation Dynamics of Water. *Nature* **1994**, *369* (6480), 471–473.

(27) Martinez-Fernandez, L.; Gustavsson, T.; Diederichsen, U.; Improta, R. Excited State Dynamics of 8-Vinyldeoxyguanosine in Aqueous Solution Studied by Time-Resolved Fluorescence Spectroscopy and Quantum Mechanical Calculations. *Molecules* **2020**, 25(4), 824-843.

(28) Pecourt, J. M. L.; Peon, J.; Kohler, B. DNA Excited-State Dynamics: Ultrafast Internal Conversion and Vibrational Cooling in a Series of Nucleosides. *J. Am. Chem. Soc.* **2001**, *123* (42), 10370–10378.

(29) Wondrazek, F.; Seilmeier, A.; Kaiser, W. Ultrafast Intramolecular Redistribution and Intermolecular Relaxation of Vibrational Energy in Large Molecules. *Chem. Phys. Lett.* **1984**, *104* (2), 121–128.

(30) Seilmeier, A.; Scherer, P. O. J.; Kaiser, W. Ultrafast Energy Dissipation in Solutions Measured by a Molecular Thermometer. *Chem. Phys. Lett.* **1984**, *105* (2), 140–146.

(31) Gottfried, N. H.; Seilmeier, A.; Kaiser, W. Transient Internal

Temperature of Anthracene after Picosecond Infrared Excitation. *Chem. Phys. Lett.* **1984**, *111* (4), 326–332.

(32) Schwarzer, D.; Troe, J.; Votsmeier, M.; Zerezke, M. Collisional Deactivation of Vibrationally Highly Excited Azulene in Compressed Liquids and Supercritical Fluids. *J. Chem. Phys.* **1996**, *105* (8), 3121–3131.

(33) D. Schwarzer; J. Troe, M. V.; Zerezke, M. Collisional Deactivation of Vibrationally Highly Excited Azulene in Supercritical XenonIEthane Mixtures. *Ber. Bunsenges. Phys. Chem.* **1997**, *101*, 595–599.

(34) Martin, R. L. Natural Transition Orbitals. *J. Chem. Phys.* **2003**, *118* (11), 4775–4777.

(35) Avila Ferrer, F. J.; Santoro, F.; Improta, R. The Excited State Behavior of Cytosine in the Gas Phase: A TD-DFT Study. *Comput. Theor. Chem.* **2014**, *1040–1041*, 186–194.

(36) Ma, C.; Cheng, C. C.-W.; Chan, C. T.-L.; Chan, R. C.-T.; Kwok, W.-M. Remarkable Effects of Solvent and Substitution on the Photo-Dynamics of Cytosine: A Femtosecond Broadband Time-Resolved Fluorescence and Transient Absorption Study. *Phys. Chem. Chem. Phys.* **2015**, *17* (29), 19045–19057.

(37) Kistler, K. A.; Matsika, S. Photophysical Pathways of Cytosine in Aqueous Solution. *Phys. Chem. Chem. Phys.* **2010**, *12* (19), 5024–5031.

(38) Zgierski, M. Z.; Fujiwara, T.; Kofron, W. G.; Lim, E. C. Highly Effective Quenching of the Ultrafast Radiationless Decay of Photoexcited Pyrimidine Bases by Covalent Modification: Photophysics of 5,6-Trimethylenecytosine and 5,6-Trimethyleneuracil. *Phys. Chem. Chem. Phys.* **2007**, *9* (25), 3206–3209.

(39) Trachsel, M. A.; Blaser, S.; Lobsiger, S.; Siffert, L.; Frey, H. M.; Blancafort, L.; Leutwyler, S. Locating Cytosine Conical

Intersections by Laser Experiments and Ab Initio Calculations. *J. Phys. Chem. Lett.* **2020**, *11* (9), 3203–3210.

(40) Trachsel, M. A.; Lobsiger, S.; Schär, T.; Blancafort, L.; Leutwyler, S. Planarizing Cytosine: The S 1 State Structure, Vibrations, and Nonradiative Dynamics of Jet-Cooled 5,6-Trimethylenecytosine. *J. Chem. Phys.* **2017**, *146(24)*, 244308(1-13).

(41) Yaghoubi Jouybari, M.; Liu, Y.; Improta, R.; Santoro, F. Ultrafast Dynamics of the Two Lowest Bright Excited States of Cytosine and 1-Methylcytosine: A Quantum Dynamical Study. *J. Chem. Theory Comput.* **2020**, *16* (9), 5792–5808.

(42) Keane, P. M.; Wojdyla, M.; Doorley, G. W.; Watson, G. W.; Clark, I. P.; Greetham, G. M.; Parker, A. W.; Towrie, M.; Kelly, J. M.; Quinn, S. J. A Comparative Picosecond Transient Infrared Study of 1-Methylcytosine and 5'-DCMP That Sheds Further Light on the Excited States of Cytosine Derivatives. *J. Am. Chem. Soc.* **2011**, *133* (12), 4212–4215.

(43) Miannay, F.-A. A.; Gustavsson, T.; Banyasz, A.; Markovitsi, D. Excited-State Dynamics of DGMP Measured by Steady-State and Femtosecond Fluorescence Spectroscopy. *J. Phys. Chem. A* **2010**, *114* (9), 3256–3263.

(44) Gustavsson, T.; Bányász, Á.; Lazzarotto, E.; Markovitsi, D.; Scalmani, G.; Frisch, M. J.; Barone, V.; Improta, R. Singlet Excited-State Behavior of Uracil and Thymine in Aqueous Solution: A Combined Experimental and Computational Study of 11 Uracil Derivatives. *J. Am. Chem. Soc.* **2006**, *128* (2), 607–619.

(45) Tomasi, J.; Mennucci, B.; Cammi, R. Quantum Mechanical Continuum Solvation Models. *Chem. Rev.* **2005**, *105* (8), 2999–3093.

(46) Zhao, Y.; Schultz, N. E.; Truhlar, D. G. Design of Density Functionals by Combining the Method of Constraint Satisfaction with Parametrization for Thermochemistry,

Thermochemical Kinetics, and Noncovalent Interactions. *J. Chem. Theory Comput.* **2006**, *2* (2), 364–382.

(47) Zhao, Y.; Truhlar, D. G. Density Functionals with Broad Applicability in Chemistry. *Acc. Chem. Res.* **2008**, *41* (2), 157–167.

(48) Andersson, K.; Malmqvist, P. A.; Roos, B. O.; Sadlej, A. J.; Wolinski, K. Second-Order Perturbation Theory with a CASSCF Reference Function. *J. Phys. Chem.* **1990**, *94* (14), 5483–5488.

(49) Andersson, K.; Malmqvist, P.; Roos, B. O. Second-order Perturbation Theory with a Complete Active Space Self-consistent Field Reference Function. *J. Chem. Phys.* **1992**, *96* (2), 1218–1226.

(50) Finley, J.; Malmqvist, P.-Å.; Roos, B. O.; Serrano-Andrés, L. The Multi-State CASPT2 Method. *Chem. Phys. Lett.* **1998**, *288*, 299–306.

(51) Ghigo, G.; Roos, B. O.; Malmqvist, P.-Å. A Modified Definition of the Zeroth-Order Hamiltonian in Multiconfigurational Perturbation Theory (CASPT2). *Chem. Phys. Lett.* **2004**, *396* (1), 142–149.

(52) Forsberg, N.; Malmqvist, P.-Å. Multiconfiguration Perturbation Theory with Imaginary Level Shift. *Chem. Phys. Lett.* **1997**, *274* (1), 196–204.

CHAPTER 4

A MECHANISTIC STUDY OF ETHENO ADDUCTS PHOTOSENSITIZATION

4.1. INTRODUCTION

Photosensitization of DNA bases has attracted considerable interest in order to understand the interaction between light and chemicals, which is responsible for the appearance of harmful effects such as aging, phototoxicity, photocarcinogenesis, etc. [1]

The main types of mechanisms involved in DNA photosensitization correspond to Type I or II processes, together with triplet-triplet energy transfer (TTET). [2,3] The resulting primary photolesions are not always photostable and might suffer further photodegradation. However, up to now the photobehavior of DNA lesions has been the subject of a limited number of studies, most of them centered on the photolability of 8-oxo-7,8-dihydroguanosine (8-oxoG) as the main oxidatively generated DNA damage through Type I and Type II processes. [4,5] In this context, mutagenic properties of the formed secondary products have been demonstrated for 2,2-diamino-oxazolone (Ox) [6], spiroiminodihydantoin (Sp) or guanidinohydantoin (Gh). [7]

Concerning the etheno adducts (ε-adducts), the chemical stability of εdG has been tackled in the literature to evaluate the accuracy of the analytical methods employed in its quantification as an oxidative stress biomarker. [8] Thus, its degradation by hydrolysis under acidic condition (pH 2), Fenton reaction and one electron oxidation by $SO_4^{\bullet-}$ has been evidenced, [8] ending up in its repaired nucleotide, dG, for those two last processes.

Furthermore, the reactivity of ε-adducts with $^1O_2$ has also been studied few years ago. [9] In this work, thermally generated $^1O_2$, using naphthalene-derived endoperoxides, reacts with εdG and allows regeneration of the original nucleoside, dG. Bimolecular rate constants for $^1O_2$ quenching by ε-adducts ranging from 2.3 to 4.4×10^6 $M^{-1}s^{-1}$ have been determined. These values are close to that measured for quenching by dG of ca. 5.4×10^6 $M^{-1}s^{-1}$, [9] which is the only nucleoside able to react with this ROS. However, the repair was only detected for the εdG lesion pointing towards a physical quenching of $^1O_2$ by εdA and εdC. The proposed mechanism for Type II reactivity of εdG involves formation of an oxetane

intermediate, which after cleavage and elimination leads to restored dG.

With this background, photosensitization of the three ε-adducts by Rose Bengal (Figure 4. 1, RB^{2-}) and 4-carboxybenzophenone (CBP) was considered of interest in this Chapter.

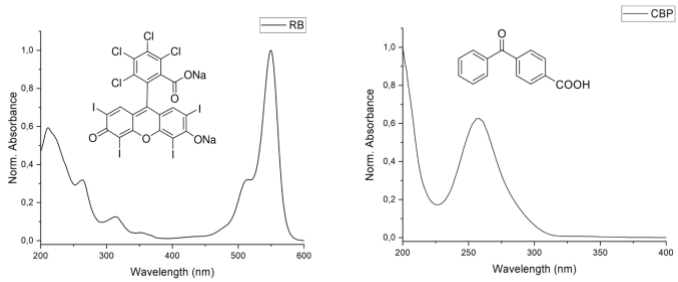

Figure 4. 1. Structure and absorption spectra of Rose Bengal (RB^{2-}) in water, left and 4-carboxybenzophenone (CBP) ACN:H_2O (1:1, w/w), right.

On the one hand, RB^{2-} is a well-known photosensitizer that has been widely used due to its high quantum yield of $^1O_2$ formation (Φ_Δ = 0.76 in water). [10] Therefore, its mode of action has been mostly attributed to a Type II mechanism, ie. reaction between the substrate and $^1O_2$. In this context, RB^{2-} has been used to investigate the photoproducts obtained from $^1O_2$ attack to nucleoside or DNA molecules [4,5], leading to the formation of 8-oxoG, Ox, Sp or Gh. However, it has also been shown that RB^{2-} could undergo oxidative and reductive triplet excited state quenching in biological media. [11] Thus, the potential role of each pathway (Type I *vs* Type II) has to be considered during ε-adduct photosensitization by RB^{2-}.

On the other hand, benzophenone and its derivatives such as CBP have been described as classical and paradigmatic chromophores. [12] They are well-established DNA photosensitizers able to yield a large variety of lesions arising from Type I (electron transfer and hydrogen abstraction) or Type II processes, but also from triplet-triplet energy transfer (TTET) to thymine, the nucleobase with the lowest triplet excited state energy. In this chapter, CBP is used as a water-soluble derivative, and ε-adduct photosensitization was run under anaerobic conditions, to prevent

Type II mechanism and focus the attention on Type I and TTET processes.

4.2. RESULTS

4.2.1. Spectroscopic properties of etheno adducts

In a first step, spectroscopic properties of etheno adducts were determined and compared to those of the canonical nucleosides. As shown in Figure 4. 2 (black line) and summarized in Table 4. 1, a shift of the absorption maximum, ranging from 34 nm for εdG to 3 nm for εdC, was observed for the three lesions in aqueous solution at pH 7.4. This is in agreement with the presence of the extra etheno bridge that extends the π conjugation initially present in the bases, leading to a bathochromic effect of the absorption bands. Moreover, although the maxima (λ_{max}) for the three ε-adducts are located in the UVC, they all exhibit a tail in the UVB region, which reaches the UVA for εdA and εdG.

Table 4. 1. Absorption and singlet excited state properties of the ε-adducts and DNA bases in aqueous solution: Absorption maxima (λ_{max}), molar absorption coefficients (ε), fluorescence maxima (λ_f), fluorescence quantum yields (ϕ_f) and lifetimes (τ_f), singlet excited state energies (E_s).

	λ_{max} (nm)	ε ($M^{-1}cm^{-1}$)	λ_f (nm)	ϕ_f	τ_f (ps)	E_s ($kJ\ mol^{-1}$)
εdA	275	5760	410	0.12	$23 \cdot 10^3$	349
dA[a]	260	14930	307	$0.86 \cdot 10^{-4}$	0.17	-
εdC	273	13200	325	$1.84 \cdot 10^{-4}$	0.47 (τ_1), 1.89 (τ_2)	403
dC[a]	270	9300	328	$0.89 \cdot 10^{-4}$	0.22 (τ_1), 0.96 (τ_2)	-
εdG	286	10530	374	$6.5 \cdot 10^{-4}$	0.57 (τ_1), 8.11 (τ_2)	364
dG[a]	252	13850	334	$0.97 \cdot 10^{-4}$	0.16 (τ_1), 0.78 (τ_2)	-

[a] data obtained from [13]

Moreover, fluorescence emission was monitored in PBS at pH 7.4 (Figure 4. 2, red line). As a general trend, the ε-adducts band is red-shifted in comparison to that of the corresponding nucleobase (Table 4. 1). In this context, both εdA and εdG exhibit a broad signal with a maximum at 410 and 374 nm, respectively, while εdC emission spectrum is sharper and centered at 325 nm. A large Stoke shift, ca. 100 nm, was observed for purine derivatives. Fluorescence quantum yields were determined using thymidine monophosphate as reference ($\phi_f = 1.54 \times 10^{-4}$) [13]. The obtained values for εdC and εdG, in the range of 10^{-4}, are somewhat higher compared to that of the nucleobases. In addition, a pronounced enhancement of εdA emission was observed with ϕ_f of ca. 0.12, which is three orders of magnitude higher than that of the other etheno lesions.

Table 4. 2. Triplet excited state properties of the ε-adducts: Phosphorescence maxima (λ_p) and triplet excited state energy (E_T).

	λ_p (nm)	E_T (kJ mol^{-1})
εdA[b]	500	278
dA[a]	380	320
εdC[b]	480	281
dC[a]	371	334
εdG[b]	415	314
dG[a]	376	326

[a] data obtained from [14], for monophosphate nucleotides at 77K in ethylene glycol/water.
[b] data obtained in ethanol at 77K

Triplet excited states were first studied at room temperature by laser flash photolysis. No triplet-triplet transient absorption signal was obtained under direct 266 nm excitation of degassed aqueous solutions of ε-adducts.

a)

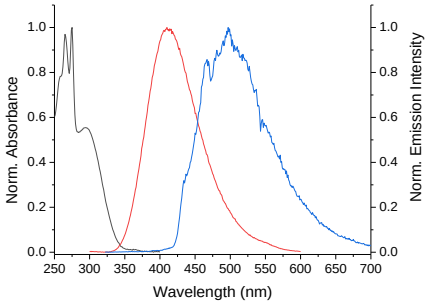

b)

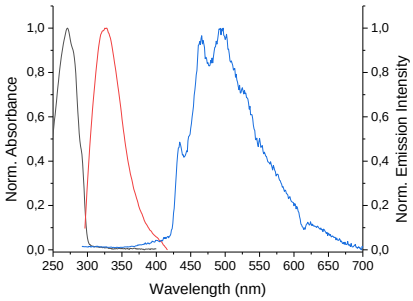

c)

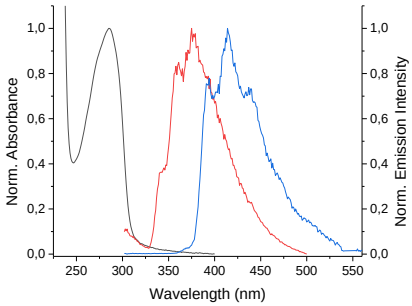

Figure 4. 2. Room temperature absorption (black) and fluorescence (red) spectra in PBS at pH 7.4, and phosphorescence emission in ethanol at 77K (blue). λ_{ex}(εdA)=310 nm; λ_{ex}(εdC)=275 nm; λ_{ex}(εdG)=283 nm a) εdA, b) εdC, c) εdG.

By contrast, phosphorescence experiments performed at 77K in EtOH showed emission for the three compounds (Figure 4. 2, blue line). Triplet excited state energies (E_T) were determined from

the λ value that corresponds to the 20% of the maximum phosphorescence intensity; they are ranging between 278 and 314 kJ mol^{-1} (Table 4. 2). As in the case of the singlet excited states, these energies are lower than those reported for the corresponding bases.

Finally, an overlap between the fluorescence and phosphorescence spectra of the purine-derived etheno adducts, observed in Figure 4. 2, is not present for εdC.

4.2.2. Photosensitization studies

Steady-state photolysis of ε-adducts in PBS revealed their lack of photoreactivity under direct irradiation. Therefore, photosensitization studies were addressed using RB^{2-} and CBP, whose absorption at λ>350 nm ensures their selective excitation in the presence of the lesions.

4.2.2.1. Photosensitization of ε-adducts by Rose Bengal

4.2.2.1.1. Steady-state photolysis

4.2.2.1.1.1. Aerobic conditions

Rose Bengal is mainly known as a Type II photosensitizer with a singlet oxygen quantum yield ϕ_Δ of ca. 0.76 [11] and low lying singlet and triplet excited states (with energies of 213 and 176 kJ mol^{-1}, respectively). [10] In this context, to investigate the reactivity of singlet oxygen with the ε-adducts, steady state photolysis was performed using RB^{2-} solutions in deuterated water with a ratio of 2:1 between the lesion (20 μM) and RB^{2-} (10 μM). The solutions were irradiated using a Luzchem photoreactor equipped with eight fluorescent tubes of white light (FSL-T5 8W/765) with an emission between 350-700 nm and analyzed by HPLC to follow the kinetics of ε-adduct consumption and photoproduct formation.

Although the ε-adducts do not exhibit absorption in this range, control experiments were performed by irradiating the lesion alone

(Figure 4. 3). Expectedly, no changes were observed by HPLC showing their photostability under these conditions of direct irradiation.

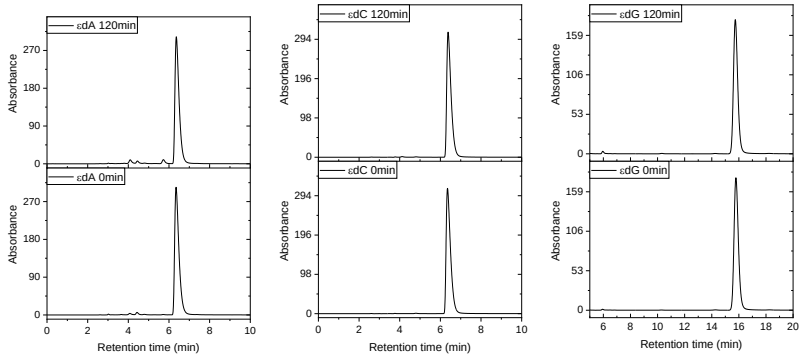

Figure 4. 3. HPLC chromatograms registered at 260 nm obtained after 0 and 120 min of irradiation of a solution of 20:10 μM of etheno adduct and RB^{2-} in deuterated water using white light.

Conversely, steady-state photolysis of the ε-adducts in the presence of RB^{2-} showed that the initial peak decreases as a function of irradiation time (Figure 4. 4). An almost complete conversion was observed after 30 min for εdC and εdA with the formation of only one product eluting at t_R = 4.0 and 5.9 min, respectively. The guanine-derived adduct, εdG, exhibited a higher reactivity, and its consumption gave rise to the formation of three main peaks, at retention times (t_R) of 6.4 min, 9.2 and 11 min (Figure 4. 4). These three peaks exhibit a similar trend as their intensity increases during the first 15 min and decreases afterwards. This behavior is characteristic of reaction intermediates, and it ends up with the formation of secondary photoproducts eluting at shorter irradiation time (see Figure 4. 4c, inset). The signal at t_R= 5 min is assigned to an impurity since it appears from the beginning and remains stable during the irradiation (Figure 4. 4c, inset).

Interestingly, the peaks eluting at t_R = 4.0 min for εdC and 5.9 min for εdA and εdG were assigned to the original nucleosides dC, dA and dG; this assignment was confirmed by comparison with authentic samples and by UPLC-HRMS analysis of the irradiation mixtures.

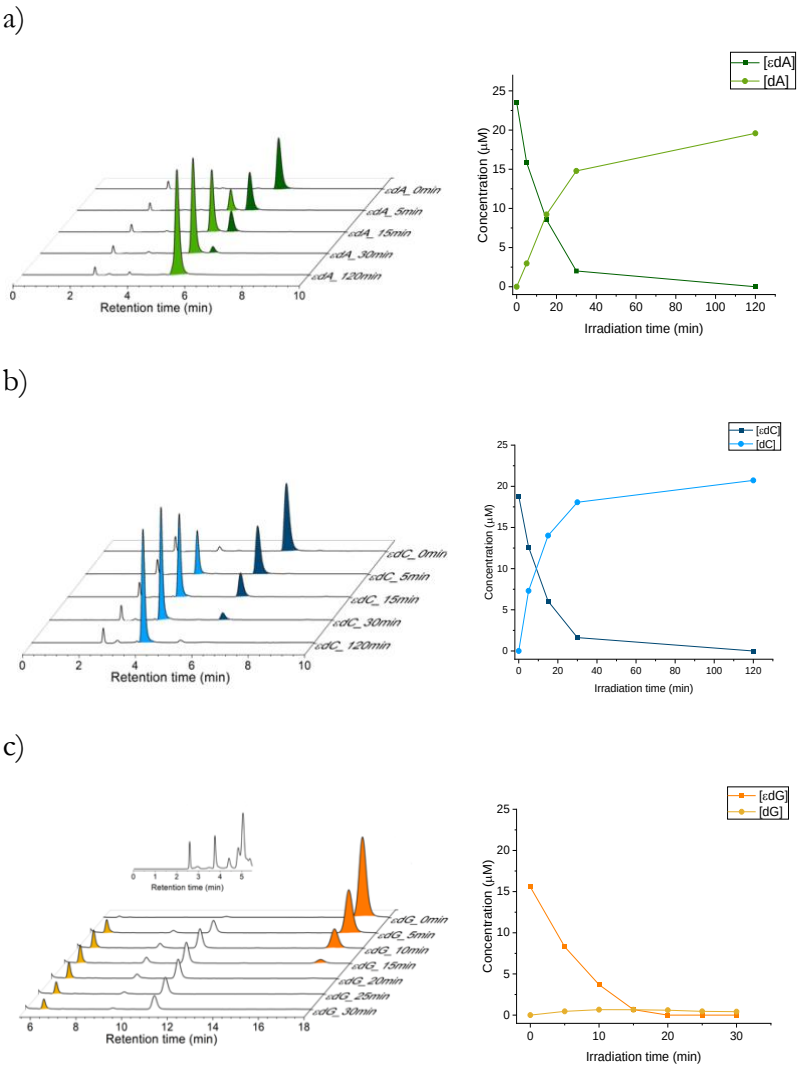

Figure 4. 4. Left, HPLC chromatograms registered at 260 nm for an aerated solution of 20 μM ε-adduct in presence of 10 μM RB upon irradiation at different times in D_2O. Right, variation of the concentration of damaged (square) and repaired nucleoside (circle) as a function of the irradiation time. a) εdA, b) εdC, c) εdG, inset: chromatogram at short retention times after 30 min of irradiation.

For εdG, the intermediates at 9.2 and 11 min were not identified. However, they can correspond to the compounds depicted in Figure 4. 5, previously reported in the literature. [9]

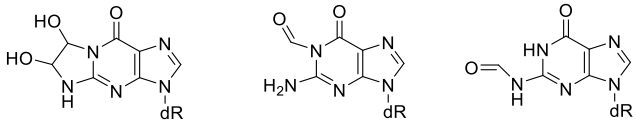

Figure 4. 5. Possible intermediates of εdG photodegradation.

Thus, RB^{2-} photosensitization of etheno adducts under aerobic conditions leads back to the original nucleosides, and thus provides a photorepair process of these lesions. Recovery of the nucleosides appears to occur in high yields of 100% and 83% after 120 min of irradiation for εdC and εdA, respectively (Figure 4. 4). By contrast, dG formation yield reaches only 4% after 15 min and then decreases. This behavior is due to the particular reactivity of this nucleoside with $^1O_2$, which is the only DNA nucleobase able to react with this ROS to yield products such as Sp or Gh. [15]

4.2.2.1.1.2. Anaerobic conditions

Next, experiments were performed under deaerated conditions in order to investigate the possible involvement of other pathways in the photosensitization process. Therefore, the samples were prepared as described in the previous section and flushed with nitrogen for 15 minutes before irradiation.

As shown in Figure 4. 6, effective photodegradation of all the ε-adducts was observed and gave rise to the original nucleosides as the only detectable product, with a yield of 86% for dA and 100% for dC after 120 min of irradiation. As under aerobic conditions, a faster kinetics of photodegradation was observed for εdG. Once again, formation of dG was not quantitative; however, it reached yields of ca. 32% after 15 min of irradiation. An intermediate product, reaching a maximum intensity after the same irradiation time, also appeared at t_R=10 min together with minor products at short retention times (Figure 4. 6c, inset).

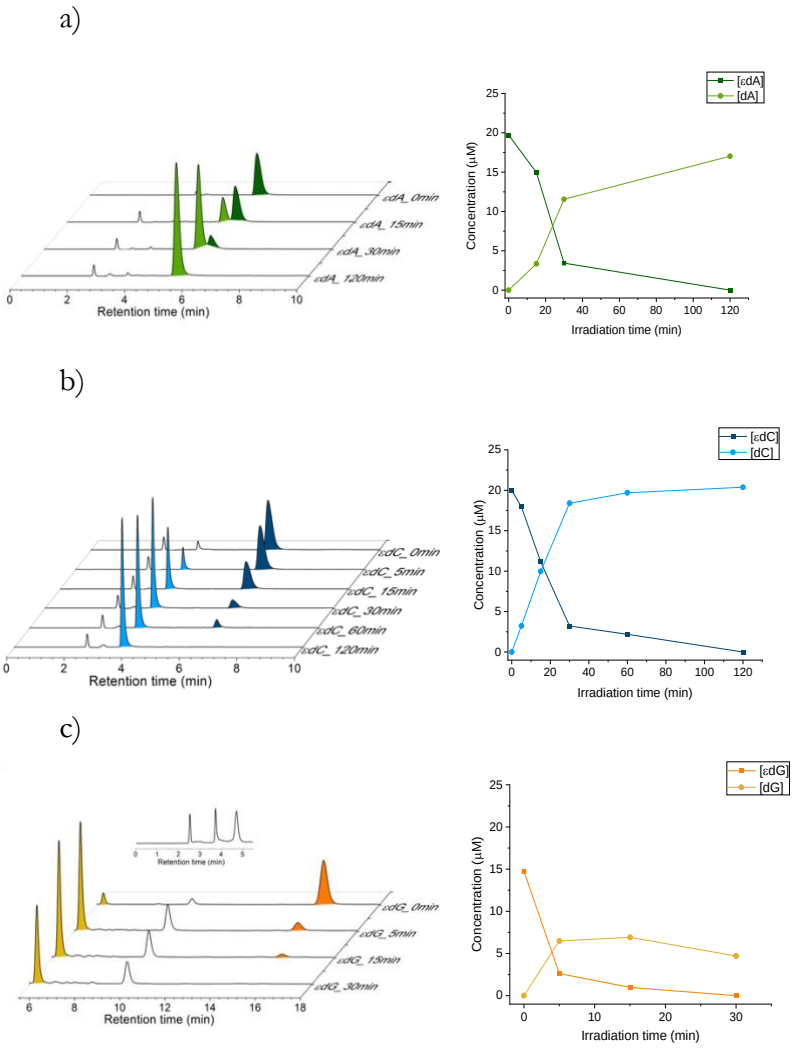

Figure 4. 6. Left, HPLC chromatograms registered at 260 nm for a degassed solution of 20 μM ε-adducts in presence of 10 μM RB upon irradiation at different times in D_2O. Right, variation of the concentration of damaged (square) and repaired nucleoside (circle) with irradiation time. a) εdA, b) εdC, c) εdG, inset: chromatogram at short retention times after 30 min of irradiation.

Indeed, the dG behavior is related to the fact that guanosine is the nucleobase with the lowest oxidation potential, and thus, the most predisposed to undergo oxidation by one electron transfer.

Therefore, after its formation, dG may suffer an oxidative process leading to photoproduct formation (Figure 4. 7). This would explain why, by contrast to εdA and εdC, RB^{2-} photosensitization does not yield to a high yield of εdG to dG conversion. In fact, both aerobic and anaerobic photolysis of dG under the same conditions reveal two photoproducts at t_R= 2.5 and 3.7 min, which also appear in εdG irradiations.

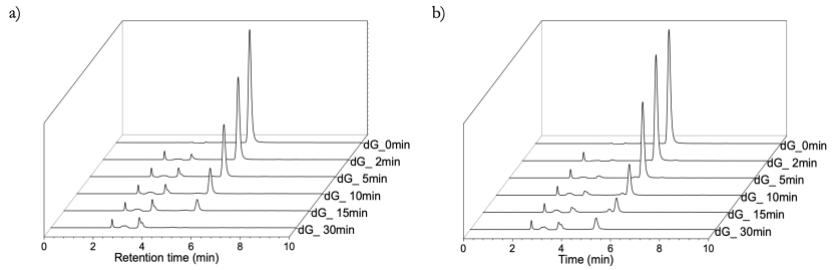

Figure 4. 7. HPLC chromatograms registered at 260 nm for a solution of 20 μM dG in presence of 10 μM RB^{2-} upon irradiation at different times in D_2O a) under air, b) under N_2.

Table 4. 3. Yields of the nucleoside formation for anaerobic and aerobic photolysis of the ε-adducts after 2 hours of irradiation for εdA and εdC and 15 min for εdG.

	Anaerobic	***Aerobic***
dA	86%	83%
dC	100%	100%
dG	32%	4%

Comparison of the obtained data under aerobic and anaerobic conditions showed that the role played by $^1O_2$ in the repair process is not predominant as the reaction also occurs in high yields in the absence of oxygen (Table 4. 3). Thus, the next step was to consider the photophysical study of RB^{2-} excited states and singlet oxygen in the presence of etheno derivatives to get more insight into the photosensitization routes.

4.2.2.1.2. Photophysical study of Rose Bengal in the presence of etheno adducts

4.2.2.1.2.1. Singlet oxygen generation and quenching by the lesions

The study of the interaction of the ε-etheno adducts with singlet oxygen using RB^{2-} as a photosensitizer was performed by time-resolved phosphorescence. Experiments were run recording $O_2(^1\Delta g)$ characteristic signal at 1270 nm after excitation at 532 nm of RB^{2-} deuterated water solutions at a concentration of 5 μM (A_{532}=0.18). A shortening of the singlet oxygen lifetime, initially τ_0 of ca. 66 μs, was observed after addition of the etheno derivatives (Figure 4. 8).

The $^1O_2$ quenching rate constants ($k_q(^1O_2)$-ε in $M^{-1}s^{-1}$) were determined from the Stern-Volmer plots applying the equation $1/\tau=1/\tau_0 + k_q(^1O_2)\text{-}\varepsilon \times [\varepsilon\text{-adduct}]$, where τ_0 and τ are the $^1O_2$ lifetime (in s) in the absence and in the presence of a concentration [ε-adduct] of the quencher (in M). Similar values were obtained for the three adducts with $k_q(^1O_2)$-ε in the order of 10^6 $M^{-1}s^{-1}$ (Table 4. 4).

Table 4. 4. Quenching rate constants of $^1O_2$, generated with RB^{2-}, by etheno adducts.

	$k_q(^1O_2)$-ε $(M^{-1}s^{-1})$
εdA	$9.2 \cdot 10^5$
εdC	$1.2 \cdot 10^6$
εdG	$3.6 \cdot 10^6$

Moreover, a decrease of the top emission intensity was observed for all the quenchings, this was especially pronounced for εdA and εdC (Figure 4. 8 a & b) where the final adduct concentration is higher (εdG is not soluble at concentration higher than 0.4 mM). This decrease could be the result of a lower

formation yield of the singlet oxygen precursor, *ie.* the Rose Bengal triplet excited state ($^3RB^{2-}$*), as the concentration of the quencher increases. The changes in $^3RB^{2-}$* population can be due to several processes.

First, the screening effect resulting from absorption of the etheno derivatives can be discarded due to their lack of absorption at the excitation wavelength. Another option is an interaction of the ε-adducts with the singlet excited state of the photosensitizer ($^1RB^{2-}$*), that would decrease the excited molecules available for ISC and population of $^3RB^{2-}$*. In order to investigate this possibility, steady-state fluorescence experiments were carried out (Figure 4.9). Solutions were prepared as described above for $^1O_2$ detection experiments and increasing amounts of ε-adducts were added to the RB^{2-} solution.

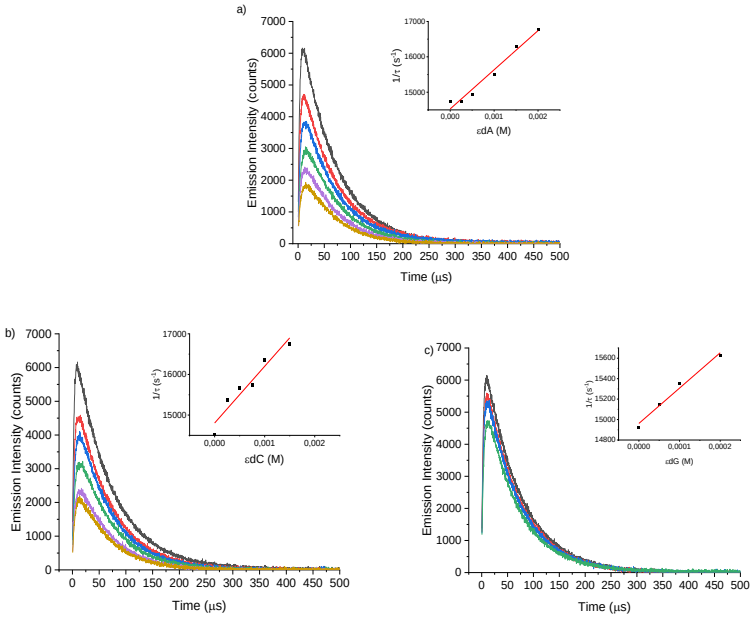

Figure 4. 8. Time-resolved $^1O_2$ phosphorescence signal and their corresponding Stern-Volmer plot obtained from aerated D_2O solutions of 5 μM RB in presence of increasing amounts of etheno adducts (from 0 to 2 and 1.5 mM for εdA and εdC, respectively) and from 0 to 0.2 mM in case of εdG. a) εdA, b) εdC and c) εdG.

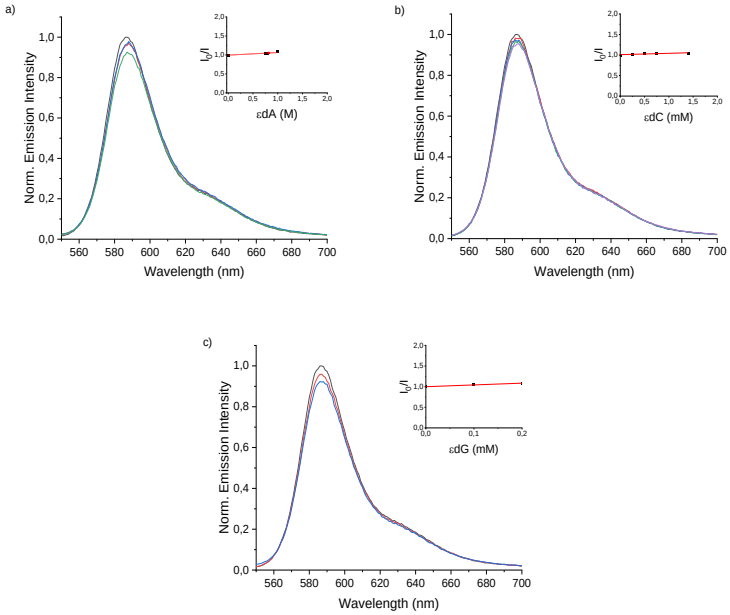

Figure 4. 9. Fluorescence emission spectra obtained from 5 μM RB^{2-} (λ_{ex}= 532 nm) in presence of increasing amounts of etheno adducts, from 0 to 1 and 1.4 mM for εdA and εdC, respectively and from 0 to 0.2 mM in case of εdG, a) εdA b) εdC and c) εdG. Inset: corresponding Stern-Volmer plot.

No significant decrease of $^1RB^{2-*}$ emission intensity was observed (Figure 4. 9). Time-resolved studies could not be performed due to the short lifetime of $^1RB^{2-*}$ of ca. 0.4 ns, which is below the time resolution of our setup. [16] Therefore, on the basis of the steady-state fluorescence results, the decrease in the top emission intensity observed in Figure 4. 9 is not due to a quenching of $^1RB^{2-*}$.

Another explanation could rely on the photodegradation of the RB^{2-} during the measurements (each trace is obtained after an accumulation time of 3 min). However, no significant changes were observed when comparing the UV-Vis absorption spectra of the solutions before and after the $^1O_2$ measurement (Figure 4. 10).

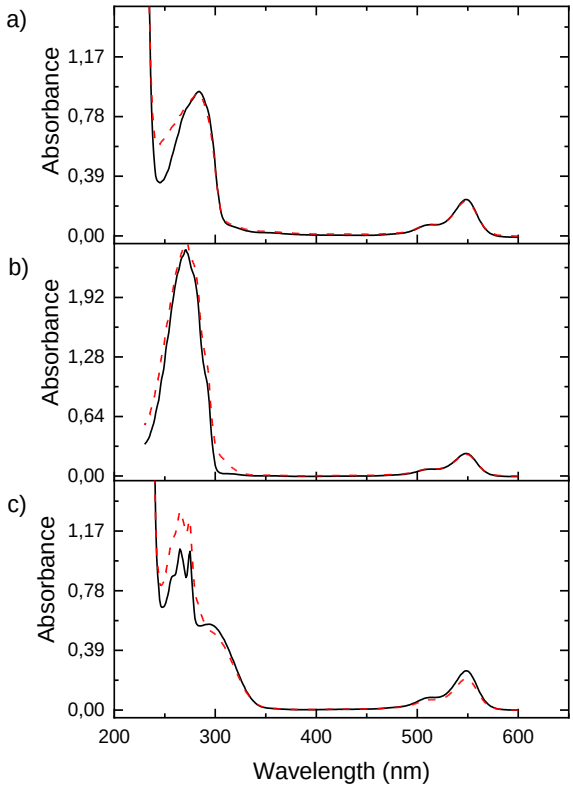

Figure 4. 10. Absorbance spectra of 0.5 mM solution of the three etheno adducts with RB before (solid line) and after (dot line) excitation at 532 nm in direct $^1O_2$ detection experiment. a) εdA b) εdC and c) εdG

4.2.2.1.2.2. RB^{2-} Triplet channel

4.2.2.1.2.2.1. Phosphorescence experiments

Another option is a direct interaction between the triplet excited state of Rose Bengal and the ε-adducts. Indeed, upon excitation, formation of the triplet manifold is the main route of deactivation with an efficient intersystem crossing, ϕ_{ISC} of ca. 0.8, thus the direct

reactivity of this state with the lesions can play an important role in the photochemical processes. [11,17,18]

In this context, phosphorescence experiments were performed using RB^{2-} solutions (5 μM) prepared in deuterated water and flushed with N_2 just before the measurements.

The phosphorescence emission was registered at room temperature after excitation at 532 nm. It showed a maximum at 730 nm, with a lifetime τ_0 of ca. 210 μs. Decays were recorded in the presence of increasing amounts of the etheno adducts (Figure 4. 11), and the bimolecular quenching rate constants $k_q(^3RB^{2-*})P\text{-}\varepsilon$, summarized in Table 4. 5, were obtained from the Stern-Volmer plots (see insets, Figure 4. 11).

Table 4. 5. Bimolecular quenching rate constants, in $M^{-1}s^{-1}$, of $^3RB^{2-*}$ by ε-adducts determined from the phosphorescence, $k_q(^3RB^{2-*})P\text{-}\varepsilon$, and from laser flash photolysis, $k_q(^3RB^{2-*})LFP\text{-}\varepsilon$, experiments.

	$k_q(^3RB^{2-*})P\text{-}\varepsilon$	$k_q(^3RB^{2-*})LFP\text{-}\varepsilon$
εdA	$1.5 \cdot 10^6$	$3.8 \cdot 10^6$
εdC	-	-
εdG	$1.3 \cdot 10^8$	$8.5 \cdot 10^7$

a)

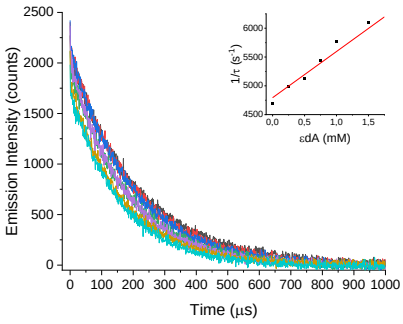

b)

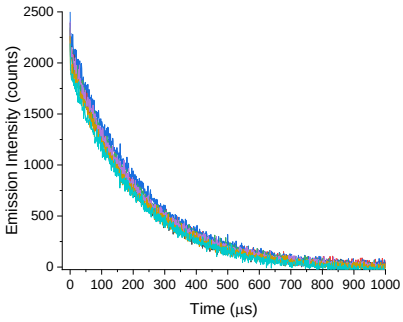

c)

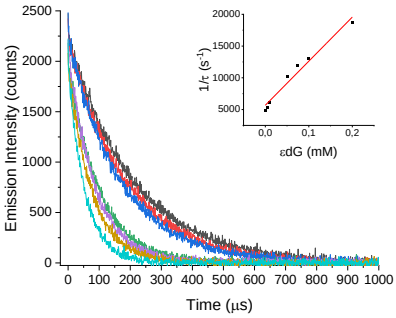

Figure 4. 11. Time-resolved $^3RB^{2-*}$ phosphorescence signals, monitored at 690 nm, in N_2 and their corresponding Stern-Volmer plot obtained from 5 µM RB^{2-} in presence of increasing amounts of etheno adducts a) εdA b) εdC and c) εdG (from 0 to 2 mM and 0 to 0.2 mM in the case of εdG).

These phosphorescence experiments showed that $^3RB^{2-}*$ is quenched by εdA and εdG, with a constant two orders of magnitude higher for the latter. Interestingly, for εdG, the quenching rate constant of $^3RB^{2-}*$ is also two orders of magnitude higher than that of $^1O_2$. The most surprising result is the absence of interaction between εdC and $^3RB^{2-}*$, which is in contrast with the efficient photoreactivity observed during the steady-state photolysis.

Therefore, laser flash photolysis experiments were carried out in order to get more insight into the quenching mechanism and to investigate the presence of other intermediates such as radical species in the ε-adducts photosensitization process and especially for εdC.

4.2.2.1.2.2.2. Laser flash photolysis

Previous work revealed that 532 nm laser excitation of RB^{2-} leads not only to the formation of its triplet excited state but also to oxidative and reductive processes leading to the corresponding ion radicals. [10] Figure 4.12 shows the formation of those radicals arising from an electron exchange between $^3RB^{2-}*$ and a molecule of RB^{2-} in its ground state to give both the reduced ($RB^{\bullet 3-}$) and oxidized ($RB^{\bullet -}$) species (Figure 4. 12a). The same species can also be obtained from a disproportionation (Figure 4. 12c) taking place between two $^3RB^{2-}*$. Finally, the formed radical ions can undergo back electron transfer (k_{eT}, Figure 4. 12b) and deactivate to regenerate RB^{2-}.

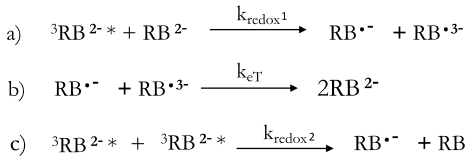

Figure 4. 12. Scheme of the formation and deactivation of RB^{2-} radicals.

Thus, experiments were performed by means of a nanosecond pulsed laser (Nd:YAG) using 532 nm as excitation wavelength. Figure 4. 13 shows the transient absorption spectra of a degassed

solution of RB^{2-} in deuterated water at different times after the laser pulse. The spectrum is in agreement with those described in the literature for RB^{2-},[10] and provides evidence for the formation of three transient species. The first one, exhibiting three maxima at λ_{abs}^{max} 380, 465 and 590 nm, is attributed to the triplet-triplet transition $^3RB^{2-}*$, that starts to decay just after the pulse having a lifetime of $\tau(^3RB^{2-}*) = 82$ μs.

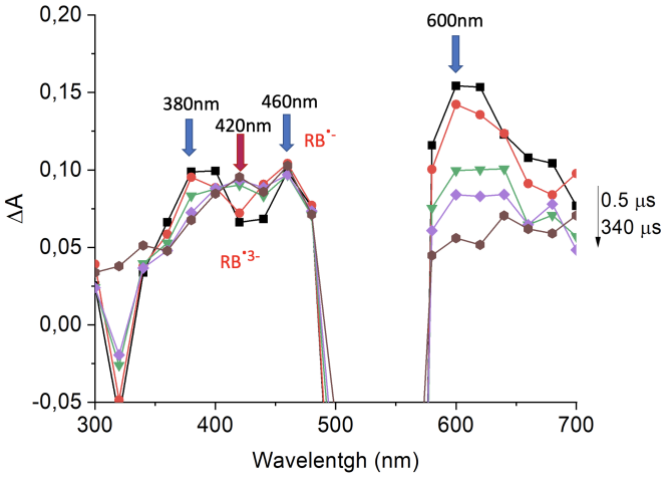

Figure 4. 13. Transient absorption spectra of Rose Bengal under N_2 in deuterated water after 532 nm excitation.

The other two transients are longer-lived than $^3RB^{2-}*$ and appear at λ_{abs}^{max} 420 and 460 nm with a relative delay after the pulse. On the basis of literature data [10], they were assigned to the oxidized ($RB^{\bullet-}$) and reduced ($RB^{\bullet 3-}$) forms.

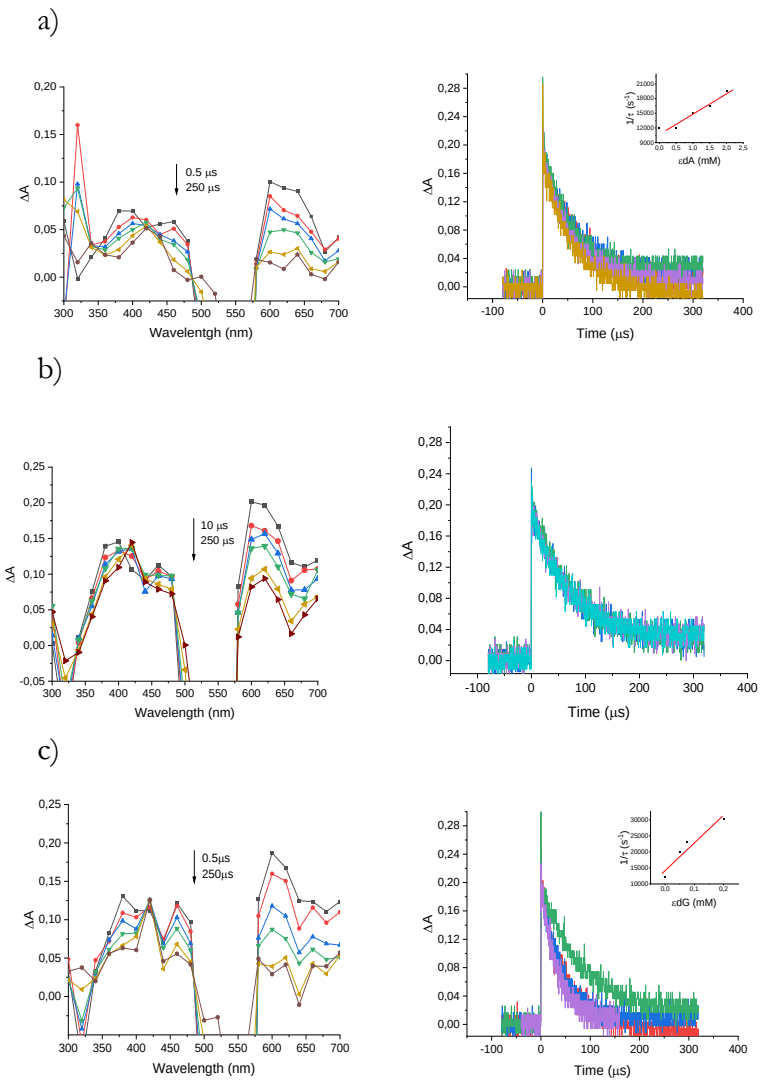

Figure 4. 14. Left, Transient absorption spectra of RB^{2-} in presence of ε-adduct (2 mM for εdA and εdC, 0.2 mM for εdG) in D_2O at different time after the 532 nm laser pulse. Right, decay signal monitored at 610 nm at different ε-adduct amounts; a) εdA, b) εdC and c) εdG.

Quenching experiments were run by adding increasing amounts of the different etheno derivatives. For the three lesions, the signal at 600 nm assigned to the triplet-triplet transition was monitored, and bimolecular quenching rate constants of the same

order of magnitude as those obtained during the luminescence studies were determined. For εdA and εdG, the k_q values are of ca. $3.8 \cdot 10^6$ and $8.5 \cdot 10^7$ $M^{-1}s^{-1}$, respectively; and no changes in the decay were observed in the case of εdC (Table 4. 5).

Interesting outcomes can be drawn from the radical ion signals. As shown in Figure 4. 14, when εdA and εdG are added to the RB^{2-} solution, the signals at 380, 465 and 590 nm decay, whereas the transient absorption corresponding to the photosensitizer reduced form $RB^{\bullet 3-}$ at 420 nm remains stable.

The spectra obtained in the presence of εdC are different (Figure 4. 14b) and are quite similar to those obtained for RB^{2-} alone. No clear decrease of the transient absorption bands below 500 nm is observed, whereas the signal at 590-600 nm is disappearing as a function of time.

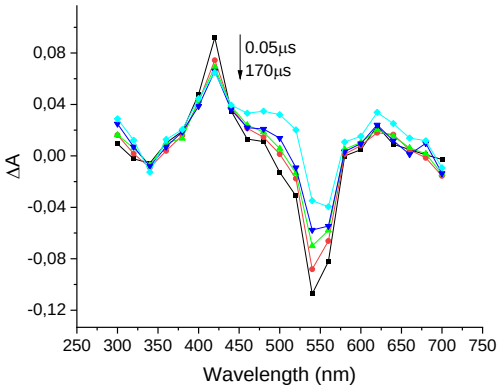

Figure 4. 15. Transient absorption spectra of RB^{2-} in the presence of 5 mM of DABCO in water at different time after the 532 nm laser pulse.

For further assignment, formation of $RB^{\bullet 3-}$ was forced by adding 1,4-diazabicyclo[2.2.2]octane (DABCO) to the system. Figure 4. 15 shows the transient absorption spectra of RB^{2-} in presence of 5 mM DABCO, where the $RB^{\bullet 3-}$ signal at 420 nm is clearly observed. Therefore, detection of this species when εdG and εdA are present in the solution, together with $^3RB^{2-*}$ quenching by these ε-adducts points toward a photoredox process where $^3RB^{2-*}$ oxidizes the lesions to yield the photosensitizer reduced form, $RB^{\bullet 3}$,

and the radical cation of the lesions. This latter was not detected in our experiment; however, it could be masked by the band derived from RB^{2-}, have a low molar absorption coefficient or absorb in a region different from the analysis window.

In addition, the triplet manifold of the donor, $E_T(^3RB^{2-*})$ of ca. 176 kJ mol^{-1}, has a lower energy than that of the acceptor, as the E_T of ε-adducts range from 278 to 314 kJ mol^{-1}. This allows discarding a triplet-triplet energy transfer (TTET) process as responsible for the quenching.

4.2.2.2. Photosensitization of ε-adducts by 4-carboxybenzophenone

4.2.2.2.1. Steady-state photolysis

As an alternative photosensitizer, 4-carboxybenzophenone (CBP) was considered. First of all, steady-state photolysis experiments were done in order to investigate the repair process.

The etheno adducts were irradiated with UVA light in the presence and absence of CBP in a deaerated mixture of water and acetonitrile (1:1, v:v). CBP was used to study pure Type I mechanisms or TTET; therefore, absence of O_2 is required. No degradation of the etheno derivatives occurred during the control irradiation in the absence of CBP. By contrast, in the presence of CBP, photodegradation took place for the three etheno derivatives (Figure 4. 16). In the case of εdC, a low yield of dC was obtained after its degradation, and no other compounds were detected under the experimental conditions (monitoring at λ=260 nm). For εdG and εdA, the repaired nucleoside was observed together with another peak at a t_R of ca. 10 min for εdG, as it has been mentioned above for RB^{2-} photosensitization, and t_R=4 min for εdA (Figure 4. 16). These results point toward the possibility of a photoinduced anaerobic oxidation process for the purine derivatives, which regenerates the original nucleobase from the ε-adducts.

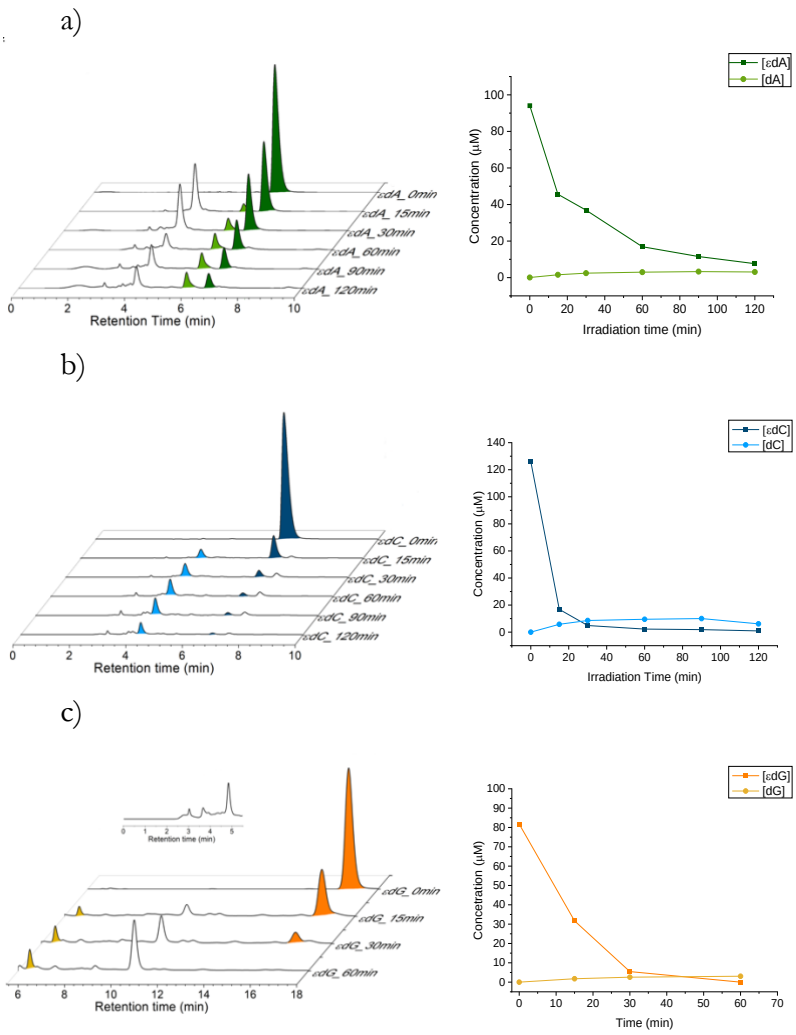

Figure 4. 16. HPLC chromatograms registered at 260 nm for an anaerobic solution of ε-adducts 100 μM in presence of CBP 50 μM upon UVA irradiation at different times in MeCN:H_2O (1:1, v:v). Right, variation of the concentration of damaged (square) and repaired nucleoside (circle) with irradiation time. a) εdA, b) εdC and c) εdG, inset: chromatogram at short retention times after 30 min of irradiation.

4.2.2.2.2. Laser flash photolysis

Then, LFP experiments were carried out at 355 nm to investigate the nature of the observed oxidative pathway. Figure 4. 17 shows the transient absorption spectra of an N_2 flushed H_2O:ACN CBP solution. The signal detected at 560 nm was assigned to the CBP triplet excited state (^{3}CBP*) by comparison with reported data. [12]

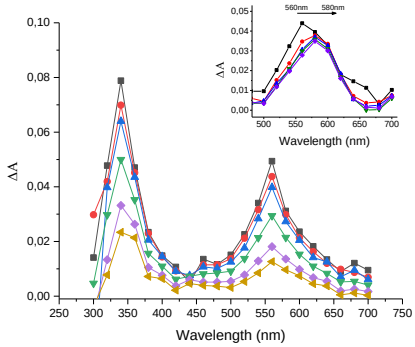

Figure 4. 17. CBP transient absorption spectra in MeCN:H_2O (1:1, v:v) at different times, from 0.1 to 8 μs, after the 355 nm laser pulse. Inset graph: CBP transient absorption spectra of the same solution adding 20% v:v of ethanol.

In the presence of purine-derived ε-adducts, the ^{3}CBP* disappeared at short delays after the laser pulse and gave rise to a long-lived and red shifted signal with maximum at ca. 580 nm (Figure 4. 18C). This process was more pronounced in the case of εdG than for εdA (Figure 4. 18A), and it was not observed for εdC. The new transient was attributed to the ketyl radical of CBP obtained from photoreduction of the ^{3}CBP* and oxidation of the lesions. In this process, the formed anion radical CBP$^{\bullet-}$ is subsequently protonated (Figure 4. 19) [19] yielding CBPH$^{\bullet}$.

a)

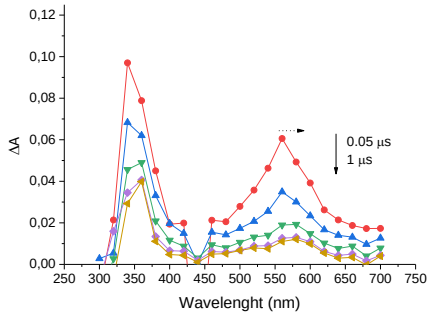

b)

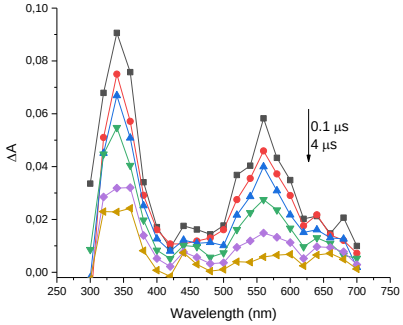

c)

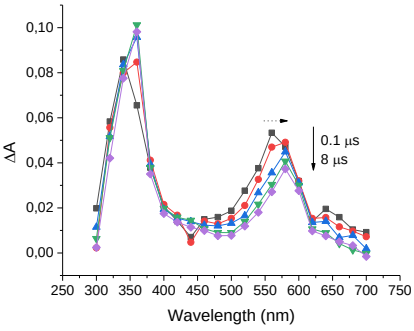

Figure 4. 18. Transient absorption spectra of CBP in presence of ε-adduct (2 mM for εdA and εdC, and 0.3 mM for εdG) in MeCN:H_2O (1:1, v:v) at different times after the 355nm laser pulse. a) εdA, b) εdC 0.5, c) εdG.

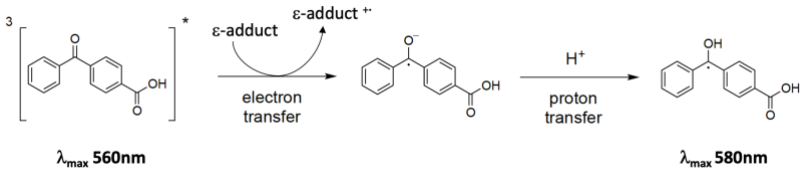

Figure 4. 19. Photooxidation mechanism triggered by 4-carboxybenzophenone leading to the formation of its anion radical (CBP$^{\bullet-}$) and subsequently to the ketyl radical (CBPH$^{\bullet}$).

This transient radical was further assigned by comparison with the signals obtained for CBP aqueous solution containing 20% of ethanol (inset Figure 4. 17). In this case, the typical H-abstraction from H donor solvent led to efficient formation of CBP ketyl radical centered at 580 nm.

Concerning the kinetics, the ^{3}CBP* lifetime was shortened in the presence of the three etheno derivatives. The bimolecular quenching rate constants $k_q(^3CBP^*)$-ε obtained from the Stern-Volmer plots were of ca. $3.6\cdot10^9$ $M^{-1}s^{-1}$ for εdG, $2.2\cdot10^9$ $M^{-1}s^{-1}$ for εdA and $2.7\cdot10^9$ $M^{-1}s^{-1}$ for εdC. Interestingly, the $k_q(^3CBP^*)$-ε was higher in the case of εdG, where TTET is energetically disfavored as $E_T(^3\varepsilon dG^*) > E_T(^3CBP^*)$. This is consistent with quenching occurring via electron transfer from the etheno to benzophenone triplet manifold and is further supported by the clear detection of CBPH$^{\bullet}$ in Figure 4. 18c.

By contrast, for εdA and εdC both TTET and photoredox processes should be considered. In the case of εdA, the ketyl radical is indeed observed albeit in lower yield (Figure 4. 18a). Hence, the high $k_q(^3CBP^*)$-ε of ca. $2.7\cdot10^9$ $M^{-1}s^{-1}$ found in this case should be the result of a combination of electron transfer and TTET.

Finally, CBPH$^{\bullet}$ is hardly detectable for quenching by εdC, pointing toward the predominance of an energy transfer quenching process.

4.3. DISCUSSION

In this chapter, the photoreactivity of ε-adducts triggered by two well-established photosensitizers has been addressed to get mechanistic insight into the processes responsible for their photodecomposition. In both cases, triplet-mediated processes were observed for the purine adducts.

Firstly, experimental results obtained during irradiation in the presence of RB^{2-} are not in agreement with a "clean" Type II photosensitization of ε-adducts since the photoreaction takes place to a similar extent in aerobic and anaerobic media. For that reason, competition between Type I and Type II oxidation was further investigated to establish the actual mechanism responsible for the ε-adducts photodegradation.

After RB^{2-} excitation, triplet excited state is efficiently populated (ϕ_{ISC}= 0.8) and then it can be deactivated following different pathways (Figure 4. 20): (i) intrinsic decay, $k_d(^3RB^{2-*})$, (ii) quenching by the ε-adducts, $k_q(^3RB^{2-*})$-ε, via a Type I process, or (iii) quenching by oxygen $k_q(^3RB^{2-*})$-O_2 to form $^1O_2$. This species can be subsequently quenched, $k_q(^1O_2)$-ε, by the ε-adduct to yield a Type II process or can decay naturally to its ground state, $k_d(^1O_2)$.

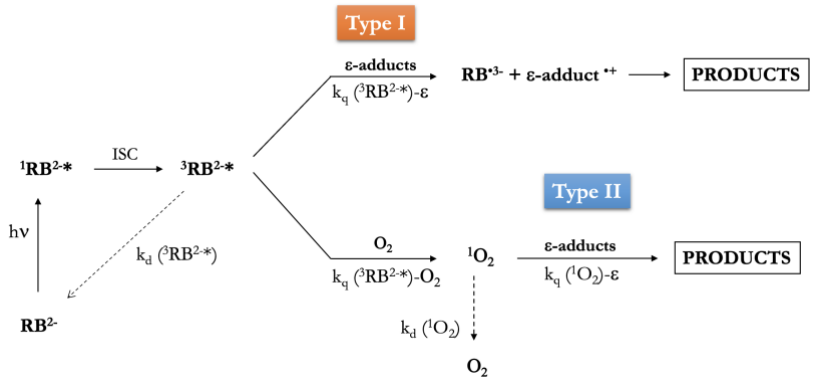

Figure 4. 20. Deactivation routes intervening in the interaction between excited RB^{2-} and ε-adducts.

The values of the bimolecular quenching rate constants are given in Table 4. 4 and Table 4. 5, the constants derived from the laser flash photolysis experiments were considered in the case of $^3RB^{2-*}$. This analysis has only been made for εdA and εdG, as no interaction between $^3RB^{2-*}$ and εdC was experimentally evidenced.

Contribution of the different routes and of the percentage of Type I vs Type II processes can be estimated by using equations (1 - 5). [20] In these equations, $\tau(^3RB^{2-*})$ and $\tau(^1O_2)$ are $^3RB^{2-*}$ and $^1O_2$ lifetimes of ca. 80 and 66 μs, respectively. Values of [ε-adduct]= $20\cdot10^{-6}$ M and $[O_2]$= $2.9\cdot10^{-4}$ M were considered for the concentrations of ε-adducts and molecular oxygen in water [21] respectively, and $k_q(^3RB^{2-*})$-O_2 is taken as $7.4\cdot10^9$ $M^{-1}s^{-1}$. [20]

Equations (1) to (3) allow determining the contribution of the three pathways arising from $^3RB^{2-*}$:

(eq. 1)

$$\%^3RB^{2-*}Intrinsicdecay(k_{d^3RB^{2-*}}) = \frac{\frac{1}{\tau_{3RB^{2-*}}}}{k_{q(^3RB^{2-*})-O_2}\cdot[O_2] + k_{q(^3RB^{2-*})-\varepsilon}\cdot[\varepsilon] + \frac{1}{\tau_{3RB^{2-*}}}} x100$$

Type I:

(eq. 2)

$$\%^3RB^{2-*}Quenching\_\varepsilon\left(k_{q(^3RB^{2-*})-\varepsilon}\right) = \frac{k_{q(^3RB^{2-*})-\varepsilon}\cdot[\varepsilon]}{k_{q(^3RB^{2-*})-O_2}\cdot[O_2] + k_{q(^3RB^{2-*})-\varepsilon}\cdot[\varepsilon] + \frac{1}{\tau_{3RB^{2-*}}}} x100$$

(eq. 3)

$$\%^1O_2\ Formation\left(k_{q(^3RB^{-2*})-O_2}\right) = \frac{k_{q(^3RB^{2-*})-O_2}\cdot[O_2]}{k_{q(^3RB^{2-*})-O_2}\cdot[O_2] + k_{q(^3RB^{2-*})-\varepsilon}\cdot[\varepsilon] + \frac{1}{\tau_{3RB^{2-*}}}} x\ 100$$

Next, quenching of $^3RB^{2-*}$ by molecular oxygen can produce $^1O_2$, which could evolve through two further pathways: intrinsic decay (eq. 4) or quenching by the ε-adduct (at the origin of Type II process, eq. 5). Therefore, considering that $^3RB^{2-*}$ quenching by O_2 only results in $^1O_2$ formation, eq. (3), the percentages of these two routes are given by eqs. (4) and (5):

(eq. 4)

$$\%^1O_2\ Intrinsic\_decay\ (kq^1O_2) = \frac{k_{q(^3RB^{2-*})-O_2}\cdot[O_2]}{k_{q(^3RB^{2-*})-O_2}\cdot[O_2] + k_{q(^3RB^{2-*})-\varepsilon}\cdot[\varepsilon] + \frac{1}{\tau_{3RB^{2-*}}}} x \frac{\frac{1}{\tau^1O_2}}{k_{q(^1O_2)-\varepsilon}\cdot[\varepsilon] + \frac{1}{\tau^1O_2}} X\ 100$$

Type II:

(eq. 5)

$$\%^1O_2\ Quenching\_by\_\varepsilon\ (kq(^1O_2)-\varepsilon) = \frac{k_{q(^3RB^{2-*})-O_2}\cdot[O_2]}{k_{q(^3RB^{2-*})-O_2}\cdot[O_2] + k_{q(^3RB^{2-*})-\varepsilon}\cdot[\varepsilon] + \frac{1}{\tau_{3RB^{2-*}}}} x \frac{k_{q(^1O_2)-\varepsilon}\cdot[\varepsilon]}{k_{q(^1O_2)-\varepsilon}\cdot[\varepsilon] + \frac{1}{\tau^1O_2}} X\ 100$$

The contributions of the different pathways for εdA and εdG photosensitization by RB^{2-} are summarized in Table 4. 6.

Table 4. 6. Estimated contributions of the different routes involved in εdA and εdG photosensitization by RB^{2-}.

Q	**%$^3RB^{2-*}$ intrinsic decay** (Eq 1)	**%$^3RB^{2-*}$ quenching by ε-adducts** (Eq. 2)	**%$^3RB^{2-*}$ quenching by O_2** (Eq 3)	**%$^1O_2$ intrinsic decay** (Eq 4)	**% $^1O_2$ quenching by ε-adducts** (Eq 5)
εdA	0.6	$3\cdot10^{-3}$	99.4	99.3	0.1
εdG	0.6	0.08	99.3	98.9	0.5

It is clearly observed that the main deactivation pathway of $^3RB^{2-*}$ under aerobic conditions consists in quenching by oxygen, leading mainly to $^1O_2$ formation (eq. 3), which accounts for 99.4% and 99.3% for εdA and εdG, respectively.

Nevertheless, subsequent quenching of $^1O_2$ by the lesions occurs with relatively low bimolecular rate constants, $k_q(^1O_2)$-ε of ca. $9.5\cdot10^5$, $3.6\cdot10^6$ $M^{-1}s^{-1}$ for εdA and εdG, respectively. Thus, at the lesion concentration of 20 μM, almost all the $^1O_2$ decays without reacting (%$^1O_2$ intrinsic decay eq. 4, Table 4. 6). Nevertheless, under

aerobic conditions, the contribution of a Type II process is higher than that of the Type I pathway.

This conclusion can be directly drawn for εdG, as it has been previously established that this lesion is able to react with $^1O_2$, cleanly generated from thermal degradation of naphthalene-derived endoperoxides, to regenerate the original dG. [9]

However, in the present work, no clear conclusion on the reactivity between $^1O_2$ and the two other ε-adducts can be made. Indeed, no chemical changes have been observed by Di Mascio *et al.*,[9] after thermal activation of an endoperoxide. This points toward a physical, rather than chemical, deactivation of $^1O_2$ by εdA and εdC, and opens the door to the involvement of Type I reactivity, as that observed during the anaerobic experiments.

Such process is conceivable in the case of the purine adducts, for which bimolecular quenching rate constants of $^3RB^{2-*}$ by the lesions are $k_q(^3RB^{2-*})$-ε of $3.8\cdot10^6$ and $8.5\cdot10^7$ $M^{-1}s^{-1}$, for εdA and εdG (Table 4. 5), respectively. Conversely, it seems quite unlikely for εdC as no interaction was observed during the phosphorescence or transient absorption measurements. Hence, for this lesion, an alternative mechanism involving other reactive species derived from RB^{2-} excitation might be involved.

To further investigate the Type I route not involving oxygen, experiments were run under anaerobic conditions using CBP as photosensitizer. In this case, two main processes might occur: an electron transfer from the ε-adduct to ^{3}CBP* or a TTET from the photosensitizer triplet manifold to the lesion.

Interestingly, in spite of exhibiting similar ^{3}CBP* quenching rate constants ranging from 3.6 to $2.2\cdot10^9$ $M^{-1}s^{-1}$, the three adducts display a different reactivity associated with their triplet excited state energy and reduction potential in the excited state. For εdG, a clear electron transfer was evidenced by the formation of CBPH$^\bullet$ (Figure 4. 18c). Although the reduction potential value for εdG has not been reported, it appears from our experiments that, like the corresponding canonical nucleobase dG, it might be the most easily oxidized ε-adduct. This assumption is not only based on CBPH$^\bullet$

detection, but also on the fact that the highest quenching rate constant for $^3RB^{2-}$*, $k_q(^3RB^{2-}*)$-ε = $8.5 \cdot 10^7$ $M^{-1}s^{-1}$, was determined for this lesion (Table 4. 5), for which TTET is energetically disfavored as E_T(CBP) < E_T(εdG) (Table 4. *2*).

In the case of εdA, a low amount of CBPH$^{\bullet}$ was formed (Figure 4. 18a). Indeed, the low E_T of the lesion opens the door to the TTET process, and thus, energy and electron transfer might compete and result in an overall $k_q(^3RB^{2-}*)$-ε of ca. $2.2 \cdot 10^9$ $M^{-1}s^{-1}$.

Finally, for εdC TTET is the most efficient route, CBP ketyl radical is hardly detectable from the transient absorption spectra (Figure 4. 18b); and no significant repair is observed by HPLC (Figure 4. 16).

On the basis of these results, mechanisms could be proposed for Type I and Type II photosensitization of ε-adducts (Figure 4. 21). Electron transfer from εdG to $^3RB^{2-}$* could result in the formation of cation radical **I** centered on the etheno ring, which after nucleophilic addition of water and deprotonation yields radical **II**. This radical can further react with water to yield glycol intermediate **III**, or disproportionate and after addition of water can also give rise to **III**. Then, dG is formed after attack of water and loss of formic acid. A similar mechanism is proposed for dA formation from εdA. In the case of $^1O_2$-mediated process, its addition on the εdG double bond of the etheno ring leads, as proposed by Di Mascio et al. [9], to an unstable dioxetane **IV** that cleaves to form intermediates **III** or **V**. For intermediate **III**, the following reaction steps are then similar to those described for Type I. For intermediate **V**, compounds **VIa** or **VIb** are formed after attack of water, and loss of formic acid; these intermediates after a second addition of water and elimination of a second molecule of formic acid lead to the regenerated base dG.

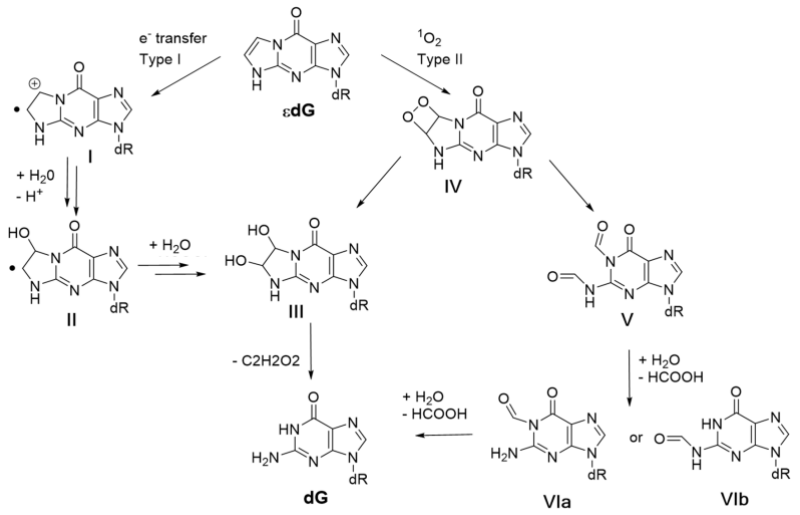

Figure 4. 21. Proposed mechanism for Type I and Type II photosensitized degradation of εdG.

4.4. CONCLUSIONS

As a global outcome, the studies run in this Chapter have revealed the photolability of ε-adducts under photosensitization. The use of photosensitizers acting by Type I and/or Type II mechanisms has shown that (i) εdG is sensitive to both types of processes, (ii) εdA is decomposed mainly under an electron transfer mechanism, (iii) εdC photosensitization might be the result of non-identified reactive species generated under RB^{2-} excitation. Interestingly, the obtained photoproducts correspond to the repaired nucleosides. Photosensitization might, thus, be proposed as a new strategy of photorepair for this type of lesions.

4.5. EXPERIMETAL SECTION

All the techniques are described in the instrumentation section, Chapter 6.

4.5.1. Synthesis

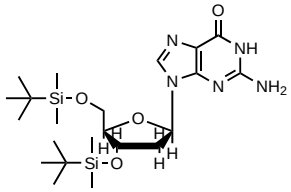

1

3',5'-O-bis(*tert*-butyldimethylsilyl)-2'-deoxyguanosine (1). Compound 1 was prepared using guanosine (8 g, 30 mmol), which was dissolved in anhydrous DMF (100 mL) under N_2 flow. Then the reaction mixture was placed in an ice bath and *tert*-butyldimethylsilyl chloride (TBDMSCl) (2 equivalents, 9 g, 59.8 mmol) and imidazole (4 g, 59.8 mmol) were added, the reaction was left 10 minutes more with the ice bath. Then, the mixture was stirred overnight at room temperature under nitrogen atmosphere. Finally, the reaction was quenched with 100 mL of water, the precipitate was filtered, washed with water and dried under vacuum obtaining 1 as a white solid (11.9 g, 80%). **^{1}H NMR (300 MHz, DMSO-d6)** δ 10.45 (s, 1H), 7.73 (s, 1H), 6.31 (s, 2H), 5.97 (m, 1H), 4.35 (m, 1H), 3.74 – 3.66 (m, 1H), 3.64 – 3.48 (m, 2H), 2.6 – 2.10 (m, 2H), 0.78 – 0.71 (s+s, 18H), -0.09 (s+s, 12H). **^{13}C NMR (75 MHz, DMSO-d6)** δ 156.6, 153.6, 150.9, 134.8, 116.6, 86.9, 82.1, 72.1, 62.7, 25.7, 25.6, 17.8, 17.6, -4.8, -5.0, -5.5, -5.6.

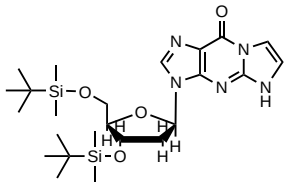

2

3',5'-O-bis(*tert*-butyldimethylsilyl)-1,N^2-Etheno-2'-deoxyguanosine (2). To a solution of 3',5'-O-bis(*tert*-butyldimethylsilyl)-2'-deoxyguanosine (1) (4 g, 8.1 mmol) in DMF (40 mL) was added K_2CO_3 (1.45 g, 10.5 mmol), and the mixture was stirred at room temperature for 10 min. Then, chloroacetaldehyde solution (50 wt % in H_2O, 1.43 mL, 11.3 mmol) was added dropwise, and the mixture was heated at 35ºC under nitrogen.

Progress of the reaction was monitored using UV spectra. The reaction was stopped when the same absorption was reached at 272 and 254 nm. After 16 hours, the reaction was quenched with 100 mL of water, the precipitate was filtered, washed with water and dried under vacuum. The resulting yellow solid was purified by column chromatography on silica gel (CH_2Cl_2:AcEtO, 1:1 to 1:3) to afford 2 as a white solid (1 g, 25%). **^{1}H NMR (300 MHz, Chloroform-d)** δ 8.42 (s, 1H), 7.61 (d, J = 2.5 Hz, 1H), 7.35 (d, J = 2.5 Hz, 1H), 6.38 (m, 1H), 4.60 (m, 1H), 4.10 (m, 1H), 3.86 – 3.73 (m, 2H), 2.55 (s, 2H), 0.98 – 0.79 (m, 18H), 0.18 – 0.00 (m, 12H). **^{13}C NMR (75 MHz, Chloroform-d)** δ 150.9, 149, 146.3, 136.1, 116.6, 107.6, 88.7, 84.8, 72.5, 63.2, 41.1, 26.1, 25.9, 18.5, 18.2, -4.4, -4.6, -5.2, -5.3.

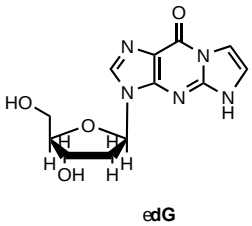

εdG

1,N^2-Etheno-2'-deoxyguanosine (εdG). To a solution of 3',5'-O-bis(*tert*-butyldimethylsilyl)-1,N^2-etheno-2'-deoxyguanosine (2) (400 mg, 0.77 mmol) in pyridine (4 mL) with ice cooling was added a solution of HF/pyridine (70%, 456 mL) in a plastic tube. The ice bath was withdrawn, and the mixture was stirred at room temperature for 2 h. The solution was neutralized with 2 g of $NaHCO_3$, filtered and the solvent was removed by air stream. The residue was then purified by column chromatography on silica gel (CH_2Cl_2:MeOH, 19:1 to 5:1) to afford εdG as a white solid (63.7 mg, 29%). **^{1}H NMR (300 MHz, DMSO-d6)** δ 8.13 (s, 1H), 7.60 (d, J = 2.7 Hz, 1H), 7.42 (d, J = 2.7 Hz, 1H), 6.26 (dd, J = 7.6, 6.0 Hz, 1H), 5.38 – 5.26 (m, 1H), 4.99 (m, 1H), 4.43 – 4.32 (m, 1H), 3.84 (m, 1H), 3.55 (m, 2H), 2.67 – 2.54 (m, 1H), 2.32 – 2.19 (m, 1H). **^{13}C NMR (75 MHz, DMSO-d6)** δ 151.3, 149.9, 145.9, 136.9, 116.6, 115.3, 106.8, 87.6, 82.9, 70.7, 61.6. **HRMS (ESI)**: calc for $C_{12}H_{13}N_5O_4$ $[M+H]^+$ 292.0968, found 292.1041.

4.5.2. NMR Spectra

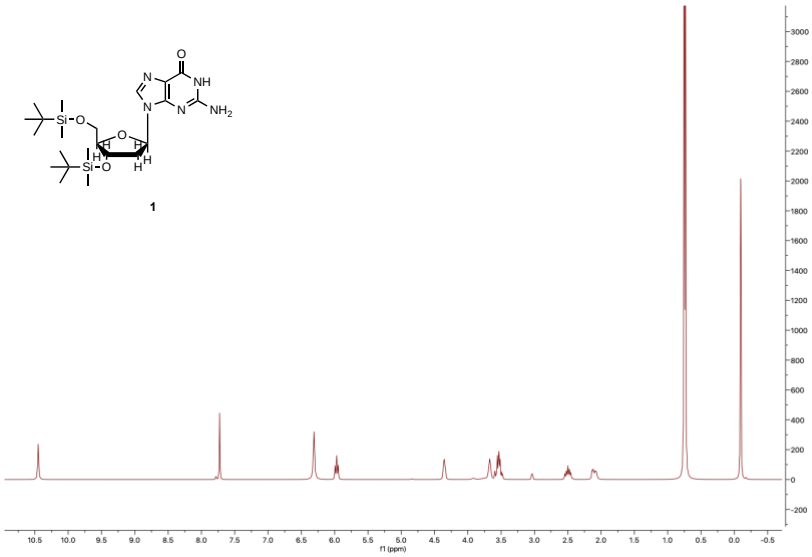

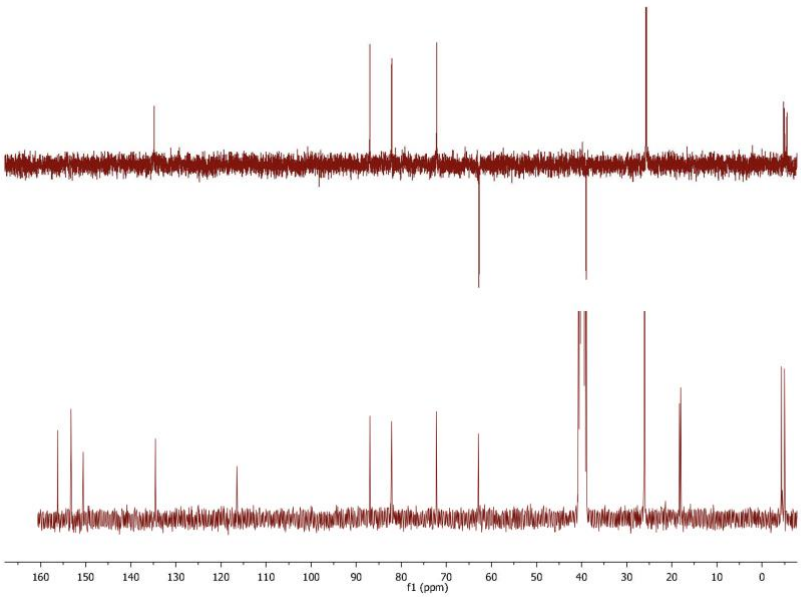

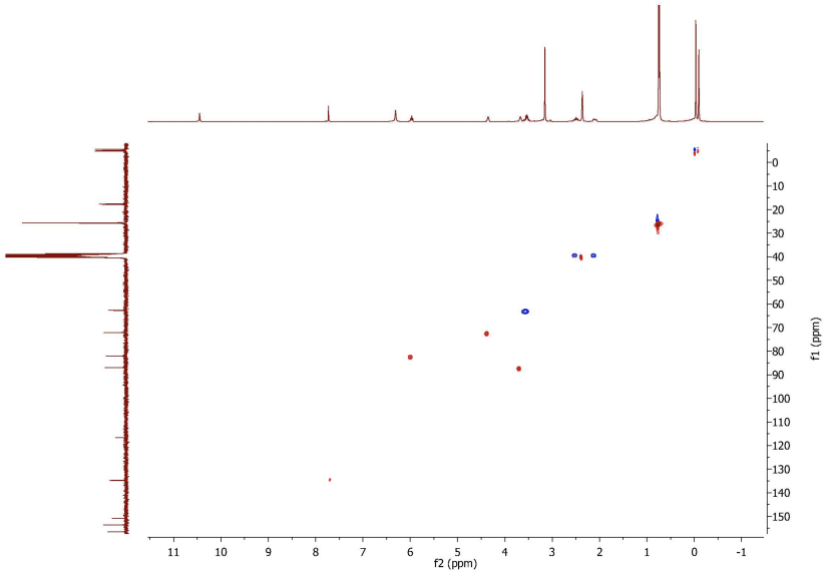
f2 (ppm)
f1 (ppm)

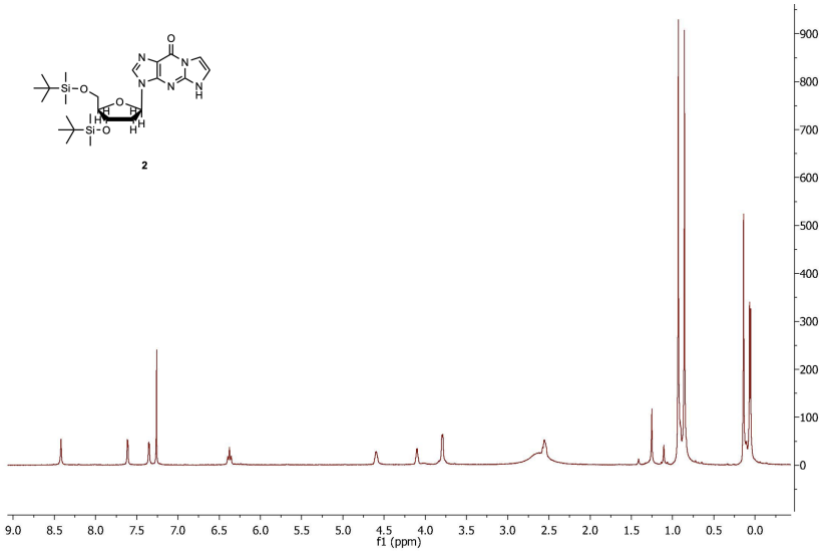
2
f1 (ppm)

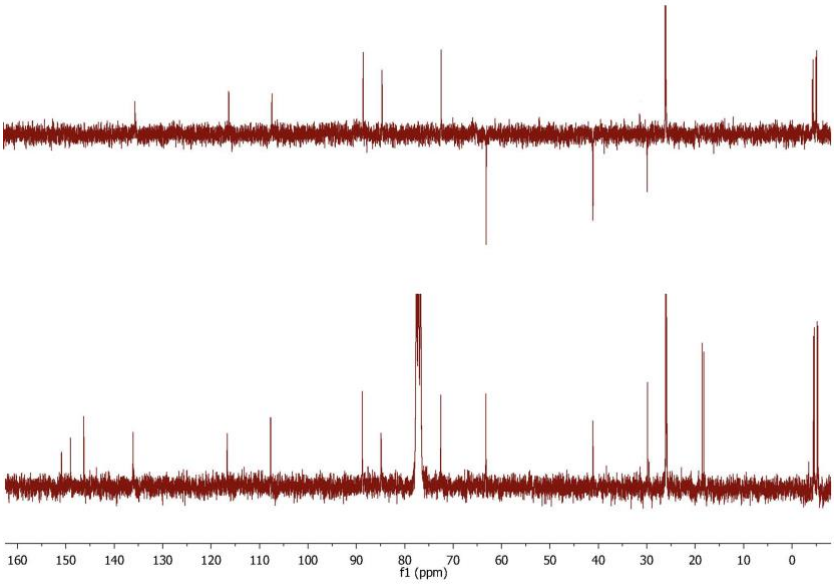
160
150
140
130
120
110
100
90
80
70
60
50
40
30
20
10
0
f1 (ppm)

3

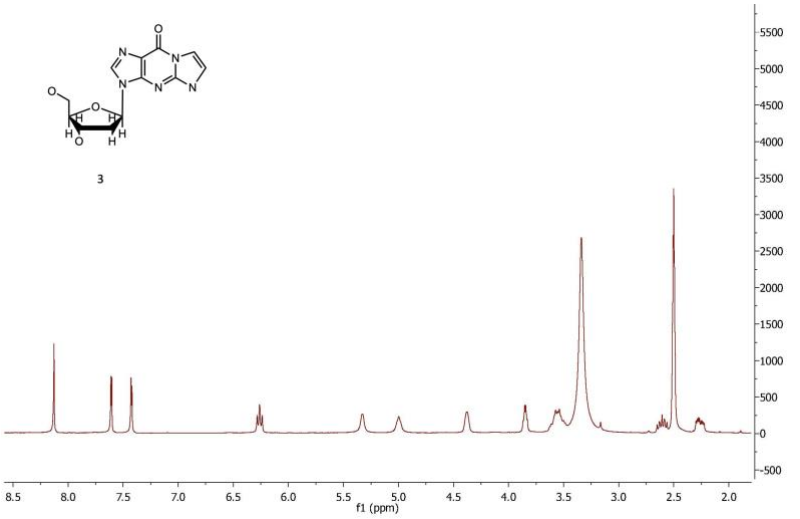
5500
5000
4500
4000
3500
3000
2500
2000
1500
1000
500
0
-500
8.5
8.0
7.5
7.0
6.5
6.0
5.5
5.0
4.5
4.0
3.5
3.0
2.5
2.0
f1 (ppm)

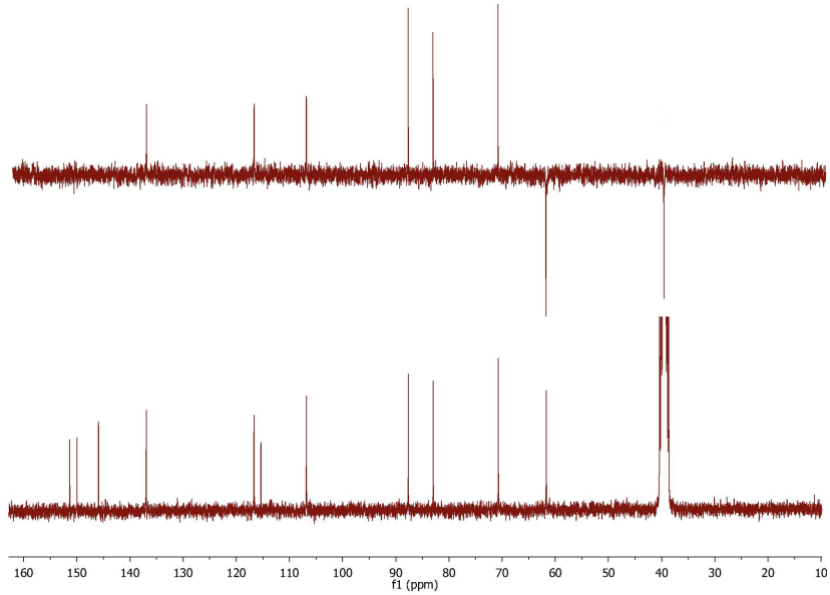
160 150 140 130 120 110 100 90 80 70 60 50 40 30 20 10
f1 (ppm)

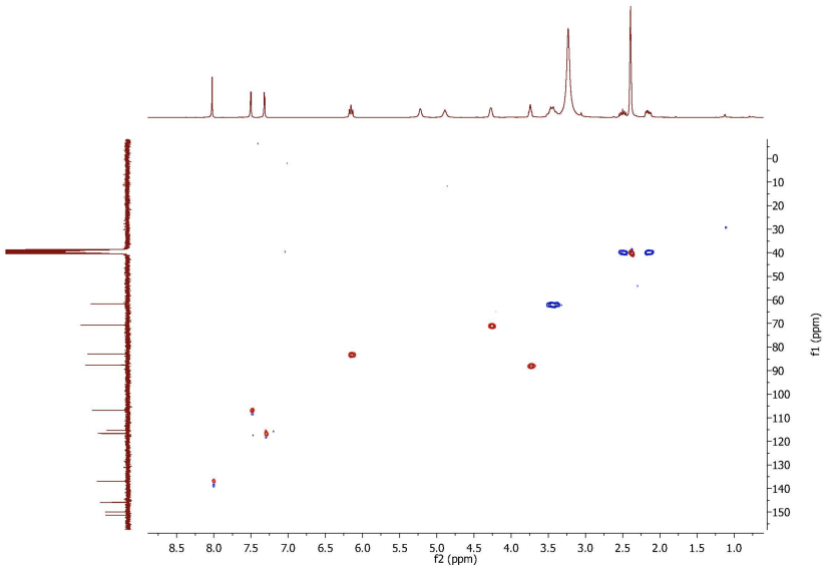
8.5 8.0 7.5 7.0 6.5 6.0 5.5 5.0 4.5 4.0 3.5 3.0 2.5 2.0 1.5 1.0
f2 (ppm)
0 10 20 30 40 50 60 70 80 90 100 110 120 130 140 150
f1 (ppm)

4.6. REFERENCES

(1) DNA Photodamage. From Light Absorption to Cellular Response and Skin Cancer.; Improta, R., Douki, T., *Eds.; Royal Society of Chemistry*, **2021**.

(2) Baptista, M. S.; Cadet, J.; Di Mascio, P.; Ghogare, A. A.; Greer, A.; Hamblin, M. R.; Lorente, C.; Nunez, S. C.; Ribeiro, M. S.; Thomas, A. H.; Vignoni, M.; Yoshimura, T. M. Type I and Type II Photosensitized Oxidation Reactions: Guidelines and Mechanistic Pathways. *Photochem. Photobiol.* **2017**, *93* (4), 912–919.

(3) Cadet, J.; Douki, T.; Ravanat, J. L. Oxidatively Generated Damage to the Guanine Moiety of DNA: Mechanistic Aspects and Formation in Cells. *Acc. Chem. Res.* **2008**, *41* (8), 1075–1083.

(4) Ravanat, J. L.; Saint-Pierre, C.; Cadet, J. One-Electron Oxidation of the Guanine Moiety of 2'-Deoxyguanosine: Influence of 8-Oxo-7,8-Dihydro-2'-Deoxyguanosine. *J. Am. Chem. Soc.* **2003**, *125* (8), 2030–2031.

(5) Cui, L.; Ye, W.; Prestwich, E. G.; Wishnok, J. S.; Taghizadeh, K.; Dedon, P. C.; Tannenbaum, S. R. Comparative Analysis of Four Oxidized Guanine Lesions from Reactions of DNA with Peroxynitrite, Singlet Oxygen, and γ-Radiation. *Chem. Res. Toxicol.* **2013**, *26* (2), 195–202.

(6) Kino, K.; Takao, M.; Miyazawa, H.; Hanaoka, F. A DNA Oligomer Containing 2,2,4-Triamino-5(2H)-Oxazolone Is Incised by Human NEIL1 and NTH1. *Mutat. Res. Mol. Mech. Mutagen.* **2012**, *734* (1–2), 73–77.

(7) Hori, M.; Suzuki, T.; Minakawa, N.; Matsuda, A.; Harashima, H.; Kamiya, H. Mutagenicity of Secondary Oxidation Products of 8-Oxo-7,8-Dihydro-2'-Deoxyguanosine 5'-Triphosphate (8-Hydroxy-2'- Deoxyguanosine 5'-Triphosphate). *Mutat. Res. Mol. Mech. Mutagen.* **2011**, *714* (1–2), 11–16.

(8) Barbati, S.; Bonnefoy, A.; Botta, A.; Chiron, S. Secondary Oxidation of Cyclic 1,N2-Propano and 1,N2-Etheno-2'-Deoxyguanosine DNA Adducts. Consequences in Oxidative Stress Biomarker Development. *Chemosphere* **2010**, *80* (9), 1081–1087.

(9) Martinez, G. R.; Brum, H.; Sassaki, G. L.; De Souza, L. M.; Loureiro, A. P. D. M.; De Medeiros, M. H. G.; Di Mascio, P. Oxidation of 1-N 2 -Etheno-2'-Deoxyguanosine by Singlet Molecular Oxygen Results in 2'-Deoxyguanosine: A Pathway to Remove Exocyclic DNA Damage? *Biol. Chem.* **2018**, *399* (8), 859–867.

(10) Ludvíková, L.; Friš, P.; Heger, D.; Šebej, P.; Wirz, J.; Klán, P. Photochemistry of Rose Bengal in Water and Acetonitrile: A Comprehensive Kinetic Analysis. *Phys. Chem. Chem. Phys.* **2016**, *18* (24), 16266–16273.

(11) Lambert, C. R.; Kochevar, I. E. Electron Transfer Quenching of the Rose Bengal Triplet State. *Photochem. Photobiol.* **1997**, *66* (1), 15–25.

(12) Cuquerella, M. C.; Lhiaubet-Vallet, V.; Cadet, J.; Miranda, M. A. Benzophenone Photosensitized DNA Damage. *Acc. Chem. Res.* **2012**, *45* (9), 1558–1570.

(13) Onidas, D.; Markovitsi, D.; Marguet, S.; Sharonov, A.; Gustavsson, T. Fluorescence Properties of DNA Nucleosides and Nucleotides: A Refined Steady-State and Femtosecond Investigation. *J. Phys. Chem. B* **2002**, *106* (43), 11367–11374.

(14) Cuquerella, M.C.; Lhiaubet-Vallet, V.; Bosca, F.; Miranda, M. A. Photosensitised Pyrimidine Dimerisation in DNA. *Chem. Sci.* **2011**, *2* (7), 1219–1232.

(15) Ravanat, J. L.; Dumont, E. Reactivity of Singlet Oxygen with DNA, an Update. *Photochem. Photobiol.* **2022**, *98* (3), 564–571.

(16) Marin, M. L.; Santos-Juanes, L.; Arques, A.; Amat, A. M.;

Miranda, M. A. Organic Photocatalysts for the Oxidation of Pollutants and Model Compounds. *Chem. Rev.* **2012**, *112* (3), 1710–1750.

(17) Lambert, C. R.; Kochevar, I. E. Does Rose Bengal Triplet Generate Superoxide Anion? *J. Am. Chem. Soc.* **1996**, *118* (13), 3297–3298.

(18) Islam, S. D. M.; Ito, O. Solvent Effects on Rates of Photochemical Reactions of Rose Bengal Triplet State Studied by Nanosecond Laser Photolysis. *J. Photochem. Photobiol. A Chem.* **1999**, *123* (1–3), 53–59.

(19) Lineros-Rosa, M.; Miranda, M. A.; Lhiaubet-Vallet, V. A Sunscreen-Based Photocage for Carbonyl Groups. *Chem. – A Eur. J.* **2020**, *26* (32), 7205–7211.

(20) Martinez-Haya, R.; Miranda, M. A.; Marin, M. L. Type I vs Type II Photodegradation of Pollutants. *Catal. Today* **2018**, *313*, 161–166.

(21) Montalti, M.; Credi, A.; Prodi, L.; Gandolfi, M. T. Handbook of Photochemistry, third edit.; *Taylor & Francis Group*, **2006**.

CHAPTER 5

ROSE BENGAL DECORATED HYBRID METAL NANOPARTICLES FOR THE PHOTOREPAIR OF ETHENO ADDUCTS

5.1. INTRODUCTION

The burden of cancer incidence and mortality is rapidly growing worldwide. The International Agency for Research on Cancer (IARC) estimated 19.3 million new cases and 10 million cancer deaths in 2020. [1] Therefore, researchers are devoting endless efforts to develop effective therapies for this disease. Conventional cancer treatments mainly include surgery, chemotherapy and radiotherapy; but, new alternatives are constantly coming to light offering safer, more effective and more affordable solutions. In this context, photodynamic therapy (PDT) combining the action of a photosensitizing drug, light and molecular oxygen is gaining ground [2,3] and is now used in the treatment of several cancers, such as skin cancer, head and neck cancers, superficial bladder cancer, esophagus, lung etc. Indeed, PDT provides numerous advantages as (*i*) it is a non-invasive, or minimally invasive treatment, (*ii*) it has no long-term side effects, (*iii*) it is most often an outpatient procedure, (*iv*) it affords a precise targeting of the treated area, (*v*) it produces little or no scarring after the site heals. [4]

Moreover, PDT has a wider application scope than cancer therapy and encompasses treatment of skin conditions such as psoriasis or the inactivation of microbial organism, also known as photodynamic inactivation (PDI).

In recent years, nanotechnology-based PDT has allowed achieving great progresses by offering solutions to the challenging issues of drug administration (drug hydrophobicity, poor stability, low cell or tissue specificity) that limit their clinical applications. Functionalization of nanoparticles by the drug/photosensitizer (Phs) has been shown to improve their targeting, specificity, and efficacy for tumors. [2,3,5,6] A large number of nanoparticle types have been reported, they include polymeric nanocarriers, micelles, nanotubes, dendrimers, magnetic nanoparticles, silica-based nanomaterials, core-shell nanoparticles, solid lipid nanoparticles, quantum dots (QDs) and so on. [5,7]

Core-shell structured nanoparticles are of interest because they integrate the functionalities of individual components (drug,

hydrophilic and/or targeting ligand, etc.) [8] into one structure and exhibit improved physical and chemical properties that differs from their single components. The shell is generally composed of silica oxide (SiO_2), which is widely used in bioapplications [9] due to its low cytotoxicity, good biodegradability and easy derivatization of its surface. This latter confers to these NPs multiple utilities encompassing targeted distribution through functionalization with antibodies [6], sensing [10] or controlled release of drugs. [11]

For the core component, metal-derived nanoparticles, especially gold and silver NPs, have attracted the attention due to their strong interaction with light, which generates localized surface plasmon resonance (LSPR). [12]

Indeed, under irradiation the conduction electrons of noble-metal nanoparticles can be driven by the incident electric field in collective oscillations known as LSPR (Figure 5. 1). This produces a net charge difference at the nanoparticle boundaries, which leads to the generation of strong electromagnetic fields at the metal surface at the origin of a wide variety of optical phenomena. [12]

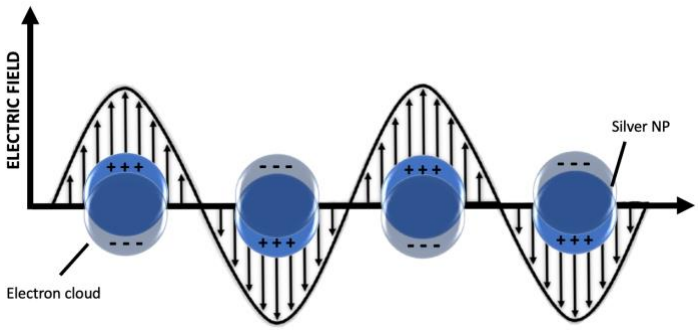

Figure 5. 1. Graphical representation of the localized surface plasmon resonance (LSPR) effect on silver nanospheres upon irradiation at their resonant wavelength.

Depending on their composition, morphology and size, the nanoparticles resonate at different wavelengths. Under irradiation at those specific wavelengths, the noble-metal NPs can absorbed/scattered a fraction of the incoming electromagnetic wave, which is spread in the far field, but it also locally enhances the

electric field in the near field at the NP surface. [13] This latter is effective within tens of nanometers from the NP's surface.

The combined near and far field effects of the metal NPs, also called nanoantennas, have led to their application in numerous fields, such as surface enhanced fluorescence (SEF), Förster resonance energy transfer, surface-enhanced Raman scattering (SERS) spectroscopy, plasmonic solar cells, sensing, nanomedicine, to name a few. [12]

Among the amplified effects produced by metal NPs, the possibility of enhancing singlet oxygen ($^1O_2$) formation has been a driving force for improving applications involving this ROS. The changes in $^1O_2$ production depend on several parameters, including the metal NP shape, size, and composition, together with the Phs−metal separation distance and spectral overlap. [14–16] In this context, it has been recently demonstrated that $^1O_2$ enhancement depends on both the near- and far-field properties of the NPs. [15] The former interactions can modulate the Phs photophysical properties by increasing its absorption, intersystem crossing yield, and energy transfer to molecular oxygen, whereas the re-emitted photons in the far field by scattering effects can boost the quantity of photons available for the Phs to absorb. [15] Concerning the Phs-metal separation, it has been shown that the perfect shell thickness is typically of ca. 10-20 nm [17] and, an optimal enhancement factor, EF_Δ, for $^1O_2$ formation was determined for Ag, Au and their 1:1 alloy NP coated with 10 nm thickness shell. [15,16]

Plasmonic NPs functionalized with $^1O_2$ Phs have been proposed to increase the therapeutic efficiency of PDT. [18,19] However, up to now no reports exist on their use to prevent cancer appearance by repairing the DNA sequence. In this Chapter, Rose Bengal-decorated silica coated metal nanoparticle (Figure 5. 2) are considered to boost the photosensitizing activity of the dye described in Chapter 4, with the final aim of achieving an efficient photorepair of the etheno adducts.

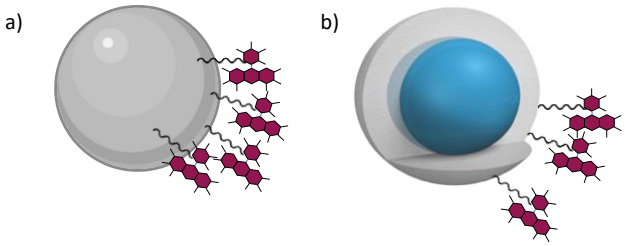

Figure 5. 2. a) SiO_2 NP functionalize with Rose Bengal (SiO_2-RB) and b) Ag@SiO_2-RB NP, blue core of Ag and SiO_2 shell in gray, couple with RB.

5.2. RESULTS AND DISCUSSION

5.2.1. Nanoparticle characterization

5.2.1.1. SiO_2-RB

Silica nanoparticles (SiO_2 NP) with the same shape and similar size that those of plasmonic NPs were used as a reference rather than the free RB^{2-} in solution (Figure 5.2a). This way, the SiO_2 NP´s geometry provides the same chemical environment for the Phs and background scattering as in the corresponding Ag@SiO_2-RB NPs. In addition, it has been previously reported that RB conjugated to SiO_2 NPs does not exhibit the same $^1O_2$ quantum yield as the dye free in solution, and a decrease of 20% was indeed determined with a ϕ_Δ value of ca. 0.6. [20]

The SiO_2 NP were obtained following the Stöber protocol using tetraethyl orthosilicate (TEOS) and ammonium hydroxide solution (NH_4OH). Spherical SiO_2 NPs with a diameter of 115±8 nm were obtained, as evaluated from the Transmission Electron Microscopy (TEM) images (Figure 5. 3). NPs were further aminated with (3-aminopropyl)triethoxysilane (APTES) prior to functionalization with RB^{2-} through the formation of an amide bond formed via carbodiimide chemistry using *N*-(3-dimethylaminopropyl)-*N*-ethylcarbodiimide hydrochloride (EDC). The detailed procedures are given in the experimental section of this chapter.

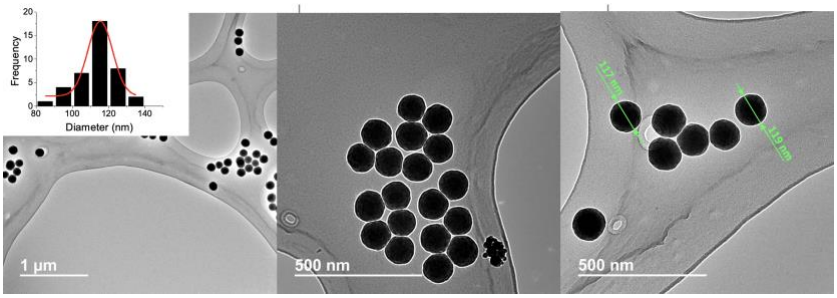

Figure 5. 3. TEM images of SiO_2 NP at different magnitude and spot. Inset: Size distribution histogram.

Throughout the synthesis, the size and surface charge (Zeta-potential, ζp) of the NPs were recorded using dynamic light scattering technology (DLS, Figure 5. 4) to confirm the surface modification at the different steps, *ie.* amination (SiO_2-NH_2) and conjugation (SiO_2-RB).

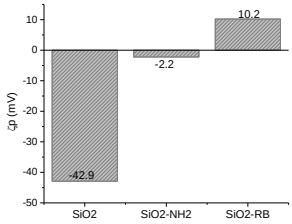

Figure 5. 4. NP Zeta-potential at the different steps of the synthesis in H_2O at pH 5 and pH 3 for SiO_2-RB.

In water, a ζp value of -42.9 mV was determined for a disperse solution of SiO_2 NPs, this negative values is due to the presence of the silanol groups on the NP surface. [21] It becomes less negative (ζp= -2.2 mV) after the amination step because of the presence of protonated amino groups at pH 5. Finally, after the last step of RB^{2-} conjugation, ζp of Ag@SiO_2-RB is positive at pH 3 where the dye is in its semi-protonate structure (pK_a~ 3.7). [22] The final hydrodynamic size of the NPs was of *ca.* 390 nm.

The amount of RB^{2-} attached onto SiO_2 NP surface was calculated by subtracting the concentration of the unreacted RB^{2-}

left in each supernatant after centrifugation during the washing step to the initial one added in the conjugation step (see experimental section). Finally, the RB^{2-} concentration was determined to be *ca.* 0.12 mM. Moreover, inductively coupled plasma mass spectrometry (ICP-MS) analysis of the same sample allows determining a concentration of 6 mM for SiO_2. Therefore, the suspended SiO_2-RB NP solution contained 0.12 mM of RB^{2-} anchored to 6 mM of SiO_2 (ie. 0.02 mM for 1 mM SiO_2).

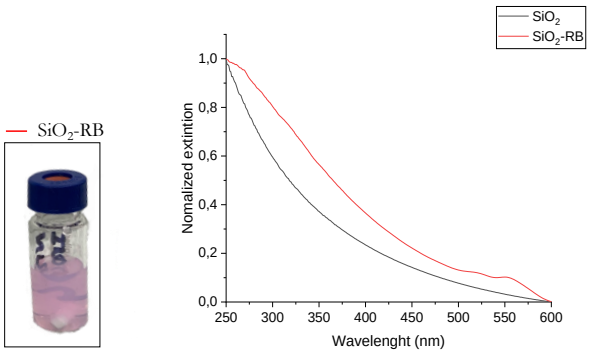

Figure 5. 5. Left: Picture of SiO_2-RB suspensions in water. Right: normalized UV-Vis spectra of SiO_2 NP and RB^{2-} conjugated SiO_2 NP.

After functionalization with RB^{2-}, the nanoparticle suspension becomes pink (Figure 5. 5 left). This colour change is in accordance with the absorption spectrum, which shows the NP scattering along with the expected RB^{2-} absorption signature centred around 550 nm (Figure 5. 5 right, red trace).

5.2.1.2. Ag@SiO_2-RB

Next, silver core nanoparticles covered with silica (Ag@SiO_2 NP) were synthesized following the protocol described in the experimental section. Briefly, in a first step, Ag NPs were obtained by a seeded growth approach using gold (Au) seeds leading to spherically and crystalline Ag NP with 47±6 nm size (Figure 5. 6). In addition, the typical narrow plasmon band with an extinction maximum at 420 nm was observed by UV-Vis spectrophotometry (Figure 5. 9, black line). These nanoparticles were coated with a 14 nm-thick layer of SiO_2 following the Stöber protocol as used for the SiO_2 NP synthesis. The size of the layer was selected on the basis

of previous works, [16,23] which established that 10-20 nm is the optimum shell distance between the metallic core and the Phs to maximize the plasmon-enhanced $^1O_2$ production.

The thickness of the shell (14 nm) was confirmed by TEM (Figure 5. 7). The obtained images gave also access to the volume distribution between Ag and SiO_2, being 46% of the total NP size formed by Ag while the remaining 54% correspond to the SiO_2 shell.

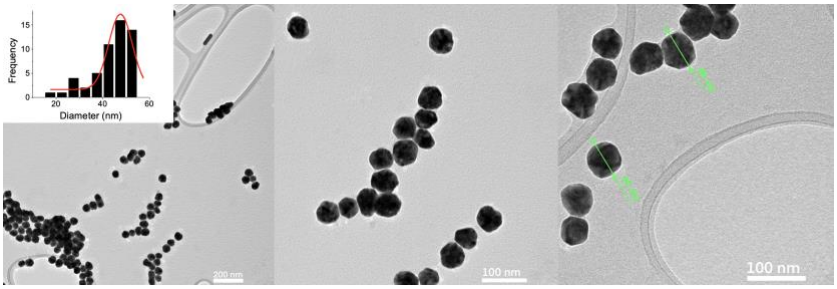

Figure 5. 6. TEM images of Ag NP at different magnitude and spot. Inset: Size distribution histogram.

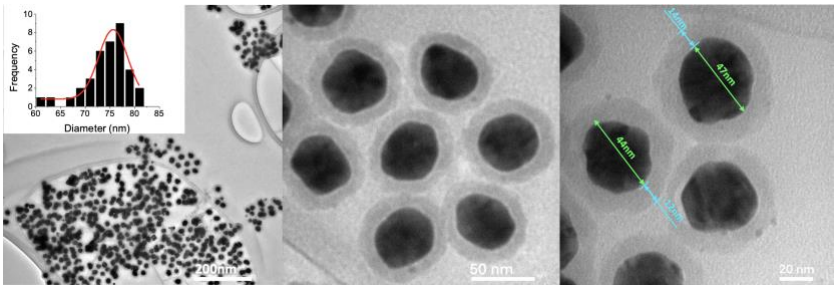

Figure 5. 7. TEM images of Ag@SiO_2 NP at different magnitude and spot. Inset: Size distribution histogram.

In terms of dynamic diffusion, the hydrodynamic size of the Ag and Ag@SiO_2 NP were of ca. 133 and 380 nm, respectively. It is worth mentioning that both NPs, SiO_2 and Ag@SiO_2, have a similar hydrodynamic size. This is an important point as this parameter is related to how NPs interact between each other and to their diffusion in the media.

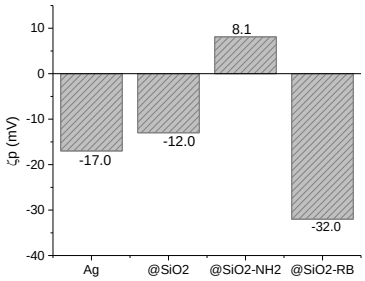

Figure 5. 8. NP Zeta-potential at the different steps of the Ag@SiO_2-RB synthesis in H_2O at pH 5.

As in the case of SiO_2 NPs, Zeta-potential was used to confirm the different surface modifications (Figure 5. 8). The surface of Ag NPs is negatively charged, this feature remains after SiO_2 coating and result in negative ζp values. Then, a positive value of 8.1 mV is measured after the amination step due to the protonated amino groups. Finally, after RB^{2-} conjugation, the negative ζp of *ca.* 32.0 mV is associated with the presence of the dye under its deprotonated form at pH 5. The large Δζp between these steps indicates a high functionalization of the NH_2 groups, and consequently a high concentration of RB^{2-} on the NP shell. This is also evidenced by UV-Vis absorption (Figure 5. 9, blue line) where the RB^{2-} band at ca. 555 nm is higher in intensity than the metal NP band at 420 nm.

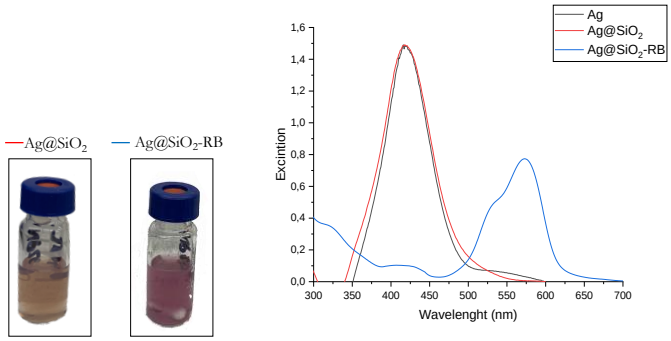

Figure 5. 9. *Left:* picture of Ag@SiO_2 (red line) Ag@SiO_2-RB (blue line) suspensions in water. *Right:* UV-Vis spectra of the different synthesis stages of Ag@SiO_2 NP and RB^{2-} conjugated to the Ag@SiO_2 NP.

The dye quantity attached onto $Ag@SiO_2$ surface was determined as described in the experimental section, a high RB^{2-} amount of ca. 2.5 mM in 1 mM of SiO_2 shell was calculated. Moreover, a concentration ratio 3:1 ($Ag:SiO_2$) was obtained for the core@shell NPs by ICP-MS analysis. Therefore, the concentration of RB^{2-} attached onto $Ag@SiO_2$ NPs surface is two orders of magnitude higher than that linked to SiO_2 NP. The steady-state photolysis experiments were performed diluting the $Ag@SiO_2$-RB suspension until reaching the same RB^{2-} concentration than that of the SiO_2-RB NPs, without taking into account the final number of nanoparticles.

5.2.2. Steady-state photolysis

The previous chapter reported on the RB^{2-} induced photolability of etheno adducts through Type I and Type II processes. But interestingly, the photoreaction is not deleterious but leads to a repair process of the lesion restoring the original nucleobases. Thus, steady-state photolysis studies using Rose Bengal supported on metal NPs were carried out to study ε-adduct repair and evaluate the effect of plasmon resonance. The enhancement of excited state RB^{2-} population and the subsequent $^1O_2$ production were evaluated by comparison with the results obtained using non plasmonic SiO_2-RB. For this purpose, both degassed and aerated irradiations were performed following the same methodology than that described in the Chapter 4.

5.2.2.1. SiO_2-RB nanoparticles

First, irradiations using SiO_2-RB NPs were run as reference experiments to quantify the ε-adducts photorepair by RB^{2-} supported on non plasmonic NPs.

The same conditions as those used in solution (see Chapter 4) were applied. The SiO_2-RB NPs were suspended in deuterated water to reach a final RB^{2-} concentration of 10 μM and a 2:1 ratio between the lesion and RB^{2-} was used (ε-adduct concentration of 20 μM). The solutions were irradiated under white light, λ_{exc} between 350 and 700 nm, using a Luzchem photoreactor equipped with eight fluorescent tubes of (FSL-T5 8W/765).Finally, samples were taken

at different irradiation times and analyzed by HPLC coupled to a UV-Vis detector to follow the photoreaction kinetics.

a)

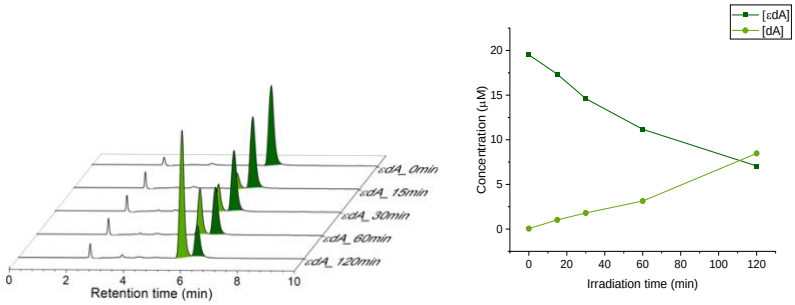

b)

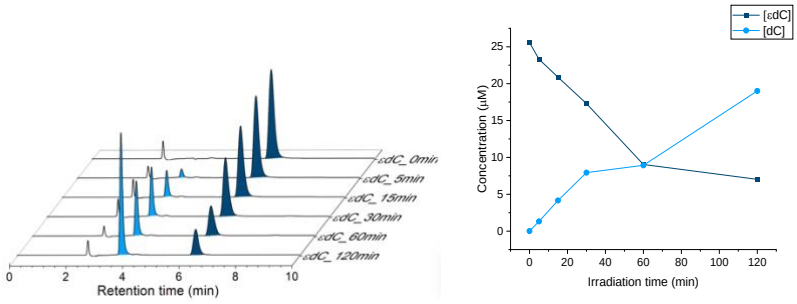

c)

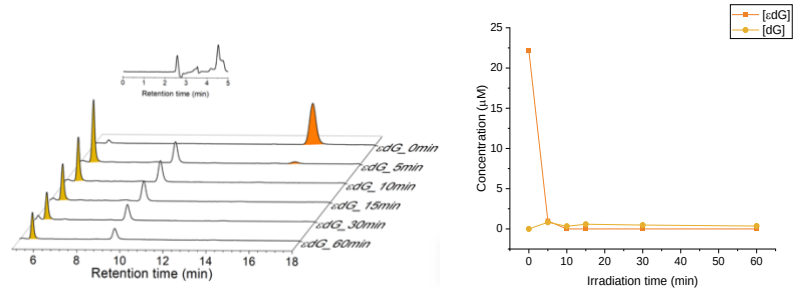

Figure 5. 10. Left, HPLC chromatograms registered at 260 nm for an aerated solution in D_2O of 20 μM ε-adduct and SiO_2-RB NP containing 10 μM RB after different irradiation times. Right, variation of the concentration of damaged (square) and repaired nucleoside (circle) as a function of the irradiation time. a)εdA, b)εdC and c)εdG, inset: chromatogram at short retention times after 60 min of irradiation.

As described in the previous chapter, the ε-adducts and their corresponding nucleobases were assigned and quantified using authentic samples. Retention times are t_R= 6.0 min for εdA, t_R=6.2 min for εdC, t_R=15 min for εdG, t_R= 5.6 min for dA and dG, and t_R= 4.0 min for dC. As shown in Figure 5. 10 and Figure 5. ***11***, during irradiation the ε-adduct peaks are decreasing concomitantly with the appearance of a new peak, which has the same elution time than that of the original nucleobase.

Steady-state photolysis experiments under aerobic conditions reveal the occurrence of a clean photoprocess for εdC and εdA, as shown in the chromatograms of Figure 5. 10. Only one photoproduct, absorbing at the monitoring wavelength λ=260 nm, was detected and it corresponds the repaired nucleobase. However, for εdG several peaks appeared before 5 min together with an intermediate at 9.2 min. Peak at t_R 2.5 min comes from the dG oxidation and intermediate at t_R 9.2 min can correspond to a possible intermediate of εdG photodegradation as explained in Chapter 4.

The repair efficiency differs depending on the ε-adduct. Indeed, it reaches a 42% yield after two hours of irradiation in the case of εdA, whereas 76% were obtained for εdC (Table 5. 1). For εdG, only 4% of the repaired dG is quantified after 5 min, but then the yield starts to decrease. This fast kinetics followed by the disappearance of the repaired nucleobase can be interpreted in terms of the high reactivity toward ROS of dG as already mentioned in Chapter 4.

A similar trend is observed in the case of anaerobic photolysis (Figure 5. 11), reaching repair yields of 45% and 60% for εdA and εdC, respectively (Table 5. 1).

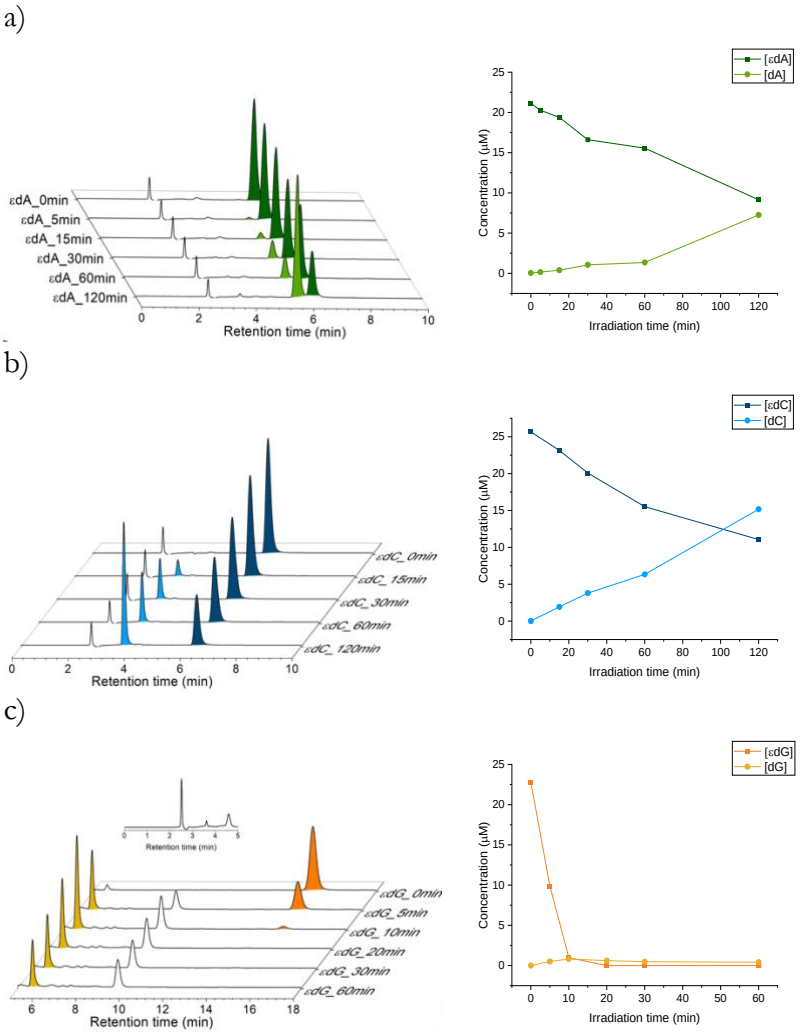

Figure 5. 11. Left, HPLC chromatograms registered at 260 nm for a degassed solution in D_2O of 20 μM ε-adducts and SiO_2-RB NP suspension containing 10 μM RB after different irradiation times. Right, variation of the concentration of damaged (square) and repaired nucleoside (circle) with irradiation time. a) εdA, b) εdC and c) εdG, inset: chromatogram at short retention times after 60 min of irradiation.

Table 5. 1. Yields of the nucleoside formation for anaerobic and aerobic photolysis of the ε-adducts irradiated in presence of both types of NP.

	AEROBIC		ANAEROBIC	
	SiO_2-RB	Ag@SiO_2-RB	SiO_2-RB	Ag@SiO_2-RB
εdA[a]	42%	40%	45%	50%
εdC[a]	76%	88%	60%	92%
εdG[b]	4%	5%	4%	5%

[a] 2h of irradiation.
[b] 5 min of irradiation.

5.2.2.1. Ag@SiO_2-RB nanoparticles

Next, the photolysis experiments were carried out with Ag@SiO_2 nanoparticles. First, control experiments were performed under aerobic conditions by irradiating the lesion in presence of Ag@SiO_2 NP (Figure 5. 12) to discard the role of non functionalized NPs as photosensitizers. The NP solution was prepared to be isoabsorptive with that containing RB^{2-} with an OD of ca. 0.4 at its maximum (ie. 420 nm) as set for the photolysis studies.

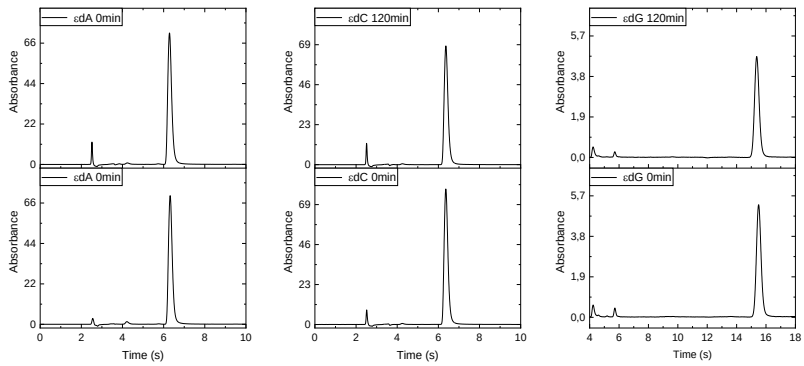

Figure 5. 12. HPLC chromatograms registered at 260 nm obtained after 0 and 120 min of white light irradiation of a solution of 20 μM of etheno adduct and Ag@SiO with an OD_{max}(Ag@SiO_2NP)=0.4 in deuterated water .

No changes in the peak area were observed by HPLC showing that the etheno adducts are stable when irradiated with white light in the presence of the naked NPs (Figure 5. 12). Contrarily, steady-state photolysis of the ε-adducts in the presence of Ag@SiO_2-RB

NPs showed the consumption of the lesions under both anaerobic and aerobic conditions (Figure 5. 13Figure 5. 14).

a)

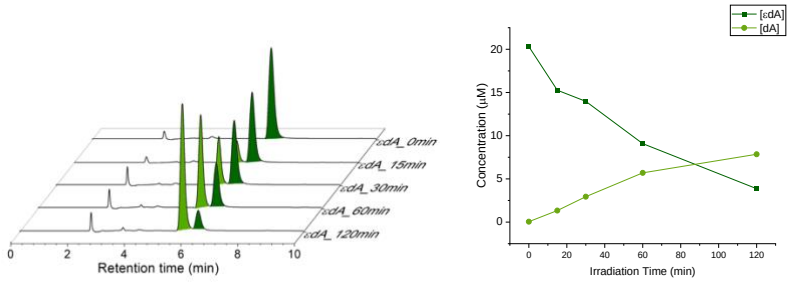

b)

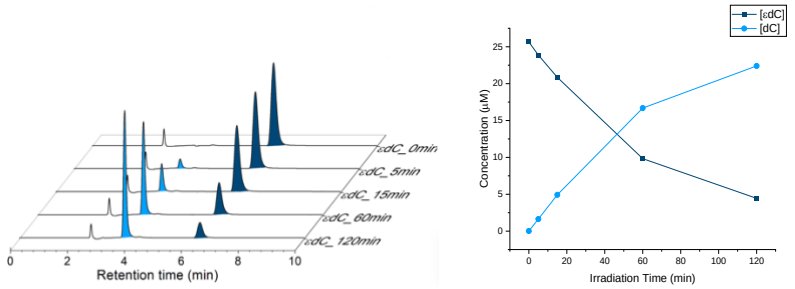

c)

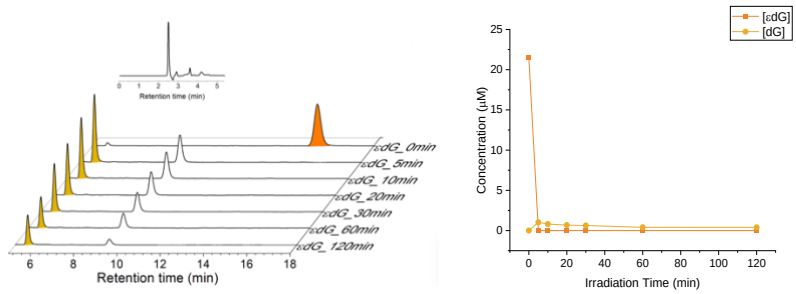

Figure 5. 13. Left, HPLC chromatograms registered at 260 nm for an aerated solution in in D_2O of 20 μM ε-adduct in presence of Ag@SiO_2-RB NP suspension containing 10 μM RB at different irradiation times. Right, variation of the concentration of damaged (square) and repaired nucleoside (circle) as a function of the irradiation time. a)εdA, b)εdC and c)εdG, inset: chromatogram at short retention times after 120 min of irradiation.

Similar trends as for SiO_2-RB experiments were observed after HPLC analysis giving rise to the formation of the same

photoproducts. Interestingly, kinetics for formation of the repaired nucleobases are faster for these metallic nanoparticles than in the case SiO_2-RB NPs, and higher yields were also obtained in the case of εdC.

a)

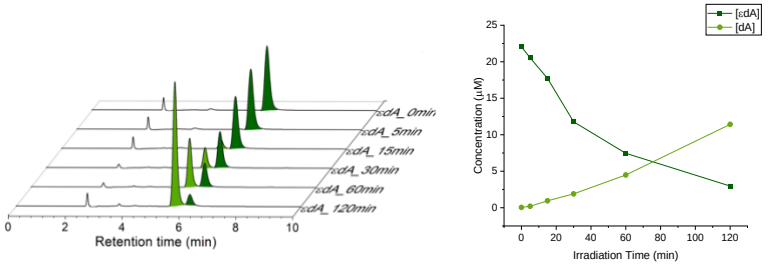

b)

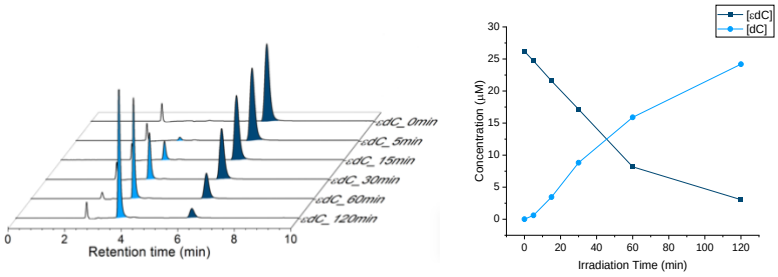

c)

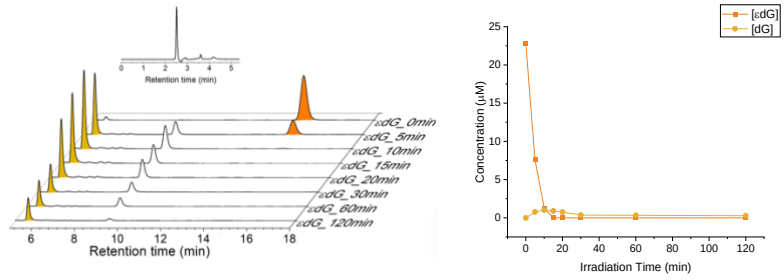

Figure 5. 14. Left, HPLC chromatograms registered at 260 nm for a degassed solution in D_2O of 20 μM ε-adducts in presence of a Ag@SiO_2-RB NP suspension that contains 10 μM RB at irradiation different times. Right, variation of the concentration of damaged (square) and repaired nucleoside (circle) with irradiation time. a) εdA, b) εdC and c) εdG, inset: chromatogram at short retention times after 120 min of irradiation.

Under aerobic conditions, recovery of the nucleosides appears to occur in similar, somewhat lower, yields than in anaerobiosis: after 2h of irradiation yields of 40% for dA and 88% for dC were determined (Figure 5. 13a,b), while in degassed solutions the repaired nucleosides are formed in a 50% for dA and 92% for dC (Figure 5. 14a,b , Table 5. 1).

As already observed, εdG is the ε-adducts that is decomposed the fastest but leads to low yields of dG, being of only 4% after 10 min in presence of air and after 5 min under deaerated conditions (Figure 5.13c and 5.14c). Indeed, the high reactivity of this purine base toward oxidation, both through Type I or Type II processes, opens the door to secondary reactions.

5.3. CONCLUSIONS

In this chapter, two types of nanoparticles have been synthesized and compared to evaluate the plasmonic effect on the ε-adduct repair. For this purpose, metal core@shell NPs of Ag@SiO_2 were considered. A thickness of ca. 14 nm between the metal core and the shell surface decorated with the Phs was achieved to get an optimal plasmon-enhanced effect as previously reported in the literature. Successful Rose Bengal loading was accomplished onto the surface of both NPs, obtaining a high coupling yield for Ag@SiO_2 NPs.

Steady-state photolysis studies undergone with SiO_2-RB and Ag@SiO_2-RB NPs as photoactive materials revealed higher final yields of the original base recovery in the case of εdC for the plasmonic NPs. Interestingly, as observed in Chapter 4, the reaction tends to be more effective under anaerobic conditions pointing towards the involvement of other reactive species than singlet oxygen.

Up to now, only the bipirymidine DNA lesions, ie. the cyclobutane pyrimidine dimers and the 6-4PPs, are known to be photochemically repaired by photolyases. In this study, we show that photosensitization of other damages belonging to the ε-adduct family also yields to the recovery of the original nucleobase. These

results can pave the way to the design of artificial enzymes, new (photo)nanozymes, mimicking the AlkB activity. For this purpose, the next step is to evaluate the repair process in more complex systems such as short oligonucleotides containing the etheno lesion to evaluate the ability of Ag@SiO_2-RB NP to regenerate the original sequence and its interaction with the canonical bases.

5.4. EXPERIMENTAL

5.4.1. Synthesis SiO_2-RB NPs

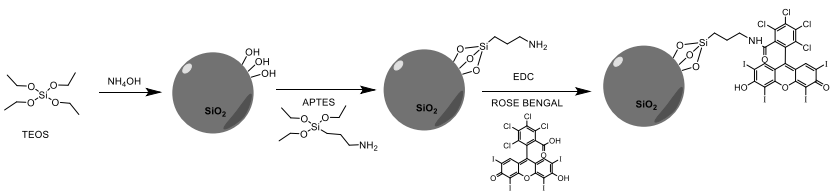

Silica nanoparticles functionalized with the photosensitizer Rose Bengal (SiO_2-RB) were synthesized as a reference nanoparticle for the plasmon-enhancement studies allowing comparison of their repair ability with that of the metal NPs.

First, 115 nm SiO_2 nanoparticles were synthesized using the Stöber protocol. [24,25] Briefly, 40 mL of absolute ethanol were poured in a round-bottom flask under stirring. Then, 1.6 mL from a solution of 0.18 M tetraethyl orthosilicate (TEOS) and 3 mL of NH_4OH (30% w/v) were added to the flask and stirred overnight. SiO_2 NPs were centrifuged (5000 rpm, 30 min) and resuspended in EtOH 3 times before being stored at 4 °C.

Finally, to get the desired repair system SiO_2-RB NPs were aminated and conjugated with RB^{2-} proceeding as described in sections 5.4.3 and 5.4.4.

5.4.2. Synthesis Ag@SiO_2-RB

5.4.2.1. Synthesis of gold seeds

The synthesis of Ag NPs was performed using the seeded growth protocol synthesis of spherical silver nanoparticles. [17]

First, Au seeds are used as a nucleation core for the silver nanoparticles (Ag NPs). The seeds were synthesized by adding 10 μL of 0.25M solution $HAuCl_4$ to a glass vial containing 10 mL of PVP-10,000 (2.5% wt in H_2O). Then, 600 μL of $NaBH_4$ from a 0.1 M aqueous solution was added very quickly. After stirring for 15 min, the solution color changed from dark orange to dark red. Finally, the seeds were kept at 4 °C for 18h before use.

5.4.2.2. Synthesis of Ag NPs

Once the Au seeds were ready to use the Ag NPs growth solution was prepared. First, 40 mL of PVP-10,000 (2.5% wt/wt in H_2O), 10 mL of acetonitrile, 2 mL of a 0.1 M ascorbic acid aqueous solution and 1.2 mL of a 0.1 M $AgNO_3$ aqueous solution are mixed in a round-bottom flask at room temperature and stirred at 700 rpm. Then, 6 μL of Au seeds were added to the growth solution. The reaction was left at room temperature and stirred for 15 min. The Ag NPs were purified by centrifugation (three cycles of 1h, 5000 rpm) and dispersed in 50 mL of H_2O.

5.4.2.3. Silica coating of silver nanoparticles

Stöber protocol was also used for the silica-coating of the Ag NPs. 25 mL of purified Ag NPs (OD_{max} = 0.5) were poured into an erlenmeyer with 100 mL of absolute ethanol and stirred at 700 rpm. Then, 2 mL of NH_4OH (30% w/v) were added, and immediately, the addition of 10 mL freshly prepared TEOS solution (33.5 μL TEOS in 15 mL ethanol) was started by using a syringe pump (Cole-Parmer 74900-00 series) working at an addition rate of 3 mL/hour. When the TEOS addition ended, the reaction mixture was stirred at room temperature for 2 hours.

Finally, the NPs were purified by three cycles of centrifugation (60 min, 4000 rpm). The supernatants were discarded, and the $Ag@SiO_2$ NPs pellet was dispersed in 25 mL of ethanol and stored at 4 °C until further use.

5.4.3. Amination step

In both types of nanoparticles, SiO_2 and $Ag@SiO_2$, (3-aminopropyl)triethoxysilane (APTES) was used as a linker between the NP and the photosensitizer. 300μL of APTES and 60 μL of NH_4OH were added to a suspension of 10 mL of NP with an OD_{440}=0.5 in a crystal vial, and the reaction mixture was stirred at room temperature overnight.

The next day, the reaction was centrifuged four times (30 min, 5000 rpm), first with ethanol, next, two times with H_2O and finally with MES buffer (pH 6). After the purification, the NPs were used straightaway in the next step.

5.4.4. RB^{2-} conjugation step

Finally, the RB^{2-} was conjugated using a carbodiimide crosslinker, N-(3-dimethylaminopropyl)-*N*'-ethylcarbodiimide hydrochloride (EDC), adapting the synthesis from previous works.[17]

First, 48 mg of EDC and 102 mg of RB^{2-} were dissolved in 6 mL of MES buffer (pH 6) in a crystal vial protected from light with an aluminum foil and stirred for 1 h. During this time, the NPs were centrifuged to remove the supernatant, leaving the pellets in the tube.

After 1h, the EDC/RB^{2-} mixture was poured into the falcon tube containing the NPs pellet, which were resuspended. Then, the reaction, protected from the light, was stirred for 24 h at room temperature. For the first 3 hours, the falcon tube was sonicated every 30 min to ensure a good dispersion of the NPs.

To finish, the RB-conjugated nanoparticles (NPs-RB) were collected by centrifugation (30 min, 5000 rpm) and washed; two times with H_2O, then five times with EtOH and finally two more times with H_2O.

The UV-visible spectrum of each supernatant was recorded between each centrifugation to determine the final amount of unconjugated RB^{2-}. The NPs-RB pellets were finally stored in the dark at 4 °C in deuterated water (D_2O).

5.4.5. Determination of the conjugated RB^{2-} concentration

The concentration of RB^{2-} bound onto the NPs surface was obtained through the difference between the sum of the RB^{2-} quantities determined from UV-visible spectrum of each supernatant and the initial RB^{2-} amount (0.1 mmol). The concentration of RB^{2-} in the supernatants was quantified using the Beer-Lambert law measuring the absorbance at the maximum absorption wavelength of RB^{2-} (550 nm and 557 nm in H_2O and EtOH, respectively) and using the molar absorption coefficient $\varepsilon_{550}(H_2O)= 95000\ M^{-1}cm^{-1}$ and $\varepsilon_{557}(EtOH)= 104700\ M^{-1}cm^{-1}$. [26]

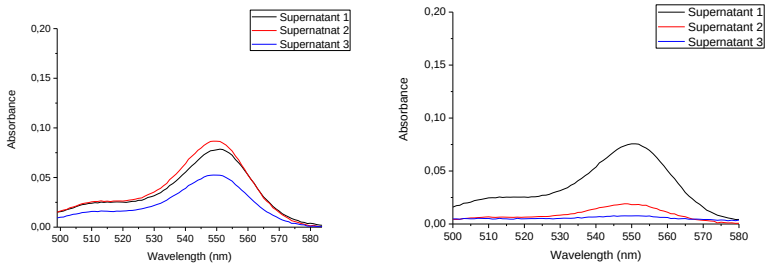

Figure 5. 15. UV-Vis spectra of some supernatants for SiO_2 NP (left) and $Ag@SiO_2$ NP (right) during the centrifugation steps.

Table 5. 2. RB^{2-} conjugated and removed quantities obtained through centrifugation washes.

	RB^{2-}_i (mmol)	RB^{2-} removed (mmol)	$[RB^{2-}]_{NP}$ mM
SiO_2-RB	0.1	0.0992	0.12
$Ag@SiO_2$-RB	0.1	0.0375	2.5

RB^{2-}_i, is the number of moles of RB added in the conjugation step.
RB^{2-} removed, is the total number of moles in the supernatant after washing.
$[RB^{2-}]_{NP}$, is the concentration of RB (in molarity) in the solution of nanoparticles after extract the RB^{2-} removed to the RB^{2-}_i.

5.5. REFERENCES

(1) Sung, H.; Ferlay, J.; Siegel, R. L.; Laversanne, M.; Soerjomataram, I.; Jemal, A.; Bray, F. Global Cancer Statistics 2020: GLOBOCAN Estimates of Incidence and Mortality Worldwide for 36 Cancers in 185 Countries. *CA. Cancer J. Clin.* **2021**, *71* (3), 209–249.

(2) Photodynamic Therapy: Methods and Protocols; Broekgaarden, M.; Zhang, H.; Mladen, K.; Hamblin, M. R.; Heger, M., Ed.; *Human Press*, **2022**.

(3) Photodynamic Medicine: From Bench to Clinic; Kostron, H., Hasan, T., Eds.; *The Royal Society of Chemistry*, **2016**.

(4) Photodynamic Therapy https://www.cancer.org/treatment/treatments-and-side-effects/treatment-types/radiation/photodynamic-therapy.html (accessed Aug 8, 2022).

(5) Chen, J.; Fan, T.; Xie, Z.; Zeng, Q.; Xue, P.; Zheng, T.; Chen, Y.; Luo, X.; Zhang, H. Advances in Nanomaterials for Photodynamic Therapy Applications: Status and Challenges. *Biomaterials* **2020**, *237*, 119827.

(6) Nanomedicines: Design, Delivery and Detection; Braddock, M., Ed.; *The Royal Society of Chemistry*, **2016**.

(7) Yang, Y.; Zeng, Z.; Almatrafi, E.; Huang, D.; Zhang, C.; Xiong, W.; Cheng, M.; Zhou, C.; Wang, W.; Song, B.; Tang, X.; Zeng, G.; Xiao, R.; Li, Z. Core-Shell Structured Nanoparticles for Photodynamic Therapy-Based Cancer Treatment and Related Imaging. *Coord. Chem. Rev.* **2022**, *458*, 214427.

(8) Chatterjee, K.; Sarkar, S.; Jagajjanani Rao, K.; Paria, S. Core/Shell Nanoparticles in Biomedical Applications. *Adv. Colloid Interface Sci.* **2014**, *209*, 8–39.

(9) Li, Z.; Barnes, J. C.; Bosoy, A.; Stoddart, J. F.; Zink, J. I.

Mesoporous Silica Nanoparticles in Biomedical Applications. *Chem. Soc. Rev.* **2012**, *41* (7), 2590–2605.

(10) Slowing, I. I.; Trewyn, B. G.; Giri, S.; Lin, V. S. Y. Mesoporous Silica Nanoparticles for Drug Delivery and Biosensing Applications. *Adv. Funct. Mater.* **2007**, *17* (8), 1225–1236.

(11) Iturrioz-Rodríguez, N.; Correa-Duarte, M. A.; Fanarraga, M. L. Controlled Drug Delivery Systems for Cancer Based on Mesoporous Silica Nanoparticles. *Int. J. Nanomedicine* **2019**, *14*, 3389.

(12) Giannini, V.; Fernández-Domínguez, A. I.; Heck, S. C.; Maier, S. A. Plasmonic Nanoantennas: Fundamentals and Their Use in Controlling the Radiative Properties of Nanoemitters. *Chem. Rev.* **2011**, *111* (6), 3888–3912.

(13) Ghosh, S. K.; Pal, T. Interparticle Coupling Effect on the Surface Plasmon Resonance of Gold Nanoparticles: From Theory to Applications. *Chem. Rev.* **2007**, *107* (11), 4797–4862.

(14) MacIa, N.; Bresoli-Obach, R.; Nonell, S.; Heyne, B. Hybrid Silver Nanocubes for Improved Plasmon-Enhanced Singlet Oxygen Production and Inactivation of Bacteria. *J. Am. Chem. Soc.* **2019**, *141* (1), 684–692.

(15) Macia, N.; Kabanov, V.; Côté-Cyr, M.; Heyne, B. Roles of near and Far Fields in Plasmon-Enhanced Singlet Oxygen Production. *J. Phys. Chem. Lett.* **2019**, *10* (13), 3654–3660.

(16) Macia, N.; Kabanov, V.; Heyne, B. Rationalizing the Plasmonic Contributions to the Enhancement of Singlet Oxygen Production. *J. Phys. Chem. C* **2020**, *124* (6), 3768–3777.

(17) Planas, O.; Macia, N.; Agut, M.; Nonell, S.; Heyne, B. Distance-Dependent Plasmon-Enhanced Singlet Oxygen Production and Emission for Bacterial Inactivation. *J. Am.*

Chem. Soc. **2016**, *138* (8), 2762–2768.

(18) Wang, P.; Tang, H.; Zhang, P. Plasmonic Nanoparticle-Based Hybrid Photosensitizers with Broadened Excitation Profile for Photodynamic Therapy of Cancer Cells. *Sci. Reports* **2016**, *6* (1), 1–8.

(19) Krajczewski, J.; Rucińska, K.; Townley, H. E.; Kudelski, A. Role of Various Nanoparticles in Photodynamic Therapy and Detection Methods of Singlet Oxygen. *Photodiagnosis Photodyn. Ther.* **2019**, *26*, 162–178.

(20) Guo, Y.; Rogelj, S.; Zhang, P. Rose Bengal-Decorated Silica Nanoparticles as Photosensitizers for Inactivation of Gram-Positive Bacteria. *Nanotechnology* **2010**, *21* (6), 065102.

(21) Fowkes, F. M.; Burgess, T. E. Electric Fields at the Surface and Interface of SiO_2 Films on Silicon. *Surf. Sci.* **1969**, *13* (1), 184–195.

(22) Batistela, V. R.; Pellosi, D. S.; De Souza, F. D.; Da Costa, W. F.; De Oliveira Santin, S. M.; De Souza, V. R.; Caetano, W.; De Oliveira, H. P. M.; Scarminio, I. S.; Hioka, N. PKa Determinations of Xanthene Derivates in Aqueous Solutions by Multivariate Analysis Applied to UV–Vis Spectrophotometric Data. *Spectrochim. Acta Part A Mol. Biomol. Spectrosc.* **2011**, *79* (5), 889–897.

(23) Ragàs, X.; Gallardo, A.; Zhang, Y.; Massad, W.; Geddes, C. D.; Nonell, S. Singlet Oxygen Phosphorescence Enhancement by Silver Islands Films. *J. Phys. Chem. C* **2011**, *115* (33), 16275–16281.

(24) Okudera, H.; Hozumi, A. The Formation and Growth Mechanisms of Silica Thin Film and Spherical Particles through the Stöber Process. *Thin Solid Films* **2003**, *434* (1–2), 62–68.

(25) Masalov, V. M.; Sukhinina, N. S.; Kudrenko, E. A.; Emelchenko, G. A. Mechanism of Formation and

Nanostructure of Stöber Silica Particles. *Nanotechnology* **2011**, *22* (27), 275718.

(26) Ludvíková, L.; Friš, P.; Heger, D.; Šebej, P.; Wirz, J.; Klán, P. Photochemistry of Rose Bengal in Water and Acetonitrile: A Comprehensive Kinetic Analysis. *Phys. Chem. Chem. Phys.* **2016**, *18* (24), 16266–16273.

CHAPTER 6

INSTRUMENTATION

6.1. ABSORPTION MEASUREMENTS

6.1.1. UV-Vis spectroscopy

All UV-Vis absorption spectra were registered with a single beam Varian Cary 60 spectrophotometer, using quartz cells of 1cm optical path length.

6.1.2. Dynamic Light Scattering

All the hydrodynamic diameter and Z potential measurements were performed in a Zetasizer Nano ZS spectrophotometer (Malvern Panalytical) equipped with a 632 nm HeNe laser as a light source operating at a 173 degree detector angle. Quartz cells were used for the size measurements and plastic disposable folded capillary cells with two electrodes for the Z-potential measurements. The nanoparticle dispersions were diluted with water. Measurements were made by three for all the samples.

6.2. EMISSION MEASUREMENTS

6.2.1. Fluorescence spectroscopy

εdA steady-state fluorescence measurements in Chapter 4 were performed using a fluorimeter Photon Technology International (PTI), LPS-220B model, equipped with a Xenon lamp of 75 W and a monochromator that covers a range from 200 to 700 nm. Measurements were registered after having adjusted the compound absorbance between 0.03 and 0.1 at the excitation wavelength.

εdC fluorescence spectrum was recorded with Spectra were measured upon 267 nm excitation with a Fluorolog-3 (Horiba, Jobin-Yvon) fluorimeter. Solutions with an absorbance of 0.1 at the excitation wavelength were prepared. As the emissions of the neat buffered solutions were not negligible compared to that of εdC, they were recorded separately and subtracted from the spectra of the sample to remove their contribution. Moreover, the recorded spectra were corrected for the response of the detection system.

6.2.2. Phosphorescence spectroscopy

Phosphorescence spectra of etheno adducts and εdG fluorescence spectrum in Chapter 4 were recorded using an Edinburgh Spectrometer FLS1000, equipped with a 60 W Flash Xenon lamp and a double grating Czerny-Turner monochromators with 2 x 325 mm focal length in detection. Finally, the instrument is equipped with a PMT-980 detector in a cooled housing which covers a range from 200 nm – 980 nm.

All solutions were prepared in ethanol, adjusting their absorbance at ca. 0.8 at the excitation wavelength (with a cuvette of 1 cm optical pathway), then measurements were performed in a quartz tube (0.5 mm diameter) at 77 K. The signal was acquired with a delay time of 0.3 ms and a gate time of 1 ms.

In Chapter 4, Rose Bengal (RB^{2-}) phosphorescence was recorded at room temperature using a customized setup having a diode-pumped Nd:YAG laser as a light source (FTSS355-Q3 model from CryLas, Germany) which was tuned to its second harmonic (532 nm). Detection system consists in a monochromator (CM110) from Spectral Product and a PMT from Hamamatsu (H11526-110-NN detection range 230 nm-700 nm); the PMT output is sent to a multi-channel scaler (TimeHarp 260-Nano, PicoQuant). All solutions were prepared in D_2O, adjusting their absorbance at ca. 0.5 at the excitation wavelength (with a cuvette of 1 cm optical pathway).

6.2.3. Direct detection of singlet oxygen luminescence

Time-resolved near-infrared (TRNIR) phosphorescence detection of $^1O_2$ at 1270 nm was carried-out using a customized setup. A diode-pumped Nd:YAG laser (FTSS355-Q3, CryLas, Germany), tuned to its second harmonic (532 nm) and working at a repetition rate of 1 kHz, was used as an excitation source for RB^{2-}. The kinetic traces were collected by isolating the 1270 nm intrinsic phosphorescence of $^1O_2$ using a monochromator (Digikröm CM110 1/8 m, Spectral Products, Putnam, CT) equipped with a 1150 nm cut-on long-pass filter (FEL1150, ThorLabs, Newton, NJ) and a 1064 nm notch filter (NF1064-44, ThorLabs) mounted

side by side at its entry port and directed to a TE-cooled photomultiplier tube (PMT, H10330A-45, Hamamatsu, Japan), which is working at -908 V and is operated in the photon-counting mode.

After amplification by a 1.1 GHz preamplifier module (PAM-102-T, PicoQuant GmbH, Germany), the output of the PMT was sent to a multi-channel scaler (TimeHarp 260-Nano, PicoQuant). The signals were collected in D_2O for 300 s with 256 ns resolution. The kinetic traces were least-square fitted to equation S1 using Prism 7.0 (GraphPad Software Inc., La Jolla, CA) with τ_Δ, τ_T, and S_0 as free parameters. The quality of the fittings was assessed by the residual plots.

$$S(t) = S_0 \frac{\tau_\Delta}{(\tau_\Delta - \tau_T)} \left(exp\left(\frac{-t}{\tau_\Delta}\right) - exp\left(\frac{-t}{\tau_T}\right) \right) \quad \text{(Equation S1)}$$

Where S(t) is the signal intensity at a time t, τ_Δ is the $^1O_2$ lifetime and τ_T is the photosensitizer's triplet state lifetime. S_0 is defined as the concentration of $^1O_2$ being produced in a given system.

6.3. STEADY-STATE PHOTOLYSIS

Irradiation of the samples containing Rose Bengal were performed under anaerobic and aerobic conditions in Pyrex vials using a Luzchem photoreactor (model LZV-4V) with 8 FLS T5 8W840/CW fluorescent lamps (emission range 350-700nm).

Meanwhile steady-state photolysis of samples containing 4-carboxybenzophenone were irradiated under N_2 in quartz cells using a Luzchem photoreactor (model LZV-4V) with 8 Sankyo Denki G8T5E fluorescent lamps (emission range 280-360nm).

6.4. LASER FLASH PHOTOLYSIS

Laser Flash Photolysis experiments were performed by exciting at 355 and 532 nm, using the 3rd and 2nd harmonic, respectively, of a pulsed laser Nd:YAG (L52137V LOTIS TII) with a pulse duration

of ca. 10 ns. The full system comprises a pulsed laser, a Xenon lamp (Lo 255 Oriel), a monochromator (Oriel 77200), a photomultiplier (Oriel 70705) and an oscilloscope (TDS-640A Tektronic). The output signal from the oscilloscope was transferred to a personal computer.

All experiments were performed in a quartz cell of 1 cm optical path length. Compounds concentration was adjusted in order to have an absorbance of ca. 0.3 at the excitation wavelength.

Before running the measurements under anaerobic conditions, solutions were flushed with N_2, for 15 min. Laser energies ranging from 20 to 35 mJ per pulse were used.

6.5. ULTRAFAST FLUORESCENCE SPECTROSCOPY VIA UPCONVERSION

A detailed description of the femtosecond fluorescence upconversion equipment has been given earlier. [1] Briefly, the 267 nm excitation was generated as a third harmonic of a femtosecond mode-locked Ti-sapphire laser (Coherent MIRA 900). The average excitation power was set at 50 mW. Sample (absorbance of ca. 0.5 at 267 nm) was circulated in a flow system with an optic path of 1 mm in order to avoid degradation.

The fluorescence from the cell was collected and focused into a 1 mm BBO type I crystal using two off-axes parabolic mirrors. It was further passed through a cutoff filter (WG305 or WG320) in order to eliminate the weak remaining UV excitation light.

After the mixing of the fluorescence and the IR gating pulse in the NL crystal, the generated sum-frequency light was focused on the entrance slit of a double monochromator equipped with a photomultiplier (Hamamatsu 1527P) connected to a photon counter (Stanford SR400).

6.6. NUCLEAR MAGNETIC RESONANCE

For all the synthesized compounds, one-dimension ^{1}H and ^{13}C NMR spectra were done with a 300 MHz Varian Bruker instrument, using DMSO-d_6 and $CDCl_3$ as solvents. The corresponding solvent signals were taken as the reference (chemical shift of δ of ca 2.50 ppm and 7.26 ppm respectively for ^{1}H NMR, and 39.52 and 77.16 ppm for ^{13}C NMR). Coupling constants (J) are given in hertz (Hz).

6.7. HPLC ANALYSES

All irradiation mixtures were analyzed on an Agilent 1100 Series HPLC set-up equipped with a UV detector covering a detection range from 200 to 400 nm. Analyses were performed using a Zorbax Eclipse Plus C18 (100 x 4.6 mm, 3.5 μm) column, under isocratic conditions with a mobile phase of 5% acetonitrile (ACN) and 95% H_2O acidified with trifluoroacetic acid (TFA) at pH ca. 3 and a flow rate set at 0.4 mL/min.

The yields of photorepair and concentration of repaired and damage nucleosides were determined from calibration curves using pure compounds.

In Chapter 5, centrifugation (8000 rpm, 10 min) of the samples were done to separate the supernatant containing the nucleoside from the nanoparticle before injection.

6.8. UPLC-HRMS ANALYSIS

A QTof spectrometer coupled with a liquid chromatography system, with a conditional autosampler at 10ºC, was used to determine the exact mass values. The separation was carried out on an UPLC with a Zorbax Eclipse Plus C18 (100 x 4.6 mm, 3.5 μm) column. The ESI source was operated in positive or negative ionization mode with the capillary voltage at 1.9 kV or 2.4 kV, respectively. The source's temperature was set at 80ºC (positive mode) and 400ºC (negative mode), and the cone and desolvation gas flows were 20 and 800 L h^{-1}, respectively. All data were collected in centroid mode, and Leucine-enkephalin was used as the lock

mass generating and $[M+H]^+$ ion (m/z 556.2771) or $[M-H]^-$ ion (m/z 554.2615) at a concentration of 250 pg/mL and flow rate of 50 μL min^{-1} to ensure accuracy during the MS analysis.

6.9. TRANSMISION ELECTRON MICROSCOPY (TEM)

Nanoparticle image characterization were done using a JEM-1400 Flash TEM of 120kV (Jeol, Nieuw-Vennep, Tokyo). The electron source of this microscope is a LaB_6 crystal with a Matataki Flash sCMOS bottom-mounted camera. The entire system provides a resolution up to 0.2 nm mapping structures.

Carbon film supported grid from cupper or nickel has been used for the different measurements. A drop from a suspension of the material was left to dryness on the top of grid.

6.10. INDUCTIVELY COUPLED PLASMA-OPTICAL EMISSION SPECTROSCOPY (ICP-OES)

The metal content of the samples was determined by inductively coupled plasma-optical emission spectroscopy (ICP−OES) (iCAP PRO, ThermoScientific, USA).

Solids were disaggregated in aqua regia and later diluted in water before analysis.

6.11. QUANTUM-CHEMISTRY COMPUTATIONS

Water solution. In order to study the behavior of εdC and $\varepsilon dC(H)^+$ in water we have adopted the computational models depicted in Figure 3.12 (Chapter 3) where the sugar is mimicked by a methyl group, bulk solvent effects are included with the polarizable continuum (PCM) model,[2] and the effect of solute-solvent hydrogen bond interactions considered by explicitly including two H_2O molecules, with the arrangement shown in Figure 3.12 (Chapter 3). Our previous study on Cyt shows indeed that substitution of the sugar with methyl group does not have a significant impact on the excited

state behaviour.[3] Calculations have been also performed without including explicit water molecules. DFT and TD-DFT, using the M052X functional,[4,5] have been used as reference computational model, since they have been already profitably adopted to study the photoactivated behaviour of Cyt derivatives in solution.[3,6] All the TD-DFT calculations have been performed by the Gaussian16 program.[7]

Gas Phase. In parallel we have mapped the PES of εCH and εCH^+ in the gas phase by Complete Active Space Self Consistent Field (CASSCF)[8,9] optimization of minima and state crossings and minimum energy path calculations. Energies have been corrected using second-order perturbation theory (CASPT2) in its single and multistate (MS)[10] formulation with an IPEA shift[11] of 0.0 a.u. and an imaginary level shift[12] of 0.3 a.u. The selected active space, 16 electrons in 12 orbitals, contains all the π and π* orbitals together with the Lone Pairs of the O and N8 atoms for εCH. Since the latter is not present in εCH^+ the active space is reduced to 14 electrons in 11 orbitals. An equal weight state-average over 5 states was used throughout. To be consistent with the DFT calculations these calculations were also done using the 6-31G(d) basis set OpenMolcas software has been used for these calculations.[13]

6.12. REFERENCES

(1) Miannay, F.-A. A.; Gustavsson, T.; Banyasz, A.; Markovitsi, D. Excited-State Dynamics of DGMP Measured by Steady-State and Femtosecond Fluorescence Spectroscopy. *J. Phys. Chem. A* **2010**, *114* (9), 3256–3263.

(2) Tomasi, J.; Mennucci, B.; Cammi, R. Quantum Mechanical Continuum Solvation Models. *Chem. Rev.* **2005**, *105* (8), 2999–3093.

(3) Martínez-Fernández, L.; Pepino, A. J.; Segarra-Martí, J.; Jovaišaitei, J.; Vaya, I.; Nenov, A.; Markovitsi, D.; Gustavsson, T.; Banyasz, A.; Garavelli, M.; Improta, R. Photophysics of Deoxycytidine and 5-Methyldeoxycytidine in Solution: A Comprehensive Picture by Quantum Mechanical Calculations and Femtosecond Fluorescence Spectroscopy. *J. Am. Chem. Soc.* **2017**, *139* (23), 7780–7791.

(4) Zhao, Y.; Schultz, N. E.; Truhlar, D. G. Design of Density Functionals by Combining the Method of Constraint Satisfaction with Parametrization for Thermochemistry, Thermochemical Kinetics, and Noncovalent Interactions. *J. Chem. Theory Comput.* **2006**, *2* (2), 364–382.

(5) Zhao, Y.; Truhlar, D. G. Density Functionals with Broad Applicability in Chemistry. *Acc. Chem. Res.* **2008**, *41* (2), 157–167.

(6) Improta, R.; Santoro, F.; Blancafort, L. Quantum Mechanical Studies on the Photophysics and the Photochemistry of Nucleic Acids and Nucleobases. *Chem. Rev.* **2016**, *116* (6), 3540–3593.

(7) Frisch, M. J.; Trucks, G. W.; Schlegel, H. B.; Scuseria, G. E.; Robb, M. A.; Cheeseman, J. R.; Scalmani, G.; Barone, V.; Petersson, G. A.; Nakatsuji, H.; Li, X.; Caricato, M.; Marenich, A. V.; Bloino, J.; Janesko, B. G.; Gomperts, R.; Mennucci, B.; Hratchian, H. P.; Ortiz, J. V.; Izmaylov, A. F.; Sonnenberg, J. L.; Williams-Young, D.; Ding, F.; Lipparini,

F.; Egidi, F.; Goings, J.; Peng, B.; Petrone, A.; Henderson, T.; Ranasinghe, D.; Zakrzewski, V. G.; Gao, J.; Rega, N.; Zheng, G.; Liang, W.; Hada, M.; Ehara, M.; Toyota, K.; Fukuda, R.; Hasegawa, J.; Ishida, M.; Nakajima, T.; Honda, Y.; Kitao, O.; Nakai, H.; Vreven, T.; Throssell, K.; Montgomery, J. A., J.; Peralta, J. E.; Ogliaro, F.; Bearpark, M. J.; Heyd, J. J.; Brothers, E. N.; Kudin, K. N.; Staroverov, V. N.; Keith, T. A.; Kobayashi, R.; Normand, J.; Raghavachari, K.; Rendell, A. P.; Burant, J. C.; Iyengar, S. S.; Tomasi, J.; Cossi, M.; Millam, J. M.; Klene, M.; Adamo, C.; Cammi, R.; Ochterski, J. W.; Martin, R. L.; Morokuma, K.; Farkas, O.; Foresman, J. B.; Fox, D. J. Gaussian 16 Revision C01. **2016**, p Gaussian 16, Revision C.01, *Gaussian, Inc., Wallin*.

(8) Andersson, K.; Malmqvist, P. A.; Roos, B. O.; Sadlej, A. J.; Wolinski, K. Second-Order Perturbation Theory with a CASSCF Reference Function. *J. Phys. Chem.* **1990**, *94* (14), 5483–5488.

(9) Andersson, K.; Malmqvist, P.; Roos, B. O. Second-order Perturbation Theory with a Complete Active Space Self-consistent Field Reference Function. *J. Chem. Phys.* **1992**, *96* (2), 1218–1226.

(10) Finley, J.; Malmqvist, P.-Å.; Roos, B. O.; Serrano-Andrés, L. The Multi-State CASPT2 Method. *Chem. Phys. Lett.* **1998**, *288*, 299–306.

(11) Ghigo, G.; Roos, B. O.; Malmqvist, P.-Å. A Modified Definition of the Zeroth-Order Hamiltonian in Multiconfigurational Perturbation Theory (CASPT2). *Chem. Phys. Lett.* **2004**, *396* (1), 142–149.

(12) Forsberg, N.; Malmqvist, P.-Å. Multiconfiguration Perturbation Theory with Imaginary Level Shift. *Chem. Phys. Lett.* **1997**, *274* (1), 196–204.

(13) Fernández Galván, I.; Vacher, M.; Alavi, A.; Angeli, C.; Aquilante, F.; Autschbach, J.; Bao, J. J.; Bokarev, S. I.; Bogdanov, N. A.; Carlson, R. K.; Chibotaru, L. F.;

Creutzberg, J.; Dattani, N.; Delcey, M. G.; Dong, S. S.; Dreuw, A.; Freitag, L.; Frutos, L. M.; Gagliardi, L.; Gendron, F.; Giussani, A.; Gonzalez, L.; Grell, G.; Guo, M.; Hoyer, C. E.; Johansson, M.; Keller, S.; Knecht, S.; Kovačević, G.; Källman, E.; Li Manni, G.; Lundberg, M.; Ma, Y.; Mai, S.; Malhado, J. P.; Malmqvist, P. A.; Marquetand, P.; Mewes, S. A.; Norell, J.; Olivucci, M.; Oppel, M.; Phung, Q. M.; Pierloot, K.; Plasser, F.; Reiher, M.; Sand, A. M.; Schapiro, I.; Sharma, P.; Stein, C. J.; Sørensen, L. K.; Truhlar, D. G.; Ugandi, M.; Ungur, L.; Valentini, A.; Vancoillie, S.; Veryazov, V.; Weser, O.; Wesolowski, T. A.; Widmark, P.-O.; Wouters, S.; Zech, A.; Zobel, J. P.; Lindh, R. OpenMolcas: From Source Code to Insight. *J. Chem. Theory Comput.* **2019**, *15* (11), 5925–5964.

CHAPTER 7

GENERAL CONCLUSIONS

In this Doctoral Thesis, the study of photochemical and photophysical behavior of DNA ε-adducts is addressed to get more insights into how structural changes are capable to modify the properties of DNA derivatives. To achieve this goal, computational chemistry, spectroscopic and steady-state photolysis experiments were performed.
The conclusions of each chapter can be summarized as follows:

1) In Chapter 3, femtosecond upconversion fluorescence measurements were carried out together with steady-state fluorescence to study the singlet channel of εdC. In addition, non-radiative and radiative deactivation pathways were examined using theoretical calculations (at the PCM-TD-DFT and CASPT2/CASSCF levels).

⇒ *These results show that the addition of an extra etheno ring on the canonical dC alters its photobehavior. On the one hand, εdC exhibits a red-shifted absorption compared to dC, which increases the UVB fraction of sunlight that can be directly absorbed by εdC–containing DNA. However, the etheno bridge decreases the efficiency of the non-radiative deactivation by lengthening the excited state lifetime. The larger absorption windows and the longer singlet lifetime may trigger undesired photolesions in the DNA.*

2) Chapter 4 tackles the photophysical properties of εdA and εdG adducts. Moreover, the photochemical reactivity of the three etheno adducts is considered using Type I and Type II photosensitizers.

⇒ *From a photophysical point of view, the etheno adducts present a red shifted absorption spectra and moderate fluorescence emission with a relatively longer lifetime than their canonical counterparts. The ε-adducts triplet excited states are lower in energy than those reported for their corresponding bases.*

⇒ *Irradiation of ε-adducts in the presence of Type I and Type II photosensitizers showed repair of the lesion under both aerobic and anaerobic conditions. εdG was found to be easily oxidized through both types of processes, by contrast, for εdA, an electron transfer mechanism seems to be the main pathway. These results open the possibility to further develop systems able to regenerate the original DNA bases from the ε-adduct.*

3) In Chapter 5, hybrid metal NPs have been considered as a system to optimize the repair ε-adduct process taking advantage not only of their ability to act as matrix to support Rose Bengal but also of the surface plasmon resonance reported to enhance the optical properties of the NPs.

⇒ *SiO_2 and Ag@SiO_2 nanoparticles have been synthesized and functionalized with Rose Bengal.*

⇒ *Metal nanoparticles (Ag@SiO_2-RB) present faster repair kinetics together with higher yields than control SiO_2-RB NPs. This effectivity results from the enhanced effect triggered by the plasmon-resonance, which seems to be more efficient for the processes taking place under anaerobic conditions.*

CHAPTER 8

SCIENTIFIC CONTRIBUTIONS

8.1. CONGRESS CONTRIBUTIONS

1. Paloma Lizondo-Aranda, Miguel Ángel Miranda and Virginie Lhiaubet-Vallet. "Photochemical repair of etheno adducts". Iberian Symposium of Young Photochemists, online, 18th – 21th October **2021**. Oral presentation.
2. Paloma Lizondo-Aranda, Thomas Gustavsson, Miguel Ángel Miranda and Virginie Lhiaubet-Vallet. "An insight into etheno adducts optical properties". 19th Congress of the European Society for Photobiology, online, 30th August to 3rd September **2021**. Oral presentation.
3. Paloma Lizondo-Aranda, Thomas Gustavsson, Miguel Ángel Miranda and Virginie Lhiaubet-Vallet. "Estudio detallado sobre las propiedades espectroscópicas de los aductos del ADN de tipo eteno originados en el proceso de peroxidación de lípidos". V Reunión Nacional del Grupo Argentino de Fotobiología (GRAFOB), online, September **2020**. Oral presentation.
4. Paloma Lizondo-Aranda, Thomas Gustavsson, Miguel Ángel Miranda and Virginie Lhiaubet-Vallet. "Spectroscopic studies of DNA adducts arising from polyunsaturated fatty acid oxidation". 2nd ITQ Winter Meeting, Valencia, Spain, 19th December **2019**. Oral presentation.
5. Paloma Lizondo-Aranda, Thomas Gustavsson, Miguel Ángel Miranda and Virginie Lhiaubet-Vallet. "Optical properties of base-modified nucleosides". XVI Simposio de Jóvenes Investigadores de la Real Sociedad Española de Química, Valencia, Spain, 4th-7th November **2019**. Oral presentation.
6. Paloma Lizondo-Aranda, Thomas Gustavsson, Miguel Ángel Miranda and Virginie Lhiaubet-Vallet. "A photophysical study of DNA lesions arising from the oxidation of polyunsaturated fatty acid". 3rd Workshop on DNA Damage and Repair. Chemistry, Biology, and Medicine, Valencia, Spain, 25th-26th September **2019**. Oral presentation.
7. Paloma Lizondo-Aranda, Thomas Gustavsson, Miguel Ángel Miranda and Virginie Lhiaubet-Vallet.

"Spectroscopic studies of DNA adducts arising from polyunsaturated fatty acid oxidation". 17th Congress of the International Union of Photobiology and 18th Congress of the European Society for Photobiology, Barcelona, Spain, 25th-30th August **2019**. Poster presentation.

8. Paloma Lizondo-Aranda, Miguel Ángel Miranda and Virginie Lhiaubet-Vallet. "Study of intrinsic DNA damages the etheno derivative". 1st ITQ Winter Meeting, Valencia, Spain, 17th December **2018**. Oral presentation.
9. Paloma Lizondo-Aranda, Miguel Ángel Miranda and Virginie Lhiaubet-Vallet. "Study of intrinsic DNA damage etheno derivative". VIth Jornadas Ibéricas de Fotoquímica, Aveiro, Portugal, 11th-14th September **2018**. Poster presentation.
10. Paloma Lizondo-Aranda, Miguel Ángel Miranda and Virginie Lhiaubet-Vallet. "Lipid peroxidation derived DNA lesions as intrinsic photosensitizers in the formation of clustered damage". 5th ESP Photobiology School, Bressanone, Italy, 10th-16th June **2018**. Poster presentation.
11. Paloma Lizondo-Aranda, Miguel Ángel Miranda and Virginie Lhiaubet-Vallet. "DNA Etheno adducts, a potential mutagenic lesion". 2nd Conference on Properties, Design and Applications of Upconversion Nanomaterials, Valencia, Spain, 4th- 6th April **2018**. Oral presentation.

8.2. PUBLICATION RELATED TO THIS DOCTORAL THESIS

1. Paloma Lizondo-Aranda, Lara Martínez-Fernández, Miguel A. Miranda, Roberto Improta, Thomas Gustavsson, and Virginie Lhiaubet-Vallet. "The Excited State Dynamics of a Mutagenic Cytidine Etheno Adduct Investigated by Combining Time-Resolved Spectroscopy and Quantum Mechanical Calculations", *J. Phys Chem. Lett.* **2022**, 13, 1, 251–257.

8.3. OTHER PUBLICATION

1. Jesuan J. Farías, Paloma Lizondo-Aranda, Andrés H. Thomas, Virginie Lhiaubet-Vallet and M. Laura Dántola. "Pterin-lysine photoadduct: a potential candidate for photoallergy." *Photochem. Photobiol. Sci.* **2022**.

SUMMARY
RESUMEN
RESUM

SUMMARY

Studies dealing with DNA damages have increased during the last decades in order to get more insight into their involvement in the appearance of cancer. Among the large number of DNA lesions, etheno adducts have been the matter of interest because of their presence in chronically inflamed human tissues, making their quantification useful as potential biomarkers for cancer of colon, prostate, lung, etc. Moreover, these lesions exhibit highly mutagenic properties and induce base transitions or transversion in mammal cells. Etheno adducts are mainly formed endogenously as a result of lipid peroxidation. This biochemical process produces reactive aldehydes such as malondialdehyde, which can combine with DNA bases creating the exocyclic ring. This exocyclic ring provides to the nucleobases an extended π- conjugated system that might confer them optical properties different from those of the canonical bases, and can pose a threat to the DNA photostability.
Canonical bases have the ability to dissipate most of the excitation energy through efficient nonradiative channels leading back to the ground state. However, the studies about the optical properties of this etheno adducts are basics to make it clear whether these lesions can jeopardize this efficient relaxation and trigger undesired DNA photoreactivity.

The first part of the thesis establishes the potential photoactivity of these DNA lesions through a spectroscopic study. Chapter 3 joints femtosecond fluorescence upconversion experiments and theoretical calculations (at the PCM-TD-DFT and CASPT2/CASSCF levels) to provide a comprehensive picture of the mutagenic etheno adduct 3,N4-etheno-2'-deoxycytidine (εdC) excited states relaxation.

Photophysics studies show that the etheno bridge significantly affects εdC optical properties in respect with those of its canonical base dC. Indeed, the fluorescence quantum yield (ϕ_f) and average lifetime $<\tau>$ increase notably. Despite the extra ring does not affect the common pyrimidine radiative deactivation pathway, this structural change decreases the efficiency of the non-radiative deactivation by lengthening the excited state lifetime.

Chapter 4 addresses the photophysical properties of the adducts together with its photoreactivity in the presence of some common photosensitizers as Rose Bengal and 4-carboxybenzophenone, paying a special attention to interaction with $^1O_2$. Interaction with $^1O_2$ is observed for the three studied ε-adducts. Interestingly, the same nucleobase formation is detected for irradiation under anaerobic conditions, opening the possibility of a mixed Type I and Type II mechanism when Rose Bengal is used as photosensitizer, and Type I for 4-carboxybenzophenone. Steady-state photolysis studies, carried out together with some laser flash photolysis experiments, allow establishing that εdG is sensitive to both types of processes (Type I and II), and that εdA is decomposed mainly through an electron transfer mechanism.

Finally, the last chapter takes advantage of all the gained knowledge about the photoreactivity of ε-adducts to choose the best chromophore and optimize the repair process observed in Chapter 4.

To achieve this, hybrid systems of Ag metal nanoparticles are used as a support matrix for the Rose Bengal. Metal NPs, such as Ag NP, possess localized surface plasmon resonance (LSPR). This effect amplifies a wide variety of optical phenomena that can enhance the Rose Bengal optical properties. To study this phenomenon, two types of nanoparticles have been synthesized: a non-optically active NP SiO_2 and an optically active metal NP Ag coated with 14 nm of SiO_2 (Ag@SiO_2-RB). Then, steady-state photolysis studies are carried out with both nanoparticles under aerobic and anaerobic conditions. In both cases, Ag@SiO_2-RB NPs present faster repair kinetics together with higher repair yields than control SiO_2-RB NPs, demonstrating that LSPR enhances the photorepair process of ε-adducts in this system.

RESUMEN

Los estudios sobre los daños en el ADN se han incrementado en las últimas décadas con el fin de profundizar en su implicación en la aparición del cáncer. Entre el gran número de lesiones del ADN, los aductos de tipo eteno han sido objeto de interés debido a su presencia en los tejidos humanos crónicamente inflamados. Asimismo, su cuantificación es útil para su uso como potencial biomarcador del cáncer de colon, próstata, pulmón, etc. Además, estas lesiones presentan propiedades altamente mutagénicas e inducen transiciones de bases o transversiones en las células de mamíferos. Los aductos de tipo eteno se generan principalmente de forma endógena como resultado de la peroxidación lipídica. Este proceso bioquímico produce aldehídos reactivos como el malondialdehído, que pueden combinarse con las bases del ADN creando un anillo exocíclico.

Este anillo exocíclico proporciona a la nucleobase un sistema extendido π-conjugado que puede conferirles propiedades ópticas diferentes a las de las bases canónicas, lo que puede suponer una amenaza para la fotoestabilidad del ADN.

Las bases canónicas tienen la capacidad de disipar la mayor parte de la energía recibida a través de canales no radiativos eficientes que conducen de nuevo al estado fundamental. Por lo tanto, los estudios sobre las propiedades ópticas de estos aductos etenos son clave para establecer si estas lesiones pueden poner en peligro la relajación eficiente de los estados excitados de las bases y desencadenar una fotorreactividad indeseada del ADN.

La primera parte de la tesis trata de evaluar la fotoactividad potencial de estas lesiones del ADN mediante un estudio espectroscópico. En el Capítulo 3 se combinan experimentos de upconversión de fluorescencia en la escala de femtosegundos y cálculos teóricos (en los niveles PCM-TD-DFT y CASPT2/CASSCF) para proporcionar una imagen completa de la relajación de los estados excitados del aducto mutagénico 3,N4-eteno-2'-desoxicitidina (εdC).

Los estudios fotofísicos mostraron que el puente de tipo eteno afecta significativamente a las propiedades ópticas del εdC respecto

a su base canónica dC. En efecto, el rendimiento cuántico de fluorescencia (ϕ_f) y el tiempo de vida medio $<\tau>$ aumentan notablemente.
A pesar de que el anillo no afecta a la vía principal de desactivación radiativa de la pirimidina, este cambio estructural disminuye la eficiencia de la desactivación no radiativa alargando el tiempo de vida del estado excitado.

El Capítulo 4 aborda las propiedades fotofísicas de los aductos junto con su fotorreactividad en presencia de fotosensibilizadores comunes como la Rosa de Bengala (RB) y la 4-carboxibenzofenona (CBP), prestando especial atención a la interacción con el $^1O_2$. En condiciones aeróbicas, se observa una interacción con $^1O_2$ para los tres aductos estudiados. Curiosamente, se observan los mismos fotoproductos, las nucleobases originales, para la irradiación en condiciones anaeróbicas, abriendo la posibilidad de un mecanismo mixto de Tipo I y Tipo II cuando se utiliza Rosa de Bengala como fotosensibilizador, y de Tipo I para la 4-carboxibenzofenona.

Los estudios de fotólisis en estado estacionario realizados junto con algunos experimentos de fotólisis de destello láser permiten establecer que el εdG es sensible a ambos tipos de procesos (Tipo I y II), y que el εdA se descompone principalmente a través de un mecanismo de transferencia electrónica.

Finalmente, el último capítulo trata de unir todos los conocimientos adquiridos sobre la fotorreactividad de los ε-aductos para elegir el mejor cromóforo tratando de optimizar el proceso de reparación observado en el Capítulo 4.
Para ello se utilizan sistemas híbridos de nanopartículas metálicas de Ag como matriz de soporte para la Rosa de Bengala. Las NPs metálicas, como las Ag NPs, poseen una resonancia plasmónica superficial localizada (LSPR), este efecto amplifica una gran variedad de fenómenos ópticos que pueden mejorar las propiedades ópticas de la Rosa de Bengala. Para estudiar este fenómeno se han sintetizado dos tipos de nanopartículas decoradas con Rosa de Bengala : unas de SiO_2 no ópticamente activas y unas de Ag metálica ópticamente activas recubiertas con 14 nm de SiO_2 (Ag@SiO_2-RB). A continuación, se realizaron estudios de fotólisis en estado estacionario con ambas nanopartículas en condiciones aeróbicas y

anaeróbicas, y las Ag@SiO_2-RB presentan una cinética de reparación más rápida junto con rendimientos de reparación más altos que las NP control SiO_2-RB, demostrando que la LSPR mejora el proceso de fotorreparación de los aductos de tipo eteno en este sistema.

RESUM

Els estudis sobre els danys en l'ADN s'han incrementat en les últimes dècades amb la finalitat d'aprofundir en la seua implicació en l'aparició del càncer. Entre el gran nombre de lesions de l'ADN, els adductes de tipus eteno han sigut objecte d'interés degut a la seua presència en els teixits humans crònicament inflamats, la qual cosa fa que la seua quantificació siga útil com a potencials biomarcadors del càncer de còlon, pròstata, pulmó, etc. A més, aquestes lesions presenten propietats altament mutagèniques i indueixen transicions de bases o transversions en les cèl·lules dels mamífers. Els adductes de tipus eteno es formen principalment de manera endògena com a resultat de la peroxidació dels lípids. Aquest procés bioquímic produeix aldehids reactius com el malondialdehid, que poden combinar-se amb les bases de l'ADN creant un anell exocíclic.

Aquest anell exocíclic proporciona a les nucleobases un sistema estés π-conjugat que pot conferir-les propietats òptiques diferents a les de les bases canòniques, i que poden suposar una amenaça per a la fotoestabilitat de l'ADN.

Les bases canòniques tenen la capacitat de dissipar la major part de l'energia d'excitació a través de canals no radiatius eficients que condueixen de nou a l'estat bàsic. No obstant això, els estudis sobre les propietats òptiques d'aquests adductes de tipus eteno són fonamentals per a deixar clar si aquestes lesions poden posar en perill aquesta relaxació eficient i desencadenar una fotoreactivitat indesitjada de l'ADN.

La primera part de la tesi tracta d'estimar el potencial fotoactiu d'aquestes lesions de l'ADN mitjançant un estudi espectroscòpic. En el Capítol 3 es combinen experiments de "upconversió" de fluorescència en una escala de femtosegons i càlculs teòrics (en els nivells PCM-TD-DFT i CASPT2/CASSCF) per a proporcionar una imatge completa de la relaxació dels estats excitats del adducte mutagènic 3,N4-eteno-2'-desoxicitidina (εdC).

Els estudis fotofísics van mostrar que el pont de tipus eteno afecta significativament a les propietats òptiques del εdC respecte a la seua

base canònica dC. En efecte, el rendiment quàntic de fluorescència (ϕ_f) i el temps de vida mig $<\tau>$ augmenten notablement.

A pesar que l'anell no afecta a la via comuna de desactivació radiativa de la pirimidina, aquest canvi estructural disminueix l'eficiència de la desactivació no radiativa allargant el temps de vida de l'estat excitat.

El Capítol 4 aborda les propietats fotofísiques dels adductes restants juntament amb el seua fotoreactivitat en presència d'alguns fotosensibilitzadors comuns com la Rosa de Bengala (RB) i la 4-carboxibenzofenona (CBP), prestant especial atenció a la interacció amb el $^1O_2$. S'observa la interacció amb $^1O_2$ per als tres adductes estudiats.

Curiosament, s'observa la mateixa formació de nucleobases per a la irradiació en condicions anaeròbiques, obrint la possibilitat d'un mecanisme mixt de Tipus I i Tipus II quan s'utilitza Rosa de Bengala com fotosensibilitzador i de Tipus I per a la 4-carboxibenzofenona.

Els estudis de fotòlisi en estat estacionari realitzats juntament amb alguns experiments de fotòlisi de flaix làser permeten establir que el εdG és sensible a tots dos tipus de processos (Tipus I i II), i que el εdA es descompon principalment a través d'un mecanisme de transferència d'electrons.

Finalment, l'últim capítol tracta d'unir tots els coneixements adquirits sobre la fotoreactivitat dels adductes de tipus eteno per a triar el millor cromòfor tractant d'optimitzar el procés de reparació observat en el Capítol 4.

Per a això s'utilitzen sistemes híbrids de nanopartícules metàl·liques de Ag com a matriu de suport per a la Rosa de Bengala. Les NPs metàl·liques, com les de Ag, posseeixen ressonància plasmónica superficial localitzada (LSPR), aquest efecte amplifica una gran varietat de fenòmens òptics que poden millorar les propietats òptiques de la Rosa de Bengala. Per a estudiar aquest fenomen s'han sintetitzat dos tipus de nanopartícules decorades amb Rosa de Bengala: una de SiO_2 no òpticament actives i una de Ag metàl·lica òpticament activa coberta amb 14 nm de SiO_2 (Ag@SiO_2-RB). A continuació, es van realitzar estudis de fotòlisi en estat estacionari amb totes dues nanopartícules en condicions aeròbiques i anaeròbiques, i les Ag@SiO_2-RB presenten una cinètica

de reparació més ràpida juntament amb rendiments de reparació més alts que les NPs de control (SiO_2-RB), demostrant que la LSPR millora el procés de fotoreparació dels adductes de tipus eteno en aquest sistema.